UNIVERSITY OF LEICESTER

MPhil Thesis:

‘Studies of Helium Droplet Mass Spectrometry and Magnetic Nanoparticles’

University of Leicester

Charlotte Pughe MChem

(139018027)

2019

Abstract

‘Studies of Helium Droplet Mass Spectrometry and Magnetic Nanoparticles’

Charlotte Pughe

As the title suggests, this MPhil thesis is separated into two research topics. The first topic is based in the field of superfluid helium droplet science, and explores mass spectrometry of conjugated molecules in superfluid helium droplets. Recent observations have suggested conjugated molecules behave very differently to other molecules upon electron ionization in the helium droplet environment. The helium droplet mass spectrum of p-benzoquinone was recorded and compared to the gas phase mass spectrum. To try to explain the fragmentation process, density functional theory calculations were performed on the initial fragmentation pathways. By combining the experimental data and the theoretical calculations, a model to explain the reduced parent ion signal in the helium droplet mass spectrum of p-benzoquinone was developed. The model suggests the high energy of the proton loss pathway and the potential of a large energy barrier to parent ion ejection, forces p-benzoquinone to almost completely fragment upon ionisation inside the helium droplet. Further studies with other conjugated molecules could reveal more information about the influence of the helium matrix on dopant species.

The second research topic investigates new methods to produce high moment iron oxide/iron nanoparticles. Iron oxide nanoparticles have been the focus of great research interest due to their various applications. Here, a modified approach to make iron oxide based on the co-precipitation technique was explored as a simple route to increase the nanoparticle magnetic moment. By applying a weak magnetic field to the reaction vessel it was found the magnetic saturation of the nanoparticles could be increased by a few emu/g. A novel method of producing pure iron nanoparticles based on liquid plasma nanosynthesis has also been proposed. The design for the liquid plasma reactor could allow iron nanoparticles, which have even higher moments than iron oxide, to be produced on a large scale.

Acknowledgements

Many thanks are given to the following people:

Dr Corey Evans, Associate Professor in Physical Chemistry (University of Leicester), for his supervisory support during this project and beyond.

Dr Michael Fay, Senior Research Fellow at the Nanoscale and Microscale Research Centre (University of Nottingham), for his assistance with the TEM imaging of the nanoparticles in Chapter 2.

Dr. Martin R. Lees, from the Superconductivity and Magnetism Group in the University of Warwick Physics Department, for his help obtaining and interpreting the SQUID magnetometry data in Chapter 2.

Mr Carl Schieferstein, Mr Gareth Bustin, Mrs Gayle Price and Mr Saiful Choudhury from the Chemistry Workshop and Stores for all their help designing and preparing equipment used to complete this MPhil.

Fellow students Martin Mugglestone and Leanne Abigail Blount for always being there to listen to my problems and help where they could.

My family for putting up with me during this project and for always supporting my decisions.

Contents

List of Figures

Abbreviations List

HeDs – Superfluid helium droplets

SPION – Superparamagnetic iron oxide nanoparticles

USPION – Ultrasmall superparamagnetic iron oxide nanoparticles

M_S – Magnetic saturation

DFT – Density functional theory

IRC – Intrinsic reaction coordinate

Introduction to Thesis

This thesis presents the research conducted in the Spectroscopy and Dynamics Group at the University of Leicester. The thesis is broadly divided into two research topics. The first research topic is a preliminary investigation of conjugated molecules in superfluid helium droplets based upon recent experimental findings. The second research topic was concerned with the synthesis of iron oxide/iron nanoparticles. This involved both improving existing methods, as well as designing new methods to produce high moment iron oxide nanoparticles intended for biomedical applications such as Magnetic Resonance Imaging (MRI) contrast agents and magnetic hyperthermia. The research topics are very different. Therefore this thesis will be divided into three chapters: one chapter for the superfluid helium droplet research and two chapters for the research on iron oxide/iron nanoparticles. Within each chapter, the story behind the research and results will be individually discussed. The rest of this overall introduction provides a brief synopsis of the three research chapters.

Superfluid helium droplets possess a number of unique properties, including ultra-high thermal conductivities, near-zero viscosity, and quantum phenomena. These properties, coupled with the high droplet pick-up probability, have made helium droplets novel micro-laboratories in which a whole range of species from single atoms, to multi-element clusters can be isolated and studied. The exotic environment often produces unusual cluster species, and the behaviour of the so-called ‘dopants’ inside the droplet can reveal information about the fundamental physics of the droplet environment. The most commonly used methods of studying dopants in helium droplets are spectroscopy and mass spectrometry. Helium droplet mass spectrometry was once thought to be a new method of achieving soft electron ionisation, particularly for small alcohols and haloalkanes, which severely fragment upon gas phase electron ionisation. Subsequent studies showed softening effects were largely dependent on the molecule, but did often lead to a small increase in the parent ion peak, as well as changes in the ratios between the daughter fragments. Common observations are large increases in the intensity of daughter fragments that produce small neutral or radical molecules as they are more easily ejected from the droplet. Therefore, the proton loss channel, which is of course the lightest species which can be lost, is often greatly enhanced. Conversely, experimental studies presented in Chapter 1 have suggested simple conjugated

molecules fragment very differently to non-conjugated molecules. This theory came from studies of p-benzoquinone in helium droplets, where instead of an increase in the parent ion peak, it was almost completely reduced relative to the gas phase mass spectrum. By studying the fragmentation process using density functional theory, a model for this observation has been developed. Similar conjugated and aromatic systems have also been studied using the same computational approach and are expected to display a similarly reduced parent ion signal in their helium droplet mass spectrum. This observation could reveal more information about the helium droplet fragmentation process and influence the helium matrix has on the parent ion.

Moving onto the second research topic, the remainder of the thesis is concerned with the synthesis of high moment iron oxide/iron nanoparticles. Nanomaterials are largely at the forefront of modern materials because their properties vary dramatically from the bulk. Iron oxide nanoparticles have been the subject of extensive research effort because of their high magnetic moment, easy synthesis and biocompatibility. They have an expanding list of applications in areas such as biomedicine, energy technologies, chemical synthesis, data storage and the environment. One of the main challenges for synthesising iron oxide nanoparticles is forming high moment iron oxide nanoparticles with a narrow size distribution and high yields, using a method which can easily be translated to industrial scale-up. Chemical methods are often favoured because they give high yields and can be scaled up. However, these methods do not always produce nanoparticles with the desired properties for their applications. As a result, this second research topic aims to research new and existing methods to overcome this challenge.

The second research topic has been divided into two chapters: Chapter 2 and Chapter 3. Chapter 2 looks at obtaining high moment nanoparticles using a widely used approach to synthesise iron oxide nanoparticles, known as co-precipitation. It has been shown magnetic field assisted synthesis can improve the quality of iron oxide nanoparticles synthesised using this high yielding method. Most previous researchers have employed high magnetic fields to achieve this. Therefore, the intention is to investigate whether similar results are obtained when the reaction is exposed to a weaker magnetic field. Chapter 3 proposes a novel method for synthesising iron nanoparticles based upon liquid plasma nanosynthesis. The advantages of electrochemical synthesis are discussed and the design for a continuous liquid plasma reactor for the production of high moment ultra-small (<5 nm) iron nanoparticles presented. Pure iron nanoparticles have much

higher moments than iron oxide nanoparticles, but they oxidize quickly. However, if oxidation can be prevented, the higher magnetic moment would be exceedingly attractive for multiple applications throughout biomedicine and beyond.

Chapter 1

Fragmentation of Conjugated Molecules in Superfluid Helium Droplets

1. Introduction

1.1 Fundamentals of superfluid helium droplets

Superfluid helium droplets (HeDs) are an exotic environment for the study of single species (atoms, molecules and ions), binary complexes and clusters (both pure and core-shell). HeDs are typically composed of 10^3-10^{11} helium atoms and possess a number of unique properties including: high pick-up probabilities, extremely low internal temperatures, vanishingly low viscosities, high thermal conductivities and quantum behaviours, such as the formation of quantized vortices.[1,2] These properties have often allowed entrapped species to adopt unusual structures, which has led to helium nanodroplet isolation (HENDI) becoming a valuable technique to study species previously unobtainable by other methods. Experimental studies are typically performed using spectroscopy and mass spectrometry.[3] In addition, dopants such as large metal clusters can be studied ex-situ by deposition from the HeDs onto a suitable surface; a technique through which HeDs nanoscience has grown. Dopants also act as a probe for the superfluid environment, which is equally fascinating to both physicists and chemists alike, and is the method by which the superfluid properties of HeDs were discovered.[4,5] For these reasons, HeDs have often been called 'ultracold nanolaboratories' and are continuing to find new uses in many areas of science.[6]

1.1.1 Origins of superfluidity

Fundamentally, superfluidity is a result of helium's ability to attain extremely low temperatures and the bosonic nature of the helium atom. Helium is the only element able to remain a liquid at 0 K because of the low binding energy of 5 cm^{-1} between helium atoms.[7,8] The binding energy is comparable to the zero point energy, preventing helium atoms from attaining fixed lattice positions. The phase diagram in Fig. 1(a) shows formation of the solid phase requires pressures exceeding 25 bar to force helium

atoms into a lattice. Consequently, unlike all other elements, the phase diagram of helium has no triple point. Instead, the four phases are connected along the λ-line, which splits the superfluid (He II) phase and liquid (He I) phase, and extends from the upper λ-point, where it meets the solid phase, to the lower λ-point, where it meets the gas phase.

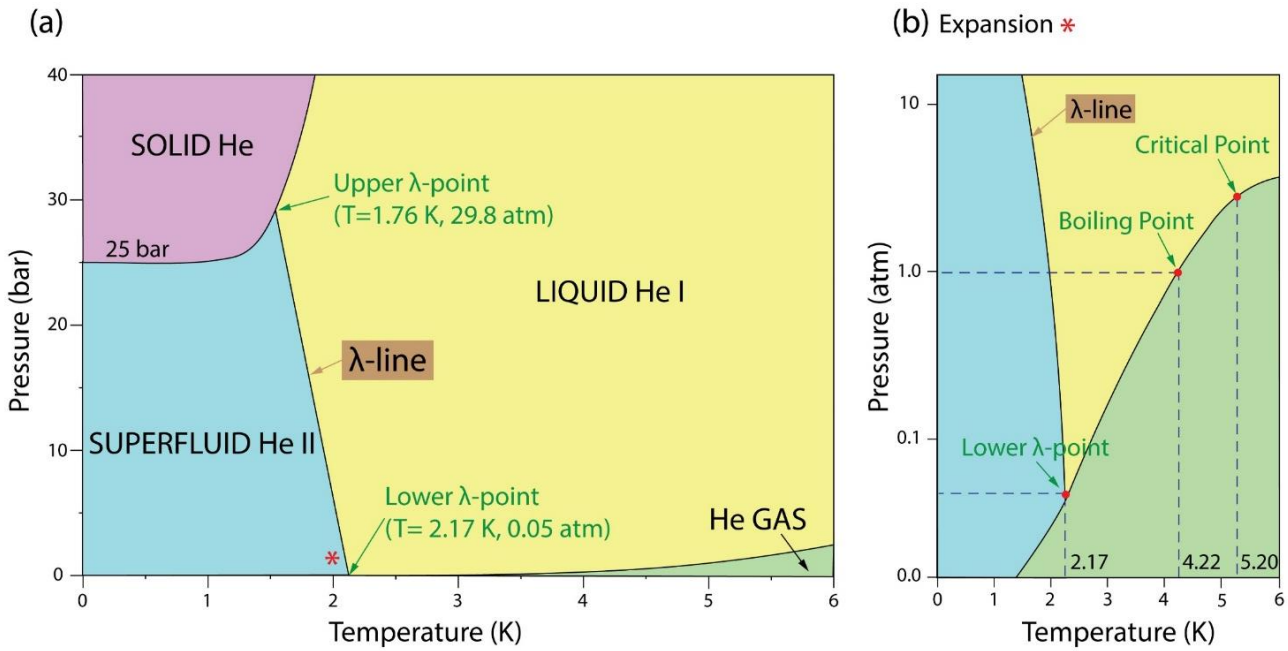

Fig. 1: (a) Phase diagram for helium (^{4}He) and (b) an expansion of phase diagram (a) about the lower λ-point.

At atmospheric pressure, helium liquefies from the gas phase into the He I phase at ~4.2 K and behaves like a normal Newtonian fluid. Upon further cooling, helium crosses the λ-line and transitions from the He I phase to the He II phase. The superfluid He II phase was first discovered in 1938 when techniques to reach cryogenic temperatures below 4.2 K were developed.[9] Tisza and Landau proposed the He II phase is fractional, consisting of both the He I and He II phases.[10,11] This so-called 'two-fluid model' was experimentally proven by Andronikashvili in 1946 who measured the oscillation frequency (f_n) of a stack of disks suspended in He I/He II.[12,13] Incorporation of fluid between the discs changes the mass and increases the moment of inertia (I), which equation 1 shows is inversely proportional to f_n.

$$f_n = \frac{1}{2\pi}\sqrt{\frac{k}{I}} \tag{1}$$

Here, k is the torsional constant. Classically, the oscillation frequency decreases when the temperature is reduced as I increases when the fluid becomes denser. Instead, I decreases until reaching 0 at 0 K, indicating fractional growth of the superfluid phase. When a container of superfluid helium is rotated, the superfluid helium does not follow the motion of the container like a normal fluid. Instead, the superfluid appears to remain stationary. Therefore, as the superfluid fraction begins to develop below 4.2 K, it does not follow the disc's oscillation. Only the normal fraction contributes to the oscillation frequency and is continually depleted as the system is converted to the He II phase. As this happens, the normal fractions contribution to I is reduced causing f_n to increase, until at 0 K when the disk stops rotating as the He I phase has been completely converted to the He II phase. Andronikashvili represented the change using density ratios. Dividing the density of the superfluid fraction (ρ_s) by the total density measured (ρ_t) gives the superfluid fraction (F_s), from which the liquid fraction (F_l) can be derived:

$$F_s = \frac{\rho_s}{\rho_t} \qquad \text{and} \qquad F_l = 1 - F_s \tag{2}$$

The density ratios of both fractions are plotted against temperature in Fig. 2, alongside an illustration of Andronikashvili's experiment. Along the temperature axis, T_λ represents the temperature at which the λ-line is crossed. Above T_λ, all the fluid is in the He I phase with F_s = 0 and F_l = 1. Below T_λ, the density of the liquid decreases, causing F_l to fall, while the corresponding superfluid density rises until F_s = 1 and F_l = 0 at 0 K.

Formation of the superfluid fraction involves condensation of helium atoms into a Bose Einstein Condensate (BEC). A BEC is a system in which all the particles share the same ground state, and hence can be described by a single macroscopic wave function. Formation of this highly ordered system is only possible at very low temperatures and only applies to bosonic particles with no net spin. Helium satisfies both conditions and below the boson formation temperature (T_B) at ~T_λ, the ^{4}He atoms start to condense into the ground state and become indistinguishable. Fermions cannot form a BEC as the Pauli Exclusion Principle prevents particles with net spin occupying the same space. For

this reason, fermionic ^{3}He is not superfluid at the same temperature as ^{4}He, but will eventually become superfluid below 3 mK when ^{3}He atoms pair to form binary bosons. Because all the ^{4}He atoms are identical in the BEC, they have the same energy, and so cannot be excited by interactions between atoms. Therefore, the total energy is conserved during motion, producing a macroscopic frictionless 'superfluid' that can creep against the force of gravity.

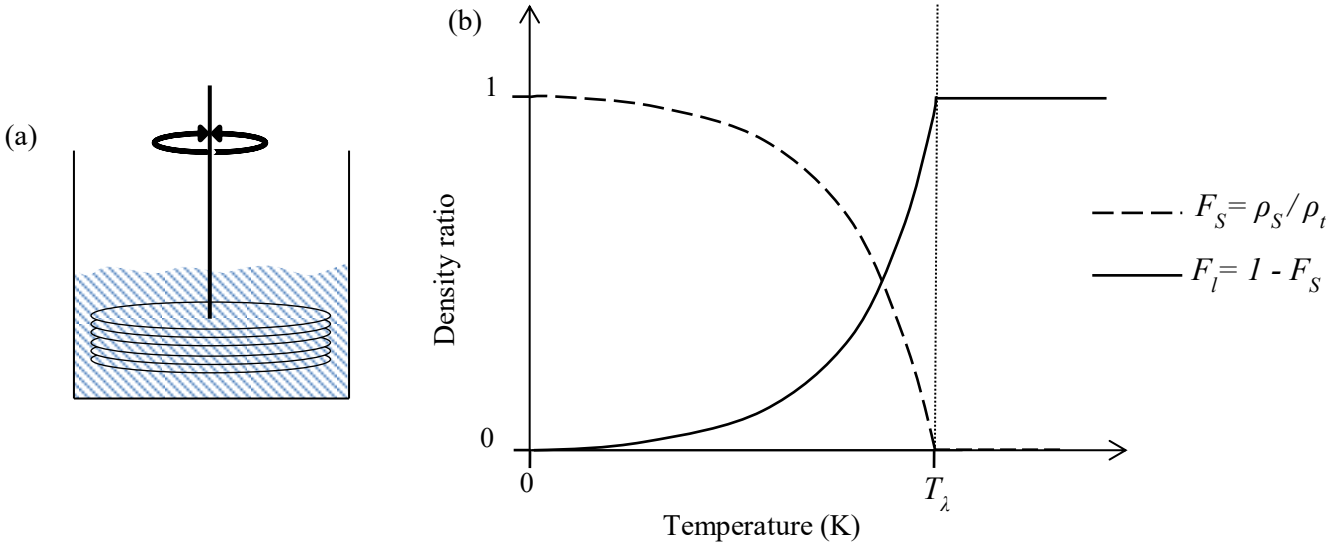

Fig. 2: (a) An illustration of Andronikashvili's rotating disc experiment. (b) A plot of the density of the normal and superfluid fraction vs. temperature. The transition temperature (T_λ) when the superfluid fraction begins to form is indicated by the dotted line on the temperature axis.

1.1.2 Properties of superfluid helium droplets

Viscosity and free dopant migration

Superfluidity is largely responsible for the unusual properties of HeDs. Superfluidity in bulk helium has been known for a while, but was only recently discovered in HeDs when Toennies and co-workers showed dopants could be captured inside droplets.[14] By comparing the infrared spectra of a single OCS molecule in ^{4}He and ^{3}He droplets, to the infrared spectrum of free OCS in a seeded Ar beam, Toennies *et al.* proved superfluidity existed in HeDs.[4,15] Fig. 3 shows the three spectra. The ^{4}He droplet spectrum (b) has

rotationally resolved P and R branches and is almost identical to the gas phase spectrum (a). The only difference is a shift in the rotational frequency because the rotational constant is slightly quenched by the helium atoms following the molecules' rotation.[16] In contrast, the ^{3}He droplet mass spectrum (c) shows no rotational resolution. This is because the stable droplet temperature is 0.37 K; far greater than the temperature required for ^{3}He to become superfluid.[15] From this it was deduced that ^{4}He droplets are superfluid as OCS could essentially rotate like a gas phase molecule. The rotational effect of the solvating helium atoms on the dopant species has been shown to vary for different molecules.[17] However, the extremely low viscosity that arises from superfluidity means all species are able to freely migrate inside the droplet, relatively unhindered by the surrounding helium atoms.

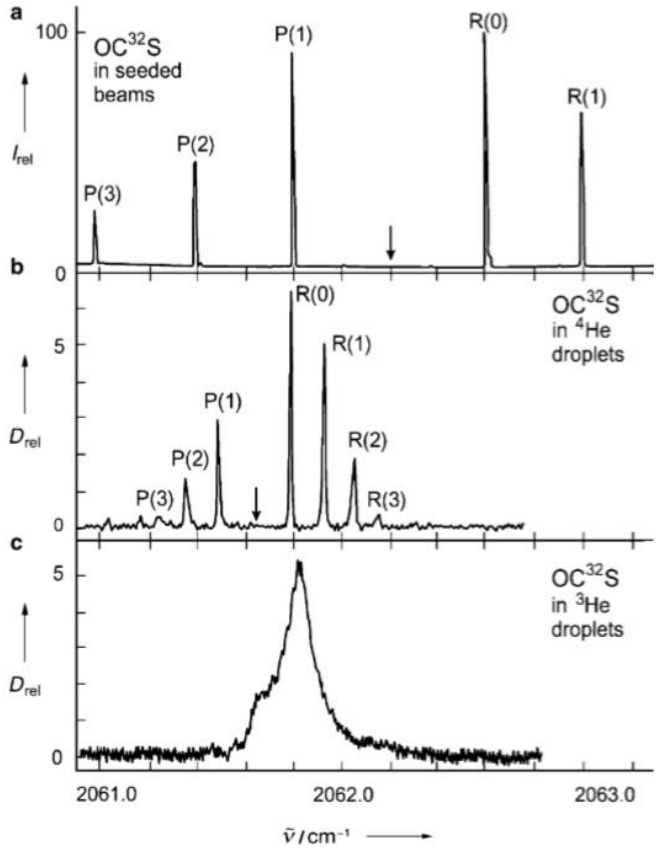

Fig. 3: The rotational spectra of $OC^{32}S$ in three different environments. (a**)** The spectrum of free $OC^{32}S$ in an Ar seeded beam; (b) the spectrum of $OC^{32}S$ in ^{4}He droplets; and (c) the spectrum of $OC^{32}S$ in ^{3}He droplets. From ref. 5.

High thermal conductivity

When dopants are added to HeDs, they are rapidly cooled to the internal droplet temperature of 0.37 K. This is due to the droplets' ultra-high thermal conductivity, which is about 30 times greater than copper.[5] Rapid energy dissipation occurs by evaporation of surface helium atoms. This occurs readily due to the weak binding energy between helium atoms, resulting in cooling rates estimated to be as high as 10^{16} K s^{-1}.[18,19] Each 1 eV of energy delivered to the droplet causes ~1600 atoms to be evaporated from the surface, making size an important consideration when adding multiple species to HeDs.[3] Formation of large clusters by addition of multiple dopants requires a large droplet size to prevent complete evaporation. Rapid energy dissipation means cluster formation involves addition of dopants to a pre-cooled cluster nucleus as the excess internal energy has already been dissipated before the next dopant species reaches the cluster nucleus. This can lead to the formation of metastable species as rapid energy dissipation causes structures to become trapped in shallow potential wells along the potential energy surface. There is not enough energy at 0.37 K for the structure to rearrange to a more stable state allowing it to exists long enough to be studied. Therefore, the HENDI technique has helped provide experimental evidence for the existence of high energy structures that have previously only been predicted computationally.[20]

Near-unity pick-up

Despite both displaying superfluidity, studies of dopants in HeDs have been far more extensive compared to in bulk helium. The reason is simply that bulk helium is a terrible solvent. Dopants generally tend to fall to the bottom of the container or reside at the walls. However, in HeDs there are no container walls to prevent solvation, and once captured, the dopant remains inside the droplet, most likely residing in the centre where the potential is at a minimum.[21] Dopants are captured with near-unity pick-up probabilities meaning if a dopant encounters a droplet, it will almost certainly be 'picked-up'. Depending on the number of dopants in the pick-up region, single or multiple dopants can be added to the droplets. The pick-up probability (P_k) is described using Poisson statistics[22]:

$$P_k(z) = \frac{z^k}{k!} \exp(-z) \tag{3}$$

In equation 3, k is the number of species picked-up and $z = \sigma n l$ is the pick-up parameter. The pick-up parameter is calculated using σ - the pick-up cross section (i.e. the size of the droplet), n - the number of dopants in the pick-up zone and l - the length of the pick-up zone. Maximising one or more of these parameters increases the pick-up probability and allows control over the number of dopants captured, which ranges from single, to thousands of atoms, molecules or ions. The exception to near-unity pick-up is alkali metal atoms and clusters. They are not incorporated inside the droplets because of the large Pauli repulsion between the diffuse electron systems and the surface helium atoms, that is not compensated for by forming alkali-helium bonds.[23] However, above a certain cluster size, the alkali cluster will eventually dissolve.[24,25]

Quantized vortices

One of the most bizarre properties of the He II phase is quantized vortex formation. As discussed earlier, instead of rotating as one body like a normal Newtonian fluid, the He II phase appears to remain stationary. The superfluid still 'rotates' but in the form of quantized vortices. Quantized vortices were first proposed by Onsager, and later suggested by Feynman to involve many vortex lines, around which the superfluid rotates with quantized circulation (κ).[26–28] Equation 4 shows the expression for κ, determined from the integral of the flow velocity (v) along an enclosed loop (s).

$$\kappa = \int v.ds = n\frac{2\pi\,\hbar}{m_{He}} \tag{4}$$

In this equation, m_{He} is the mass of a helium atom, ħ is the reduced Planck constant and n represents the quantum state (i.e. n = 0, 1, 2…etc.) of the vortex. Circulation about the vortex core (estimated to be ~1 Å in diameter) is quantized in units of $\frac{2\pi\,\hbar}{m_{He}}$.[29,30] Packard *et al.* provided the first visual proof of quantized vortex lines in bulk helium by 'pinning' electrons to vortices, which were then imaged by accelerating the electrons onto a phosphor screen.[29,31] The resulting image showed circular arrays, where each spot represented a vortex line. Pinning or 'trapping' occurs as the circulation produces a pressure gradient across the vortex, creating a weak attractive potential of 2-7 cm^{-1}.[32]

Recently, trapping of particles along vortex lines has been discovered in HeDs providing the first evidence of quantized vortex formation at the droplet level.[33]

1.2 Helium droplet mass spectrometry

Helium droplet electron ionization mass spectrometry is different to conventional gas phase electron ionization mass spectrometry in a number of ways. In the gas phase, an electron of energy ~70 eV directly impacts the molecule removing an electron and forming the positive parent ion. The excess energy delivered to the parent ion results in subsequent fragmentation to produce daughter fragments. The ionization energy of simple alkanes and alcohols is typically around ~10 eV. The excess energy is substantive causing majority of the parent ion to fragment into daughter fragments. Conversely, helium droplet electron ionization is indirect as the initial electron impacts a surface helium atom first. This produces a surface He^+ ion which then 'hops' to the dopant in the centre of the droplet via a resonance charge hopping mechanism.[34,35] Charge localisation on the dopant must occur within 10 hops, otherwise 'self-trapping' occurs resulting in the formation of He_2^+.[36,37] Hence, the intensity of the parent ion peak in the helium droplet mass spectrum depends on the size of the droplet. The intensity of the parent ion peak decreases with increasing droplet size, until it eventually disappears as the dopant is more than 10 hops away from the surface of the helium droplet, leading to the formation of only He_2^+. He_n^+ (where n>2) clusters also appear in the mass spectrum as a result of nucleation of helium atoms around He_2^+. To avoid self-trapping, HeDs containing less than 10^4 atoms are used in helium droplet electron ionization experiments. Alternatively, ionization can occur via Penning ionization where an electronically excited He* atom initially forms on the surface. Following collision with a ground state He atom, He^+ is produced. However, Penning ionization only dominates in large HeDs (>10^5 atoms) where there are enough surrounding helium atoms to cause double Penning ionization to produce He_n^+.[38,39] Therefore, only resonance charge hopping is considered here. In resonance charge hopping, both charge transfer to the dopant and self-trapping are exothermic processes. Consequently, the excess energy released causes the droplet to explode by rapid evaporation of the surrounding helium atoms, ejecting the ions from the droplet. As the illustration in Fig. 4 shows, helium droplet ionization can be summarised into three steps: (1) surface ionization of a He atom, (2) charge hopping to dopant (or until self-trapping) and (3) ion ejection from the helium droplet.

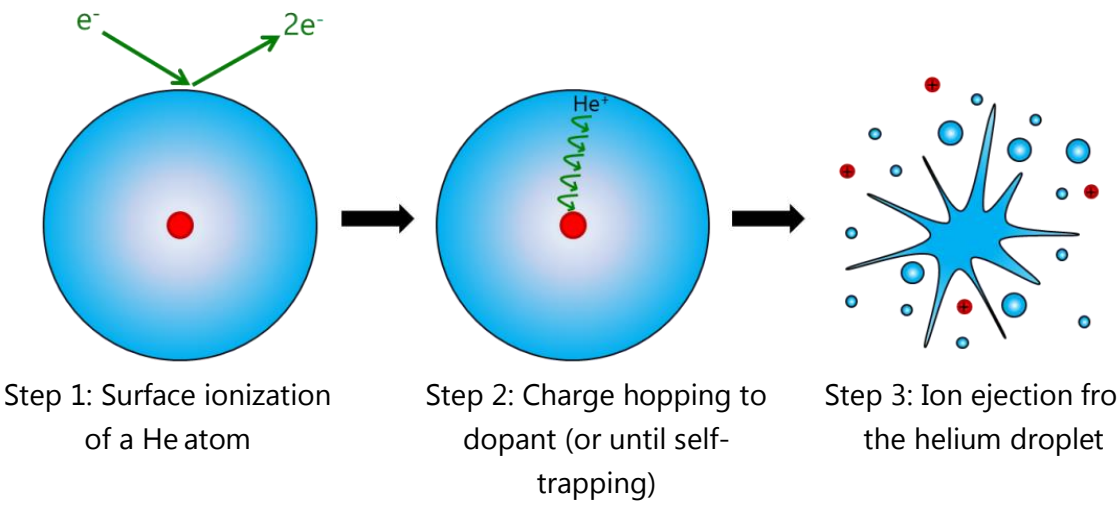

Fig. 4: Illustration of the three main steps of the helium droplet electron ionization process. The red circle in step 1 and 2 represents the dopant. The red cations in step 3 represent the dopant fragments.

Because helium droplet ionization is an indirect process, it was considered as a potential 'soft' ionization technique for molecules which heavily fragment upon electron ionisation. In each step in the ionization process, there are routes by which the initial 70 eV electron impact energy can be quenched. Firstly, surface ionization of a He atom removes a significant amount of energy as the first ionization energy of helium is 24.6 eV. As the surface charge hops between helium atoms, the excess energy delivered to the droplet is further reduced. Upon charge localisation, the energy is reduced further because of the energy required to ionize the dopant. This means for a simple alcohol with an ionization energy of ~10 eV, the excess energy can be reduced from 70 eV to 15-16 eV.[40] Finally, the remaining energy can also be dissipated by helium atom evaporation which occurs rapidly due to the weak helium-helium binding energy.

Evidence for softening has been investigated using various molecules with mixed results. Early studies with nitrogen monoxide (NO) dimers showed soft ionisation. Where the NO parent ion is completely obliterated in the gas phase electron ionization spectrum, a strong parent ion peak was retained in the helium droplet spectrum.[41] The helium droplet mass spectrum of triphenylmethanol also suggests a softening effect is present and was shown to be dependent on droplet size.[42] In addition, the cyclic alcohols, such as cyclopentanol and cyclohexanol, displays substantial softening with the parent ion becoming a major fragmentation peak compared to in the gas phase

where it is barely visible. This can be seen in Fig. 5 for cyclopentanol. However, with other molecules, very little or no softening has been observed. This includes aliphatic alcohols, ethers and haloalkanes, all of which have been studied by the Spectroscopy and Dynamics Group at the University of Leicester. Aliphatic alcohols (e.g. ethanol, *n*-butanol, 1-pentanol and 2-propanol) and ethers (e.g. diethyl ether, diisopropyl ether and methyl t-butyl ether) display similar parent ion peak intensities to the gas phase.[40] However, one important difference for many of these molecules is an increase in the proton loss peak. Taking the mass spectra for n-butanol in Fig. 6 as an example, it can be seen that the parent ion peak is only marginally enhanced in the helium droplet mass spectrum compared to in the gas phase. In contrast, the M-1 peak sees a dramatic enhancement, along with a number of the other daughter fragment peaks. This reflects a typical example of the changes in the fragmentation ratios which are often observed when switching the ionization environment from the gas phase to a helium droplet. Mono-, di- and tri- substituted haloalkanes display even fewer differences between their helium droplet and gas phase mass spectrum showing the helium droplet is unable to sufficiently quench the excess ionization energy.[43] As with aliphatic alcohols and ethers, loss of small radical fragments became more favourable, supressing the intensity of peaks produced by C-C bond breaking or hydrogen halide loss channels. From these studies, it was concluded that helium droplet electron ionization is molecule dependent and cannot reliably reduce parent ion fragmentation for every molecule.

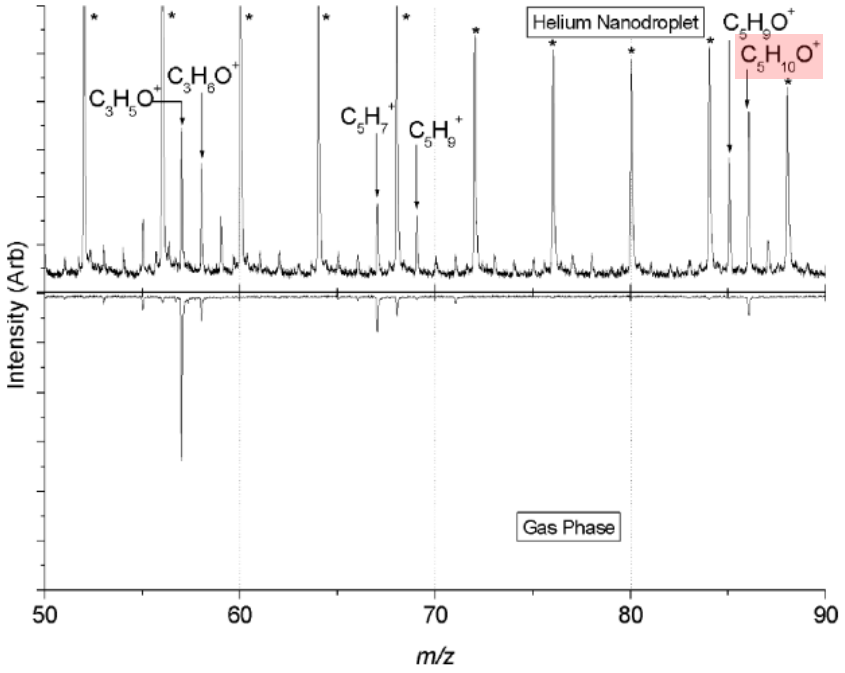

Fig. 5: The helium droplet (TOP) and gas phase (BOTTOM) electron ionization mass spectrum of cyclopentanol. The peaks marked with an asterisk (*) are the He_n^+ cluster peaks which were not subtracted from the helium droplet mass spectrum due to noise variation created by pulsed nozzle conditions. The $C_5H_{10}O^+$ peak highlighted in RED is the parent ion peak at m/z 86 and is noticeably enhanced in the helium droplet mass spectrum as a consequence of softening effects. From Ref. 40.

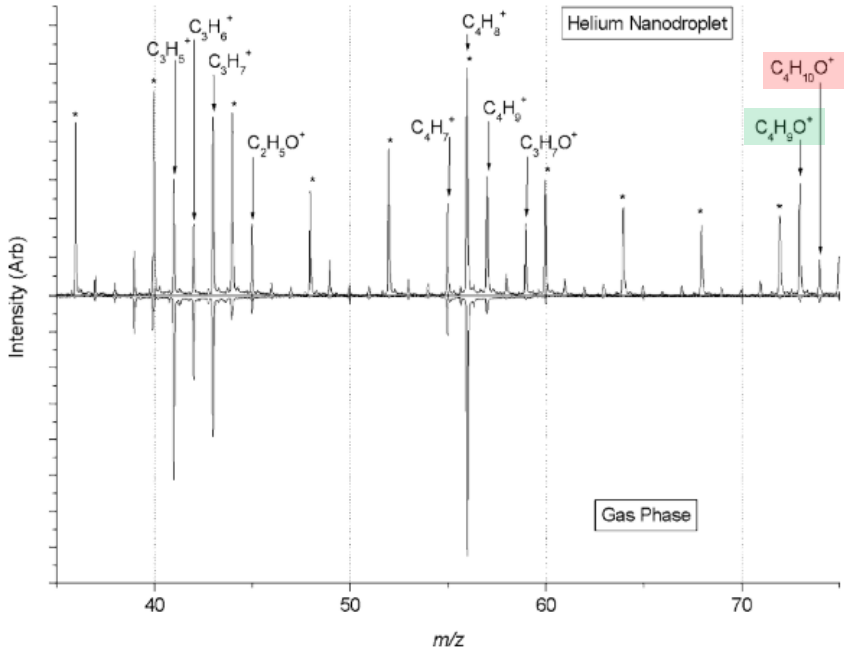

Fig. 6: The helium droplet (TOP) and gas phase (BOTTOM) electron ionization mass spectrum of n-butanol. The peaks marked with an asterisk (*) are the He_n^+ cluster peaks and were not subtracted from the data for the same reason in Fig. 5. The $C_4H_{10}O^+$ peak highlighted in RED is the parent ion peak at m/z 74 and the $C_4H_9O^+$ peak highlighted in GREEN is the M-1 peak at m/z 73 corresponding to proton loss. From Ref. 40.

Despite the reduction in the excess energy, it is thought that extensive parent ion fragmentation still ensues for certain molecules as a result of the timescales for helium evaporation vs. parent ion fragmentation. Although HeDs have an amazing ability to dissipate energy, if the rate of helium evaporation is slower than the rate at which the molecule fragments, the majority of the excess energy is retained by the parent ion resulting in extensive fragmentation. The rate of evaporation depends on size and is only significant in small HeDs.[42] Therefore, partial softening is most likely for small HeDs doped with molecules which fragment on a timescale that is longer than the rate of helium evaporation. It is also thought slow fragmentation rates are more common for large molecules, explaining why the majority of small alcohols, ethers and haloalkanes showed no softening effects in their helium droplet mass spectra.[40]

As noted earlier, even if softening is not observed, changes in the fragmentation ratios between the daughter fragment peaks are common occurrences. Typically, peaks created by loss of small neutrals or radicals from the parent ion gain in intensity, resulting in a corresponding reduction in peaks produced from loss of large neutrals/radicals. Loss of small species is believed to become more favourable in the helium droplet matrix because of 'cage effects'. During the ejection process, the helium atoms around the parent ion can exert a 'cage', whereby helium atoms are strongly attracted to the parent ion through ion induced dipole forces.[40,43,44]. This produces a significant energy barrier and makes the ejection of small radical fragments more favourable. Hence, explaining why an increase in the proton loss fragmentation peak is a common observation as a proton is the smallest possible radical that can escape through the helium matrix.

There have been few helium droplet mass spectrometry studies of simple conjugated and or aromatic molecules. Studies which have investigated aromatics such as toluene, coronene and benzene, have either looked at clusters or reactions with other molecules inside the helium droplet.[45–47] There is little evidence of anyone looking at the fragmentation of single conjugated/aromatic molecules in HeDs. Recently, the helium droplet mass spectrum of p-benzoquinone was recorded with the pick-up conditions adjusted so the majority of the peaks in the mass spectrum were produced from fragmentation of the monomer. This spectrum displays a completely different behaviour to the trends described above. Instead of partially 'softening' ionization or causing little change, ionization actually appears to become 'harder' inside the helium droplet, with the parent ion peak almost completely reduced compared to in the gas phase mass

spectrum. A reduction in the parent ion peak has not been reported before. This unusual behaviour is believed to be a result of the nature of the conjugated molecule, and the play off between the 'cage effect' and most energetically favourable fragmentation pathway. Studying this system could reveal more information about the helium droplet fragmentation process and the influence the helium matrix has on ions isolated inside the droplet. The following presents the experimental results for the p-benzoquinone helium droplet mass spectrometry experiment, along with a theory to explain the observed fragmentation pattern. Density functional theory calculations were performed to support the theory and extended to other simple aromatics to predict whether their helium droplet mass spectrum will be similar to p-benzoquinone.

2. Experimental

2.1 Experimental set-up for recording the helium droplet electron ionization mass spectrum of p-benzoquinone

The typical set-up for all HENDI experiments involves a modular ultra-high vacuum (UHV) system comprised of three main chambers: (1) the source chamber, (2) the pick-up chamber and (3) the analysis chamber. The HENDI experiment in the Spectroscopy and Dynamics Group follows this design and has been adapted to perform helium droplet mass spectrometry. For this instrument, ultra-high vacuum is achieved using a collection of turbomolecular pumps backed by Scroll pumps to achieve oil-free UHV conditions. Very good UHV conditions are needed for HeDs experiments as droplets are sensitive to background gases (N_2, O_2, H_2O, CO_2 etc.) and impurities, especially during droplet formation. An illustration of the experiment is shown in Fig. 7 and in Fig. 8 there is a picture of the HENDI instrument showing the three chambers and vacuum equipment.

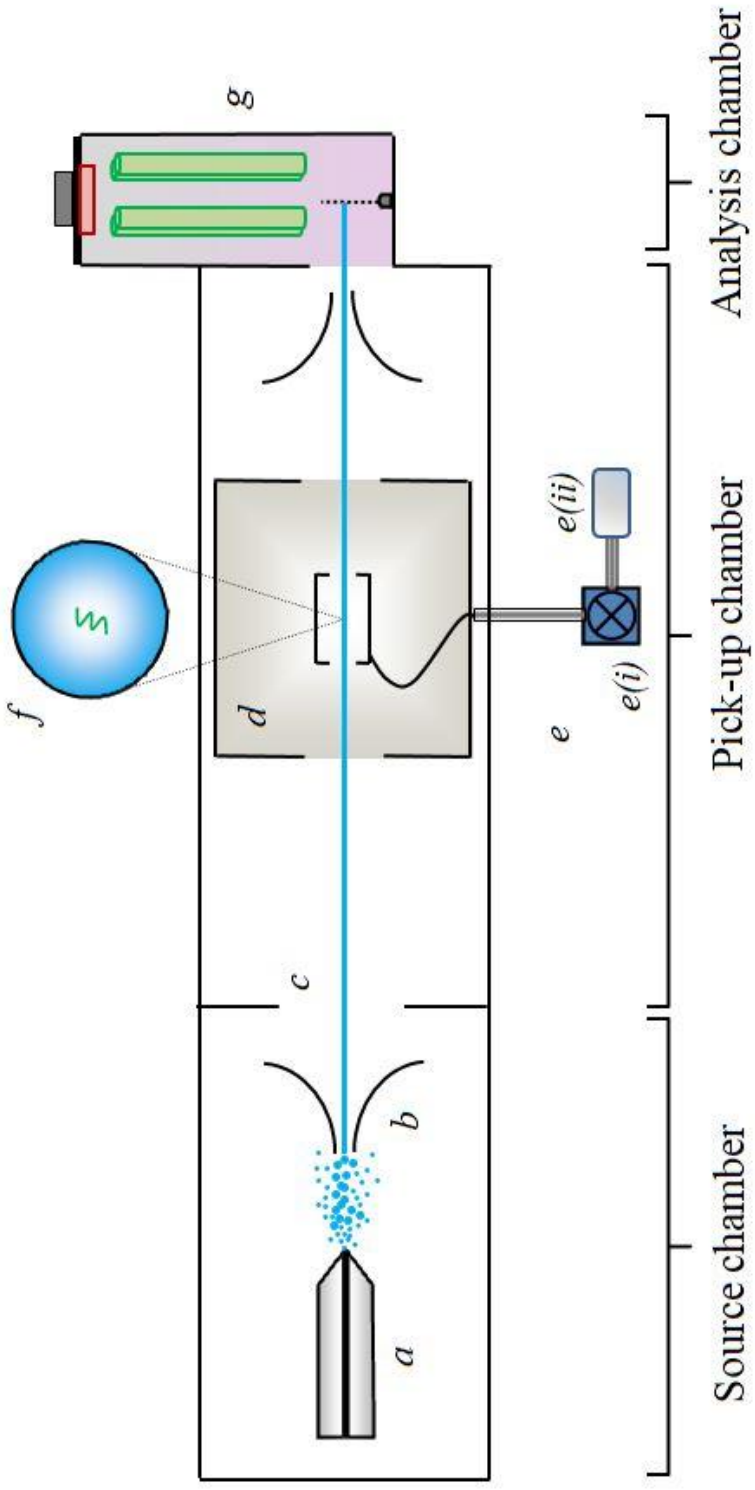

Fig. 7: Illustration of the experimental set-up for helium droplet mass spectrometry. The important features are as follows: (a) the cold head onto which the nozzle is mounted; (b) the skimmer; (c) the collimated HeDs beam; (d) the pick-up cell; (e) external doping of the HeDs where e(i) is the needle valve and e(ii) is the glass vial containing p-benzoquinone; (f) an expansion of a p-benzoquinone doped helium droplet and (g) the quadrupole mass spectrometer.

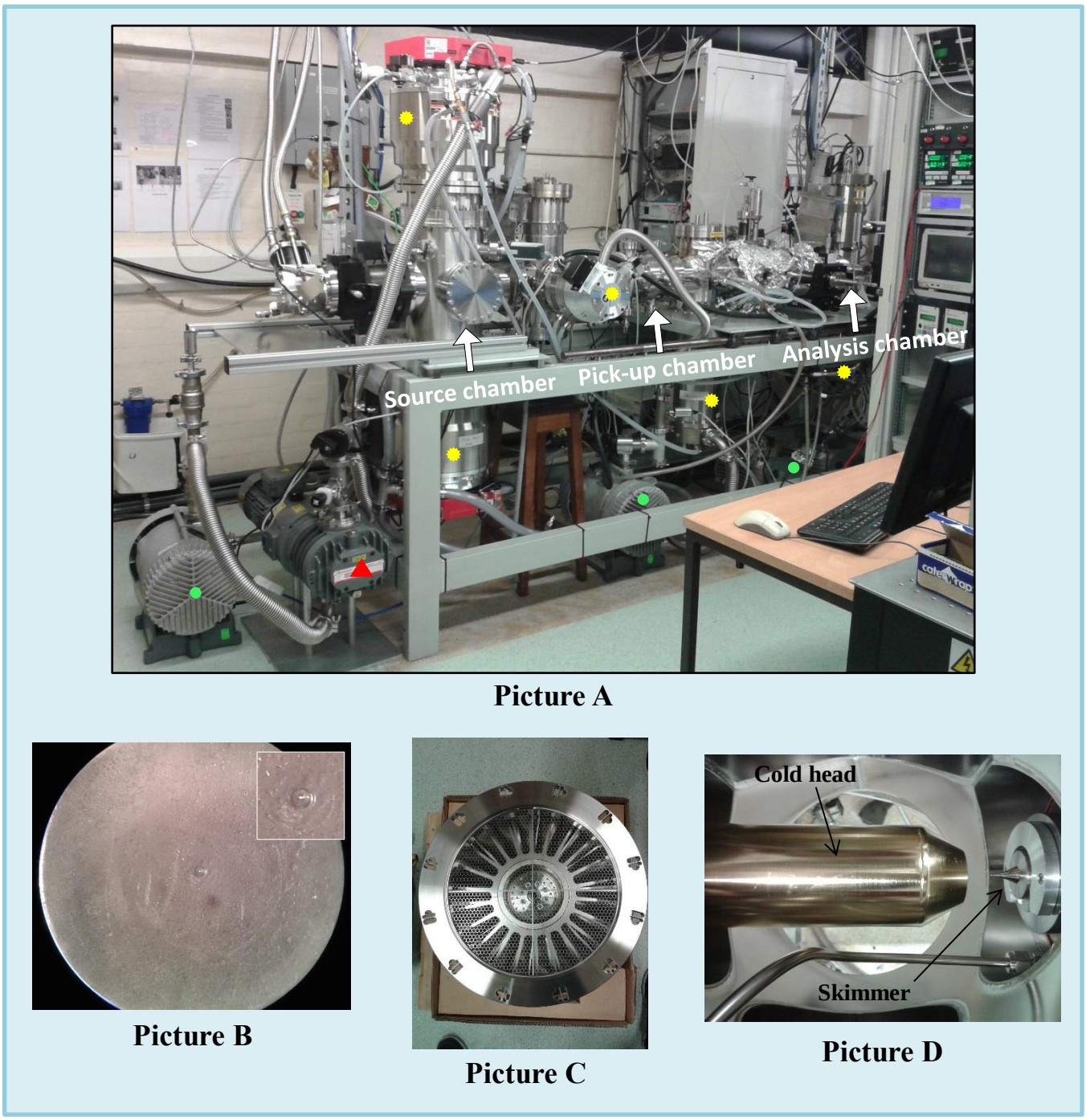

Fig. 8: Pictures of the HENDI instrument in the Spectroscopy and Dynamics Group.

Picture A – Image of the complete set-up from the HENDI, with the three chambers indicated in white text. The ultra-high vacuum system is comprised of turbomolecular pumps (●), backing Scroll pumps (●) and a roots pump (▲). The roots pump provides an additional boost to the pumping capacity in the source chamber.

Picture B – Picture of the 5 µm hole of the nozzle captured through the lens of a microscope.

Picture C – Inside of a turbomolecular pump.

Picture D – View of the cold head and the skimmer from inside the source chamber.

The source chamber is where HeDs are formed by expanding high purity (99.9999%) helium gas continuously through a nozzle 5 μm in dimeter (pictured in Fig. 8). The nozzle is mounted onto a cold head which is cryogenically cooled using a closed cycle cryostat to a set temperature. The temperature of the nozzle (T_N) and/or helium pressure (P_0) determines the type of expansion and ultimately the size of the HeDs. From expansion isentropes in Fig. 9, Toennies *et al.* have characterised three types of expansion for a helium pressure of 20 bar:[48]

- Subcritical expansion (T_N = 10-30 K) – Helium is forced through the nozzle as a gas and expands after leaving the nozzle orifice along an isentrope that crosses the critical point from the gas side. This forms droplets where the average helium droplet size, $\langle N_{He} \rangle$, is 10^3 to 10^4 atoms.
- Supercritical expansion (T_N = 6-10 K) – Expansion isentropes cross the critical point from the liquid side and emerge from the nozzle orifice as a liquid which breaks-up to form HeDs where $\langle N_{He} \rangle = 10^4$ to 10^7 atoms.
- Subsonic expansion (T_N < 6 K) – Expansion is no longer supersonic. Instead the expansion isentropes are subsonic at all points and have already crossed the critical isentrope before leaving the nozzle. Droplet formation occurs inside the nozzle by fragmentation of the liquid producing very large droplets where $\langle N_{He} \rangle$ exceeds 10^7 atoms. Below ~5 K, the liquid streams out of the nozzle as a continuous liquid jet and breaks apart due to Rayleigh instability to form the largest droplets containing more than 10^{10} atoms.[1,5]

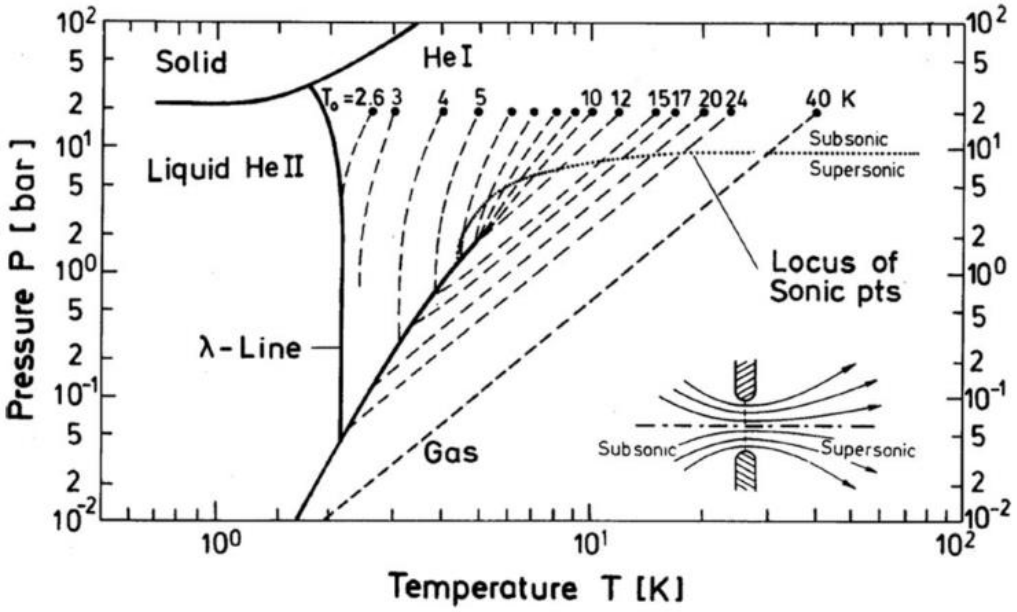

Fig. 9: Phase diagram of ^{4}He showing the various expansion regimes. The dotted lines are the expansion isentropes for various nozzle temperatures with a helium expansion pressure of 20 bar. Above 10 K, the expansion isentropes cross the critical point from the gas side. Below 10 K, the expansion isentropes cross the critical point from the liquid side until the temperature falls below 6 K and expansion becomes subsonic at all points. From ref. 1.

For mass spectrometry experiments, HeDs containing ~10^3-10^4 atoms are preferable as this ensures adequate pick-up probability whilst maintaining high signal intensity in the mass spectrum. Therefore, subcritical expansions were chosen using a nozzle temperature of T_N = 11 K and helium pressure of 20 bar producing HeDs containing $\langle He_N \rangle \sim 8.1 \times 10^3$ atoms.[49] After expansion, the droplets cool by evaporative loss of helium until they reach their steady state temperature of 0.37 K.[14] The HeDs are then collimated into a beam by aligning the nozzle with a skimmer (0.5 mm in diameter) positioned ~20 mm in front of the nozzle. Alignment is possible as the cold head is mounted onto a XYZ manipulator allowing 10 µm precision positioning of the nozzle. The skimmer in the source chamber is aligned with another skimmer between the pick-up chamber and analysis chamber allowing the HeDs to pass through the whole modular set-up.

After the source chamber, the helium droplet beam enters the pick-up chamber where it encounters dopants. The pick-up chamber consists of a series of cylindrical pick-up cells with a hollow centre so the HeDs can pass through. Solid dopants with low vapour pressures can be placed directly in the pick-up cell, and are often heated to increase the dopant partial pressure to ensure sufficient pick-up. However, the vapour pressure of p-

benzoquinone is too high meaning it would evaporate too quickly under ultra-high vacuum conditions. Therefore, the molecule was introduced to the pick-up cell from a glass cell connected to the UHV pick-up cylinder via a stainless steel tube that could be isolated using a valve. During the experiment, an additional needle valve was used to control the flow of the p-benzoquinone vapour to the pick-up cell. The needle valve was adjusted so the helium droplet mass spectrum contained predominantly the monomer p-benzoquinone peaks, with little contribution from the dimer. This low pick-up probability was achieved without heating or cooling the glass cell.

Finally, the doped HeDs pass into the analysis chamber. Here, they are ionized using an electron ionization energy of 64 eV and the ions are detected in a quadrupole mass spectrometer. The helium droplet mass spectra were recorded using a mass range of 6-800 m/z and the data was analysed in OriginPro 8. Processing the data involved subtracting the background helium droplet spectrum from the helium-p-benzoquinone mass spectrum to remove the He_N^+ cluster and background gas peaks (see Appendix A for background HeDs mass spectrum). The p-benzoquinone region of the spectrum was then selected and smoothed using the adjacent averaging method. The gas phase mass spectrum of p-benzoquinone was obtained from the NIST database. Attempts were made to record the gas phase spectrum experimentally. These attempts used two approaches. The first approach was to isolate the source chamber from the pick-up chamber so only p-benzoquinone was able to reach the analysis chamber. The second approach involved keeping the source chamber open but with the nozzle at room temperature. The idea behind this was the helium gas from the nozzle would serve as a carrier gas for p-benzoquinone, transporting it to the analysis chamber. However, with both approaches p-benzoquinone could not be detected by the QMS. This indicated the molecules mean free path was too short to reach the analysis chamber without helium droplets. Therefore, it was not possible to record the gas-phase mass spectrum using the current set-up. Yet this could have been achieved if the pick-up chamber was shorter and p-benzoquinone was injected into the analysis chamber in a seeded rare gas beam.

2.2 Density Functional Theory calculations on the fragmentation pathways of conjugated molecules

Density functional theory (DFT) is a quantum mechanical method developed from the proof provided by Hohenberg and Kohn in 1964.[50] This proof showed that the ground

state electronic energy of a many-body system can be determined from the electron density. Using the electron density to define the system and not the wavefunction provides more accurate results compared to other quantum mechanical methods such as Hartree-Fock theory. In Hartree-Fock theory, a degree of error is introduced by evaluating electronic wavefunctions individually and representing electron repulsion as an average.[51] In DFT theory, the electronic energy is obtained using a density functional which is a function of the function for the electron density. Density functionals do not have an exact form meaning there is a whole range of different functionals that can be used to obtain the energy. For this project, the hybrid Becke, 3-parameter, Lee-Yang-Parr (B3LYP) functional was chosen as it provides good computational efficiency and is commonly applied to gas phase organic molecules.[52] The B3LYP is called a hybrid functional as it combines both the exchange-correlation energy terms from Hartree-Fock theory and other *ab initio* or empirical methods.

The fragmentation pathways of the conjugated/aromatic molecules upon electron ionization were studied in Gaussian16 using the B3LYP functional and the cc-pVTZ basis set for all calculations. The following procedure was followed for each molecule. Firstly, the ground state structure was optimized using an optimization and frequency calculation to represent the molecule before ionisation. The ionization energy was then determined from a single point calculation using the coordinates for the ground state structure, but charge and multiplicity changed to 1 and 2, respectively. Therefore, vertical ionization was assumed and the structure in the single point calculation taken as the parent ion structure. Relaxed potential energy scans were used to obtain a 'guess' structure for the first transition state in each of the main initial fragmentation pathways. The guess transition state geometry was then optimized and identified as a transition state from the single negative vibrational frequency. Intrinsic reaction coordinate (IRC) calculations were performed using the transition state geometry. An IRC calculation follows the minimum energy reaction pathway between the transition state and its reactants and products, but will not proceed all the way. Therefore, by optimising the final structure on either side of the IRC curve, the starting reagent structure and the product of the fragmentation step should be obtained. If this happened, then the correct transition state structure had been located. If the product structure was an intermediate, the calculations were repeated using the same method until fragmentation was complete. Appendix B provides example input files for the calculations.

3. Results and Discussion

3.1 Helium droplet vs. gas phase electron ionization mass spectrum of p-benzoquinone

The helium droplet and gas phase electron ionization mass spectrum of p-benzoquinone are compared in Fig. 10. It is instantly noticeable that the main fragmentation peaks in both spectra are the same, but the relative intensity of the peaks is very different. In the helium droplet spectrum, the parent ion signal has the weakest intensity and the m/z 54 peak is most prominent. This is different to in the gas phase mass spectrum where the parent ion peak is most dominant.

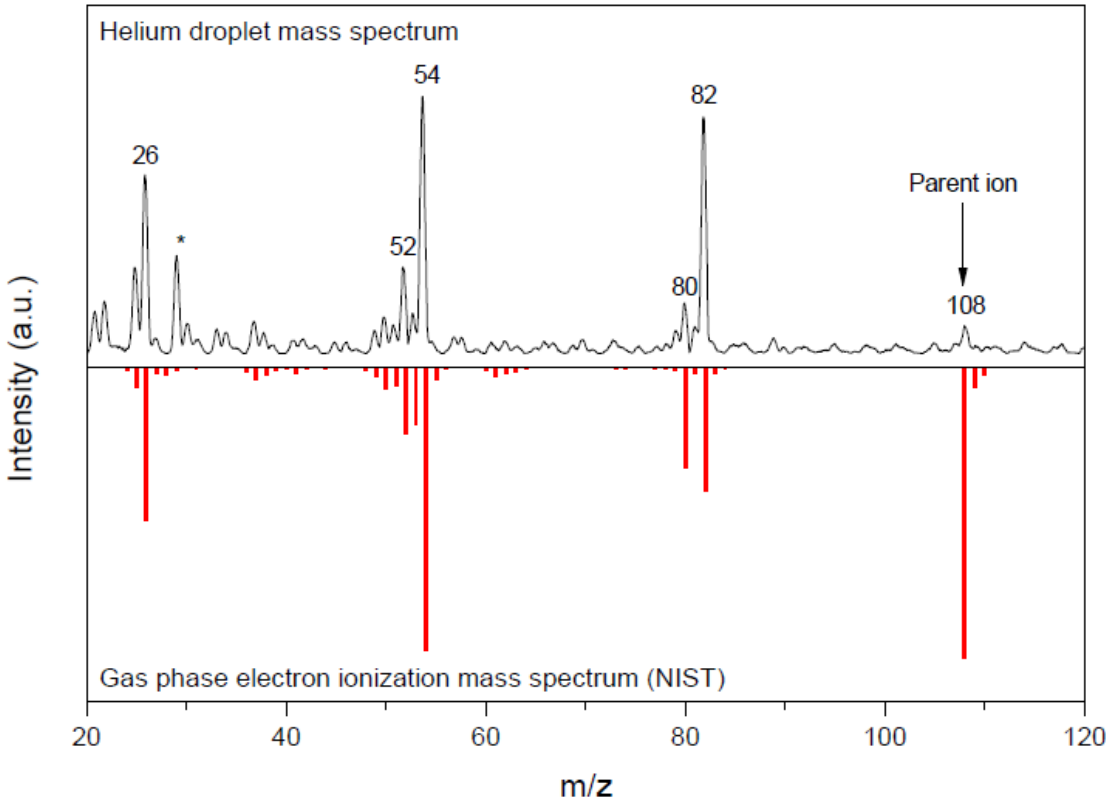

Fig. 10: The helium droplet (TOP) and gas phase (BOTTOM) electron ionization mass spectrum of p-benzoquinone. The gas phase mass spectrum was taken from the NIST database. The parent ion is the m/z 108 peak, and is clearly reduced in the helium droplet mass spectrum. The helium droplet electron ionization mass spectrum was recorded using T_N =11 K and P_0 =20 bar. In the helium droplet spectrum, the peak marked with an asterisk (*) is the N_2 peak which could not be totally subtracted from the background due to an increase in the N_2 signal from background gases in the stainless steel tubing and needle valve. This is because unlike the main chamber, the external glass cell and needle valve could not be baked due to o-ring fittings.

The intensity changes between the spectra in Fig. 10 are unusual for a number of reasons. Firstly, as a general 'rule of thumb' aromatics and conjugated molecules such as quinones typically show a very strong parent ion peak because the positive charge can be stabilized by π-electron system, making fragmentation less favourable.[53,54] Yet, in the helium droplet mass spectrum it is apparent fragmentation became more favourable, causing p-benzoquinone to break apart into its daughter fragments. Secondly, although the 'softening' effect of HeDs has been shown to be molecule dependent, a reduction in the parent ion signal has not been observed before. Neither is it expected, because as explained in the introduction, less energy is delivered to p-benzoquinone upon helium droplet electron ionisation. In addition, evaporative loss of helium will also quench some excess energy; and even though the timescale for helium evaporation may be longer than the fragmentation process, it should still help to partially increase the parent ion signal. Therefore, the parent ion signal is predicted to at least marginally increase, if not remain the same as in the gas phase. This suggests there is something very different going on during the fragmentation process.

3.2 DFT calculations on the initial fragmentation pathways of p-benzoquinone

A first hint suggesting why p-benzoquinone behaves differently during helium droplet ionization comes from looking at the main fragmentation pathways. Quinones dissociate by successive loss of either CO or C_2H_2 causing in ring contraction until C_2H_2 is formed (assuming dissociation proceeds fully). The overall dissociation process is shown in Fig. 11.

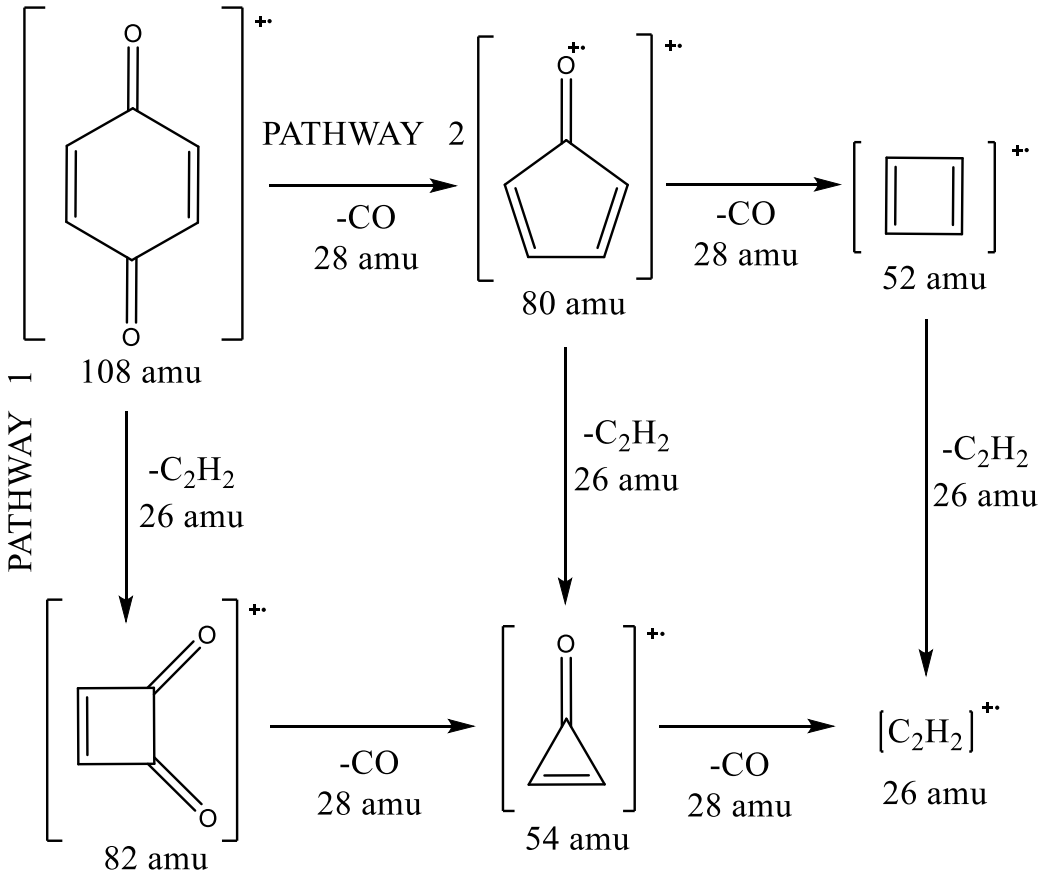

Fig. 11: Main dissociation pathways of p-benzoquinone upon electron ionisation. The mass of each fragment is displayed underneath the structure.

As seen in the scheme above, there are two main initial fragmentation pathways involving either CO loss or C_2H_2 loss. The mass of the fragments from both these pathways agrees with the peaks in the mass spectra in Fig. 10. The peaks at m/z 82 and m/z 80 are the primary daughter fragments produced from C_2H_2 loss and CO loss, respectively. The intensity of the m/z 82 peak is significantly more intense in the TOP helium droplet spectrum in Fig. 10, implying pathway 1 is more favourable. One notable feature about the dissociation process in Fig. 11 is the lack of a proton loss peak. An M-1 peak is not observed in either the gas phase or helium droplet mass spectrum suggesting C_2H_2 is the lightest neutral which can be lost from the parent ion. To understand why proton loss is not favourable, DFT calculations were performed to determine the reaction energy profile for removal of a proton from the ring. For comparison, the reaction energies for pathway 1 and pathway 2 were also calculated. The results are presented in Fig. 12.

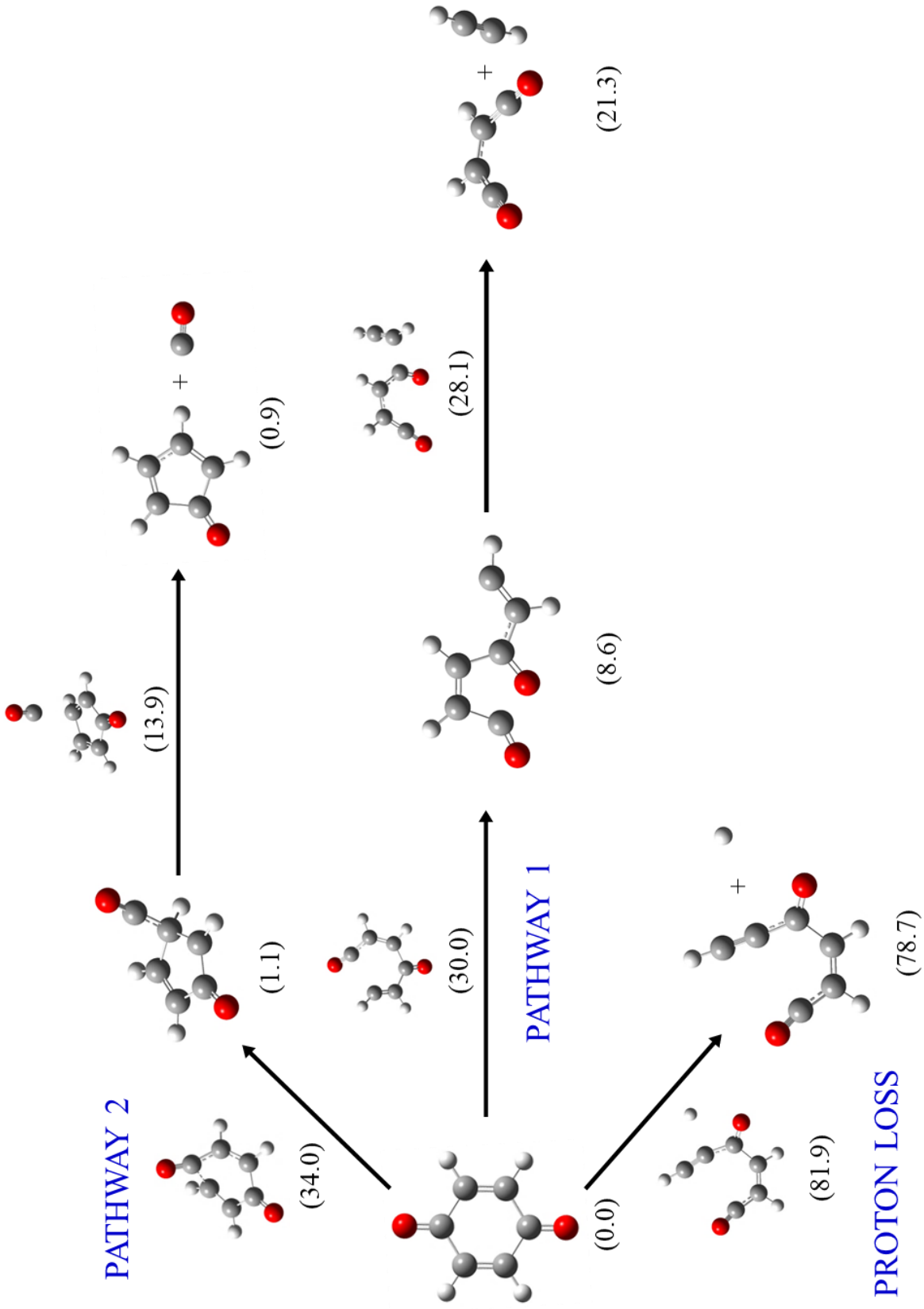

Fig. 12: Results from DFT calculations showing the reaction energy profiles of the three initial fragmentation pathways investigated for p-benzoquinone: C_2H_2 loss (pathway 1), CO loss (pathway 2) and proton loss. All energy values are quoted in kcal/mol.

3.2.1 Pathway 1 – loss of C_2H_2 from p-benzoquinone

The first step for loss of C_2H_2 from the ring involves cleavage of the C-C bond next to one of the C=O carbons. Formation of the transition state for C_2H_2 loss requires 30.0 kcal/mol and leads to an intermediate structure where the -C_2H_2 has swung around away from the ring allowing the C=O groups to approach and form the beginnings of a four-membered carbon ring. C_2H_2 loss is therefore concomitant with ring formation. This first step can be seen in the IRC profile below (Fig. 13). In the second step, the C_2H_2 is eliminated from the intermediate producing the cyclobut-3-ene-1,2-dione daughter fragment at m/z 82.

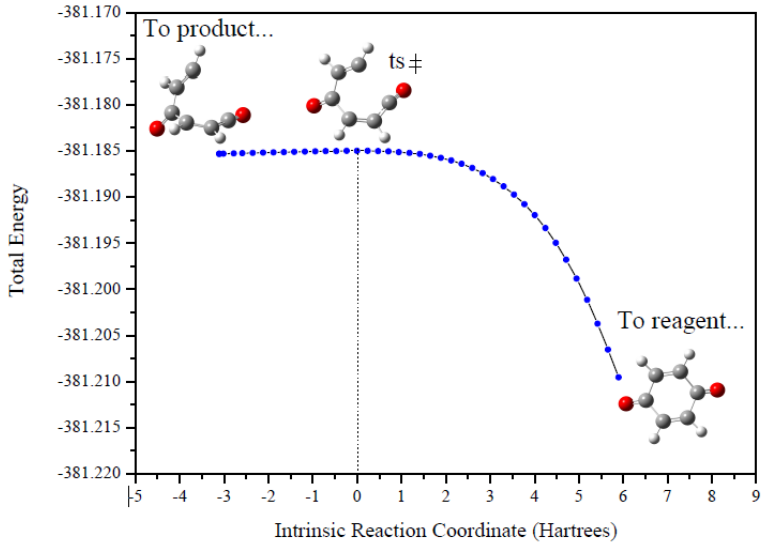

Fig. 13: IRC path for step 1 of the C_2H_2 loss fragmentation pathway for p-benzoquinone.

3.2.2 Pathway 2 – loss of CO from p-benzoquinone

The potential energy scan searches gave a transition state for the first step of CO loss where one of the CO groups is lifted-up away from the ring. As with C_2H_2 loss, removal of CO is concomitant with ring formation and as CO moves away, the ring to starts to contract into a 5-membered ring system (see IRC in Fig. 14). The transition state for this process requires 34.0 kcal/mol. By the time the intermediate has been reached, ring formation is now complete and CO is now attached to one of the ring carbons. During the second step, CO is completely eliminated to form the cyclopenta-2,4-dien-1-one at m/z 80. The transition state and intermediates structures are similar to in the energy profile for thermal decomposition of neutral p-benzoquinone studied by Roithová *et al.*

using DFT calculations with a similar procedure.[55] This suggest both neutral and ionized p-benzoquinone lose CO via a similar reaction pathway.

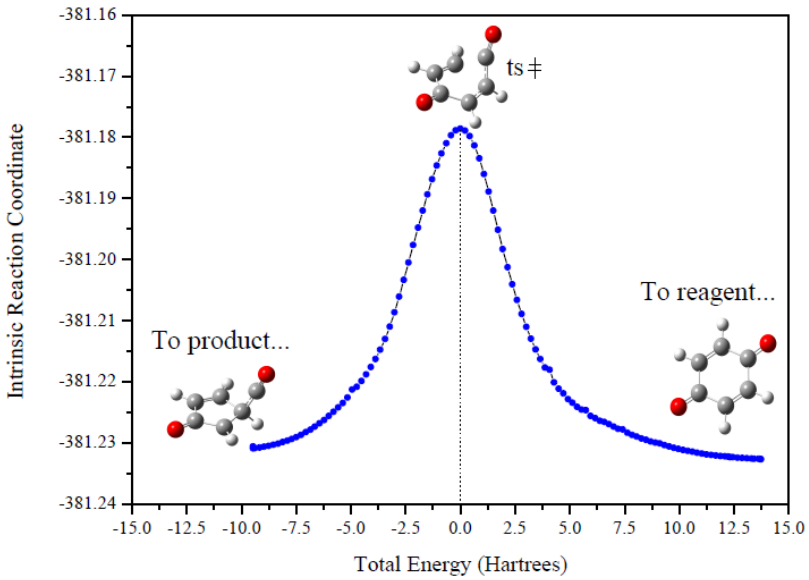

Fig. 14: IRC path for step 1 of the CO loss fragmentation pathway for p-benzoquinone.

3.2.3 Proton loss from p-benzoquinone

Removing one of the protons from the ring was a single step process and had a high energy barrier requiring 81.9 kcal/mol for transition state formation. More energy is required as removal of a proton causes significant disruption to the π-system by breaking the ring apart. The ring structure is not regained, creating little stabilisation in the product, as seen in the IRC (Fig. 15) where the path from the transition state leads onto a high energy product structure. There is no evidence that this structure is produced from fragmentation of p-benzoquinone in the gas phase or helium droplet mass spectrum.

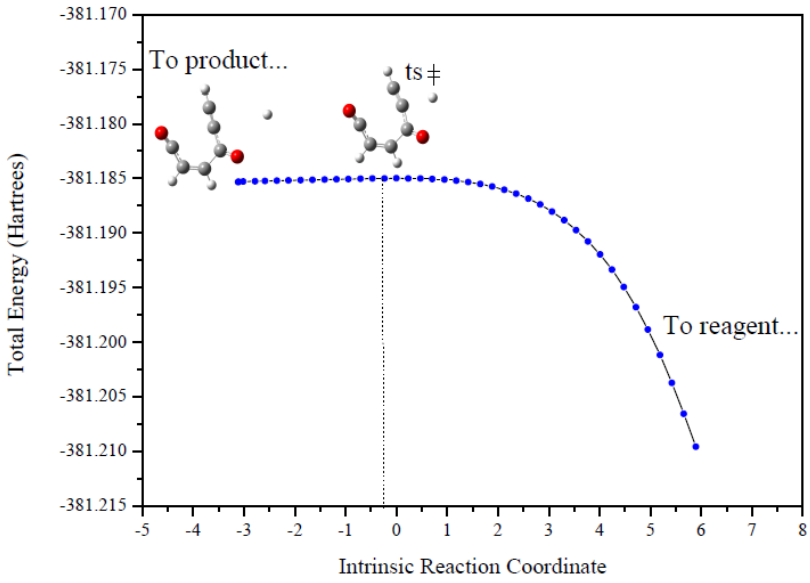

Fig. 15: IRC path for the proton loss fragmentation pathway for p-benzoquinone.

3.2.4 Discussion of results from DFT calculations

The results from the DFT calculations agree with the peak intensities in the mass spectra in Fig. 10. In both the gas phase and helium droplet mass spectra, the C_2H_2 daughter fragment peak at m/z 82 is more intense than the CO loss peak at m/z 80. This agrees with the calculated energy barrier for transition state formation. It requires more energy to form the transition state for CO loss vs. C_2H_2 loss. Hence, this reaction energy pathway is less favourable. The favourability for C_2H_2 is significantly stronger in the helium droplet mass spectrum. However, there is only a 4 kcal/mol energy difference between the activation energies. The ionization energy of p-benzoquinone was calculated to be 9.8 eV (close to the experimental of 10.1 eV[56]). Assuming the dopant is reached within two hops of the surface helium atom, it can be assumed an excess energy of approximately 5-6 eV (120 - 140 kcal/mol) is transferred to p-benzoquinone by resonant charge hopping.[40] Therefore, there is sufficient energy available to fragment either via pathway 1 or pathway 2. There must be another driving force to cause pathway 1 to be strongly favoured. It is likely the preference could also be due to cage effects. Although there is not much difference in the mass, the C_2H_2 neutral is lighter so could be ejected more easily. Alternatively, it has also been noted that the surrounding helium could make the formation of certain transition states easier.[44] A more important

regularity between the energy profiles in Fig. 12 and the mass spectra is the lack of a proton loss peak in both the helium droplet and gas phase electron ionization mass spectra. Loss of a proton from the ring requires over 2.5 times more energy than pathway 1 and pathway 2 to overcome the activation energy barrier for transition state formation. This makes the pathway so unfavourable it is not even observed in the gas phase mass spectrum where there is a wealth of excess energy delivered to the molecule. Hence, proton loss is very unlikely to occur in the helium droplet mass spectrum. This means C_2H_2 is the lightest fragment which can be lost from p-benzoquinone.

3.3 Overall theory to explain the p-benzoquinone mass spectrum

The DFT calculations have helped to understand how p-benzoquinone fragments upon electron ionization. The most favourable daughter fragments have been identified and agree with the intensities in the mass spectra. However, one thing which remains unclear is why the parent ion fragments extensively in the helium droplet mass spectrum, to the extent where most has been converted into the daughter fragments. As already discussed, this cannot be due to more energy being delivered to p-benzoquinone as the helium droplet quenches the initial ionisation energy. Another factor to consider is the constraints of the helium droplet. For alkali metals, the interaction between ions and solvating helium atoms is often referred to as a 'snowball' because the strong ion induced dipole between the positive alkali metal ion and helium atoms can cause the solvating helium to have a density comparable to that of solid helium.[57] If such a strong cage effect forms around the p-benzoquinone parent ion during the immediate stages after ionization, this will ultimately affect the fragmentation process. Although ionization produces a stable parent ion, for this parent ion to be ejected intact from the helium droplet it has to break through the cage of surrounding helium atoms. The energy barrier for this must be significant as instead the parent ion dissipates most of the excess energy by fragmentation. There is no proton loss fragmentation route as the DFT calculations show this is too unfavourable. The only other way p-benzoquinone can fragment is via loss of C_2H_2 or CO. Therefore, in the competition between ion ejection and fragmentation, fragmentation wins forcing p-benzoquinone to almost completely fragment into its daughter fragments as seen in the model in Fig. 16.

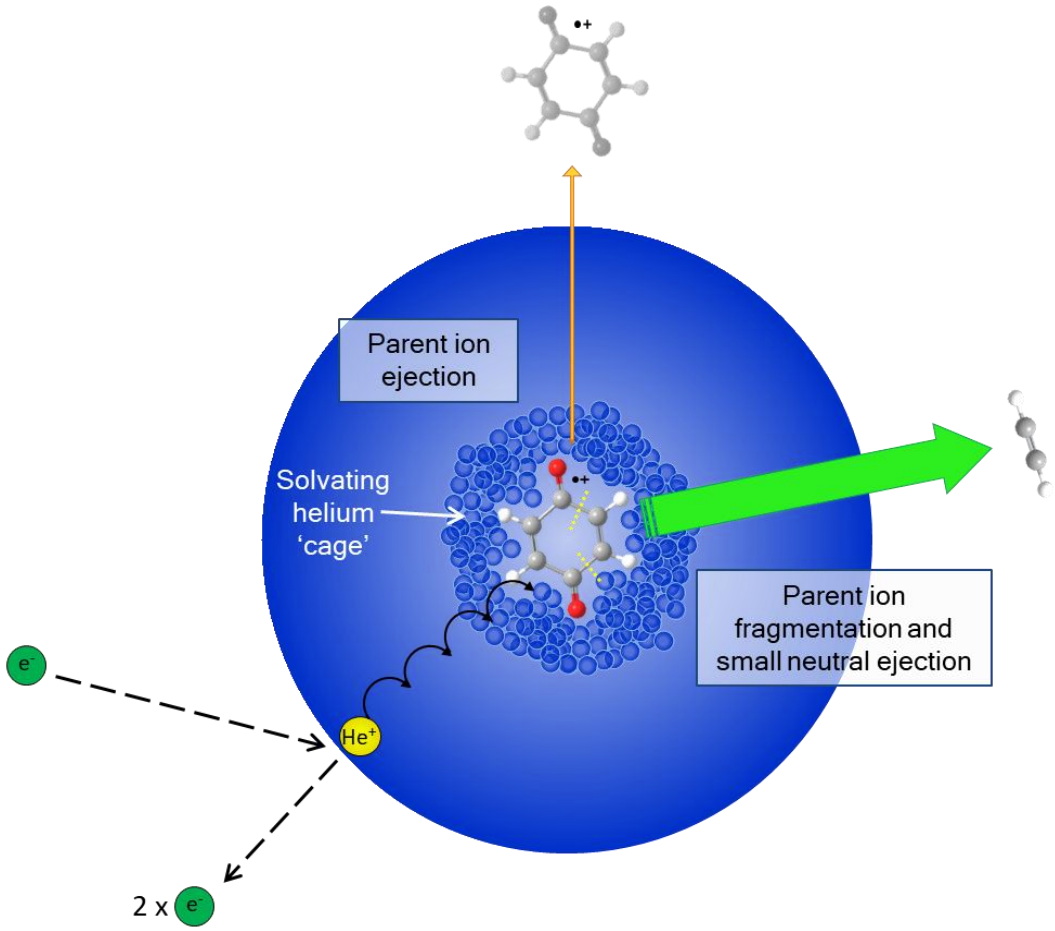

Fig. 16: Illustration of proposed model for helium droplet electron ionization of p-benzoquinone. This reflects the theory that the solvating cage of helium atoms around the parent ion creates a large energy barrier to parent ion ejection, forcing the parent ion to fragment and eject a small neutral instead. In this illustration, the neutral is C_2H_2.

It is important to note that there could be an alternative explanation to the theory above, but without further investigation this seems the most likely explanation. The behaviour observed in the helium droplet mass spectrum is interesting as it suggests the nature of the solvating helium atoms can have a stronger effect on the fragmentation process than previously thought. One thing which would be interesting to do is to model the ionization process using molecular dynamics. For example, modelling the ejection of the parent ion vs. CO or C_2H_2 from a droplet of a defined size could produce results which support the theory that there is a large energy barrier to parent ion ejection because of cage effects. Alternatively, it is important to consider that the solvation structure around the dopant could vary for different molecules. Therefore, this observation might be specific to p-benzoquinone. To support the theory, it would be interesting to see whether other conjugated and aromatic molecules have a similarly reduced parent ion signal. Such molecules are likely to have a similar fragmentation

process to p-benzoquinone in that they have a high energy proton loss pathway meaning they are forced to fragment by other routes to escape the droplet. To investigate this, molecules which could display the same behaviour were investigated using DFT calculations using the same method.

3.4 Investigating the fragmentation of other conjugated/aromatic molecules using DFT calculations

A selection of four suitable molecules were chosen including: phenol, 1,3-benzenediol, 1,4-dichlorobenzene and 1,4-dibromobenzene. All these molecules have high intensity parent ion peaks in their gas phase mass spectra (typical for aromatics) and there is no evidence of a proton loss peak. To account for the gas phase mass spectra, energy profiles for the initial step in the main fragmentation pathways have been calculated and compared against the energy profile for proton loss. Since the fragmentation patterns are similar for phenol and 1,3-benzenediol and for 1,4-dichlorobenzene and 1,4-dibromobenzene, the results will be discussed in pairs.

3.4.1 Phenol and 1,3-benzenediol

Both phenol and 1,3-benzenediol (resorcinol) initially fragment via tautomerisation followed by loss of CO. The combination of both processes results in overall ring contraction. This can be seen in the NIST mass spectra in Fig. 17 and Fig. 18, along with the proposed overall fragmentation mechanism. CO loss produces the daughter fragment at m/z 66 for phenol and m/z 82 for resorcinol. The neighbouring peaks in the spectra at m/z 65 and m/z 81, respectively, are produced by the loss of H from the daughter fragment produced by CO loss following tautomerisation. In 1,3-benzenediol there are two –OH groups so tautomerisation can occur between the two –OH groups or at the side of one –OH group. In addition, there a two potential sites for proton loss: from the ring or from one of the –OH groups. Therefore, DFT calculations have been performed for all tautomerisation + CO loss and proton loss routes. The dissociation energies calculated for removal of a proton from the *ortho*, *para* or *meta* sites on the carbon ring were almost identical (i.e. within a few kcal/mol) for both phenol and resorcinol. Similarly, the energy was the same for removal of a proton from either –OH group in resorcinol. Therefore, the value proton loss from each site is quoted as an average. Fig. 19 shows the DFT calculations for phenol and Fig. 20 shows the DFT calculations for resorcinol.

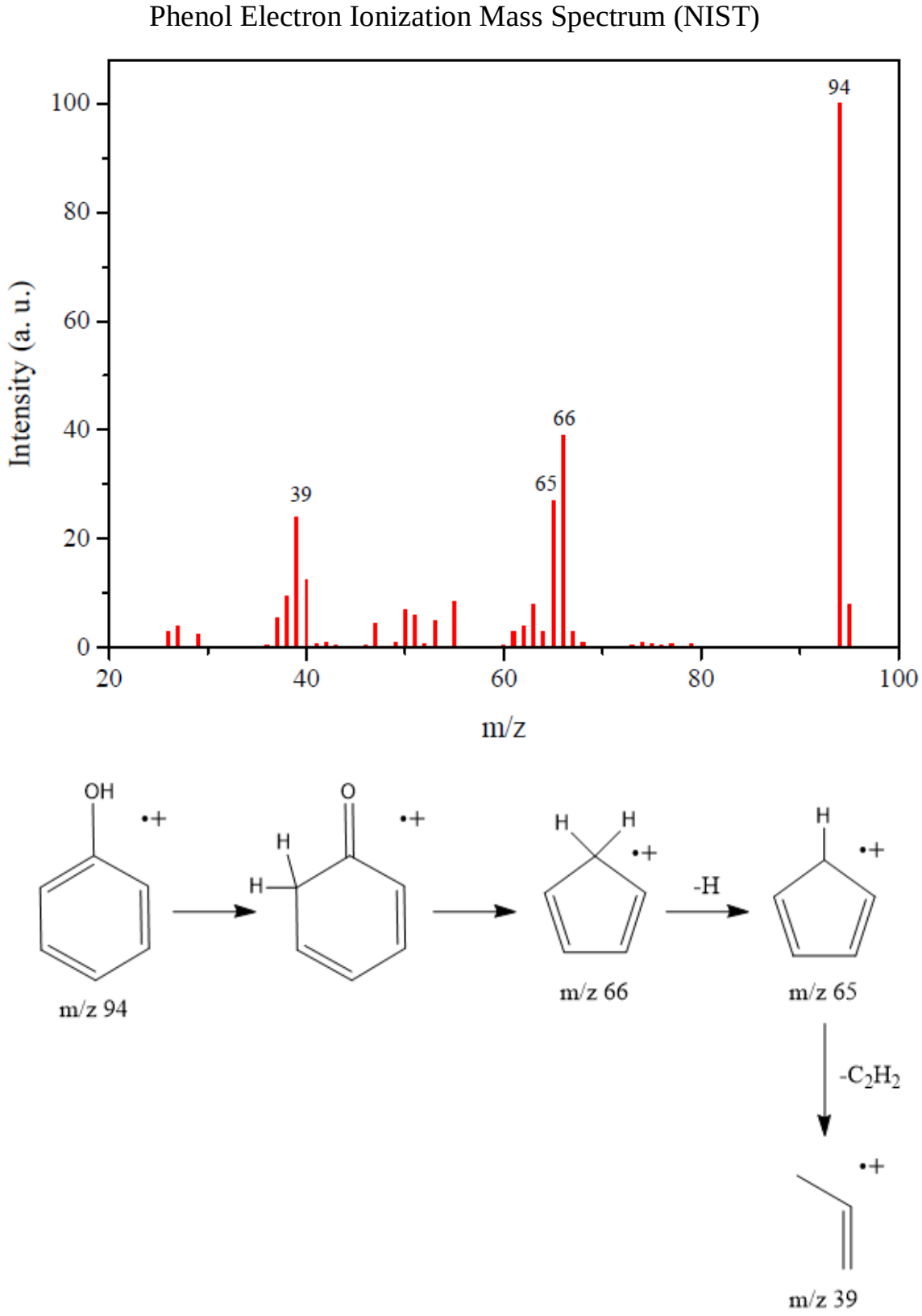

Fig. 17: The gas phase electron ionization mass spectrum of phenol taken from the NIST database. Below the spectrum, there is the suggested overall fragmentation mechanism interpreting the major peaks in the mass spectrum.

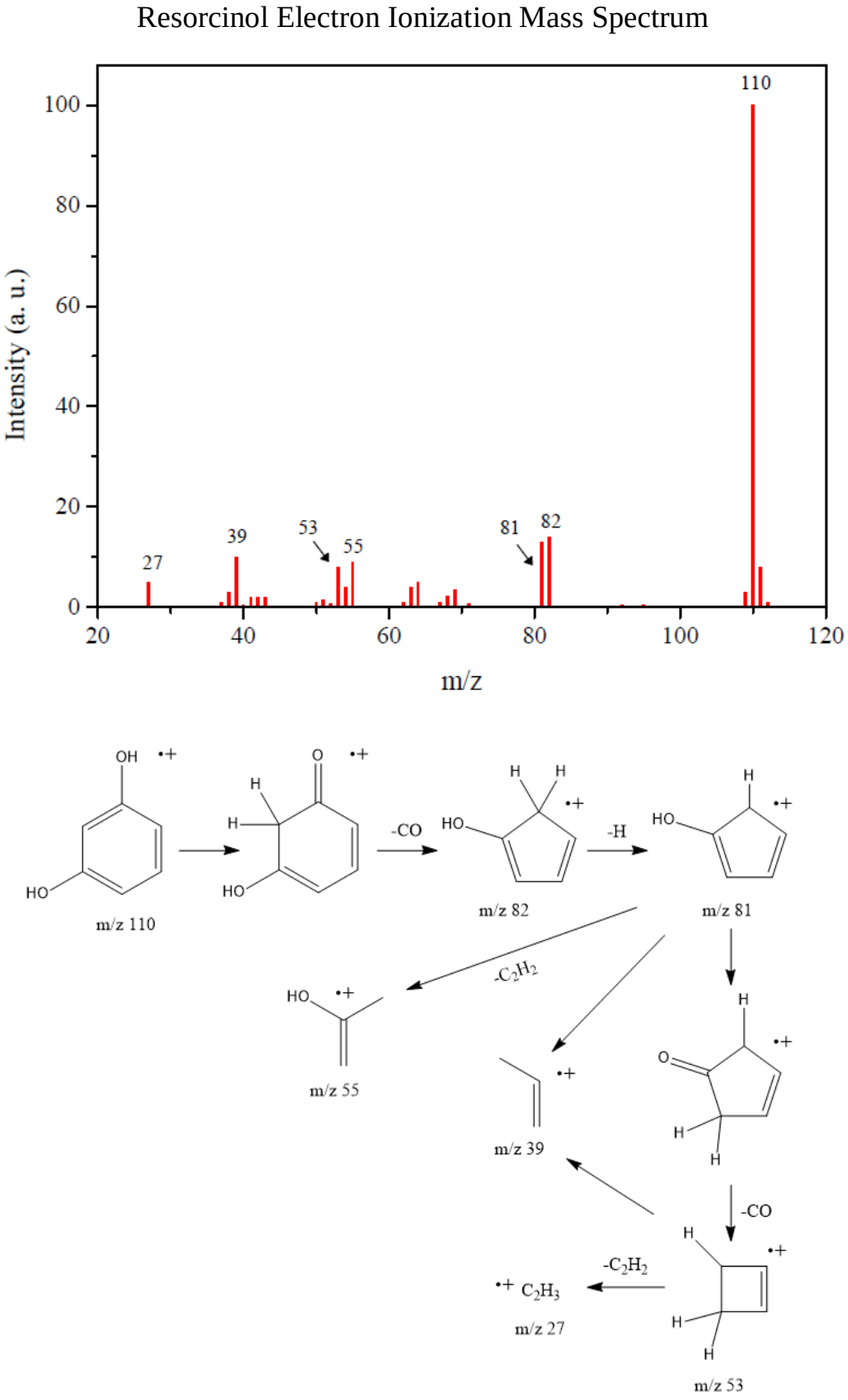

Fig. 18: The gas phase electron ionization mass spectrum of resorcinol taken from the NIST database. Below the spectrum, there is the suggested overall fragmentation mechanism interpreting the major peaks in the mass spectrum.

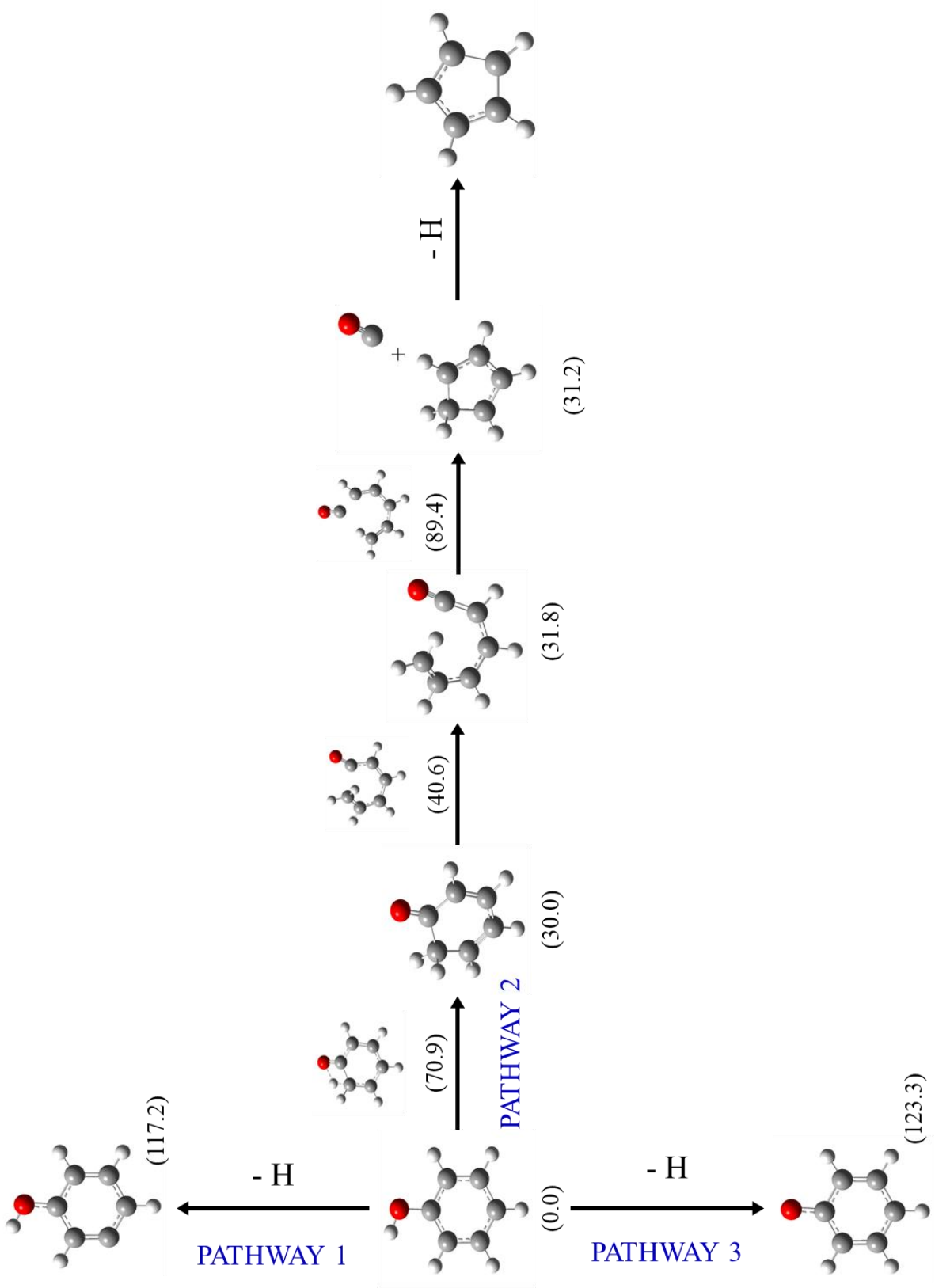

Fig. 19: Results from DFT calculations studying the initial fragmentation pathways of phenol upon electron ionisation. The pathways are as follows: proton loss from carbon ring (pathway 1); tautomerisation + CO (pathway 2); and proton loss from –OH group (pathway 3). All energy values are quoted in kcal/mol.

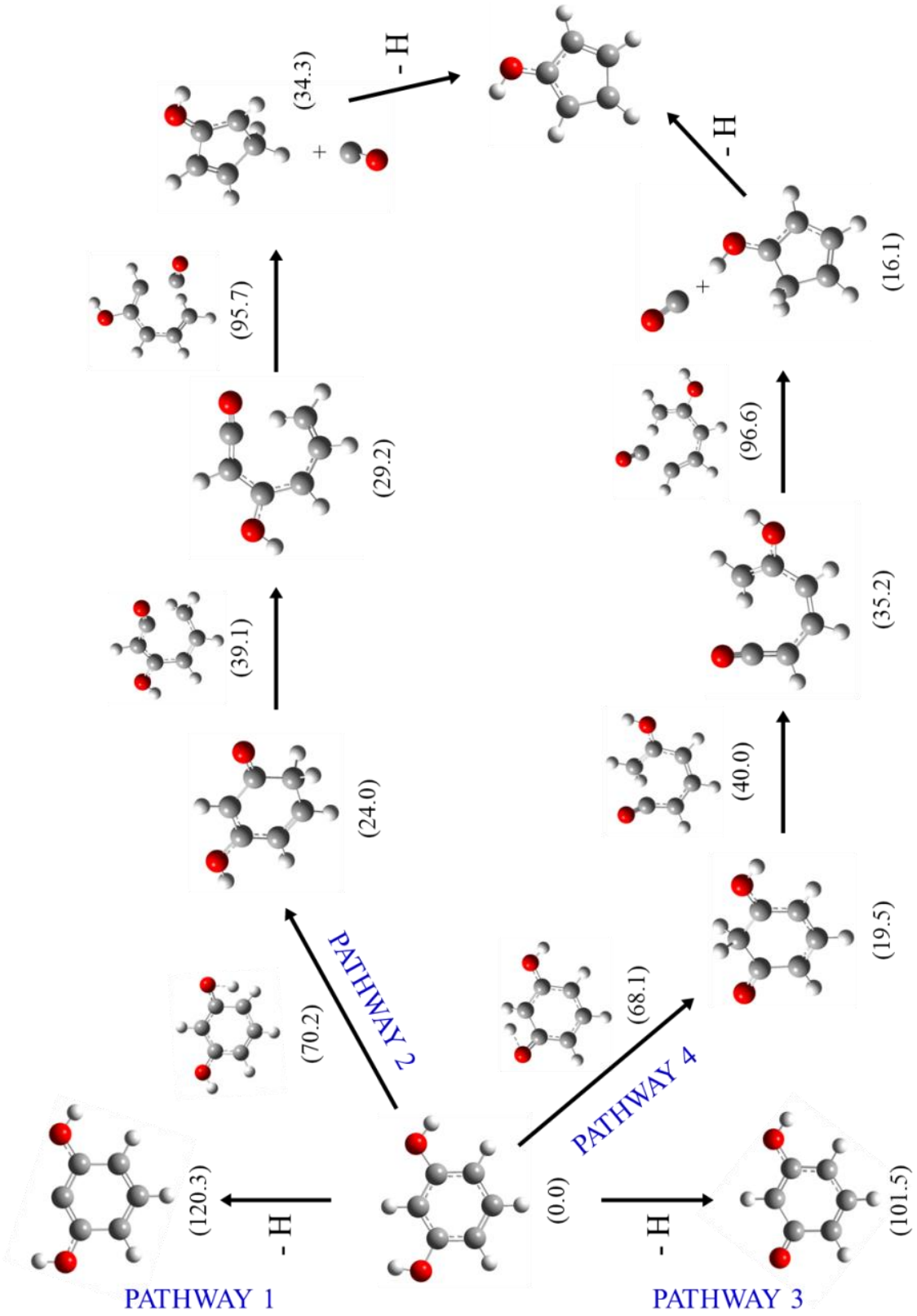

Fig. 20: Results from DFT calculations studying the initial fragmentation pathways of resorcinol upon electron ionisation. The pathways are as follows: proton loss from carbon ring (pathway 1); tautomerisation + CO loss at the side of one –OH group (pathway 2); proton loss from –OH group (pathway 3); and tautomerisation + CO loss from middle of –OH groups (pathway 4). All energy values are quoted in kcal/mol.

The energy profiles for phenol in Fig. 19 show there are three possible fragmentation pathways: pathway 1 - proton loss from the carbon ring, pathway 2 - tautomerisation + CO loss and pathway 3 - proton loss from the –OH group. It is instantly evident from the three pathways, that removal of a proton from either the –OH group or carbon ring requires a greater activation energy for the first step. The energy required to initiate tautomerisation is ~40% less than in the proton loss pathway. Almost the same results were observed in the resorcinol energy profiles in Fig. 20, but with the addition of another tautomerisation + CO loss pathway (pathway 4). There was very little difference between the initial activation energies for pathways 2 and 4 in Fig. 20 showing there is an almost equal preference for tautomerisation at either position. Again, comparing the activation energy for tautomerisation + CO loss showed proton loss required more energy (~30 to 40% more than proton loss). Therefore, the DFT calculations show that proton loss is not a favourable pathway for phenol or resorcinol. As seen with p-benzoquinone, proton loss requires more energy and produces an unstable product where the aromaticity of the benzene ring is disrupted. Although, -OH loss requires slightly less energy for resorcinol it is still not observed in the NIST mass spectrum. Hence, it is expected the lightest fragment which can be lost in the initial fragmentation step during helium droplet electron ionization should be CO.

3.4.2 1,4-Dichlorobenzene and 1,4-dibromobenzene

The fragmentation process for the 1,4-dichlorobenzene and 1,4-dibromobenzene parent ions is simple, involving loss of Cl or Br, respectively. Therefore, there were only two initial fragmentation pathways to consider: loss of a halogen vs. loss of a proton. The existence of multiple isotopes creates a cluster of two peaks representing halogen loss. These two peaks are identified in the NIST mass spectra in Fig. 21 and Fig. 22. DFT calculations were performed using four combinations the two most abundant isotopes for each halogen (as seen below) and are presented in Fig. 23.

(1) $^{35}Cl\text{-}C_6H_4\text{-}^{35}Cl$ (2) $^{35}Cl\text{-}C_6H_4\text{-}^{37}Cl$ (3) $^{37}Cl\text{-}C_6H_4\text{-}^{35}Cl$ (4) $^{37}Cl\text{-}C_6H_4\text{-}^{37}Cl$

(1) $^{79}Br\text{-}C_6H_4\text{-}^{79}Br$ (2) $^{79}Br\text{-}C_6H_4\text{-}^{81}Br$ (3) $^{81}Br\text{-}C_6H_4\text{-}^{79}Br$ (4) $^{81}Br\text{-}C_6H_4\text{-}^{81}Br$

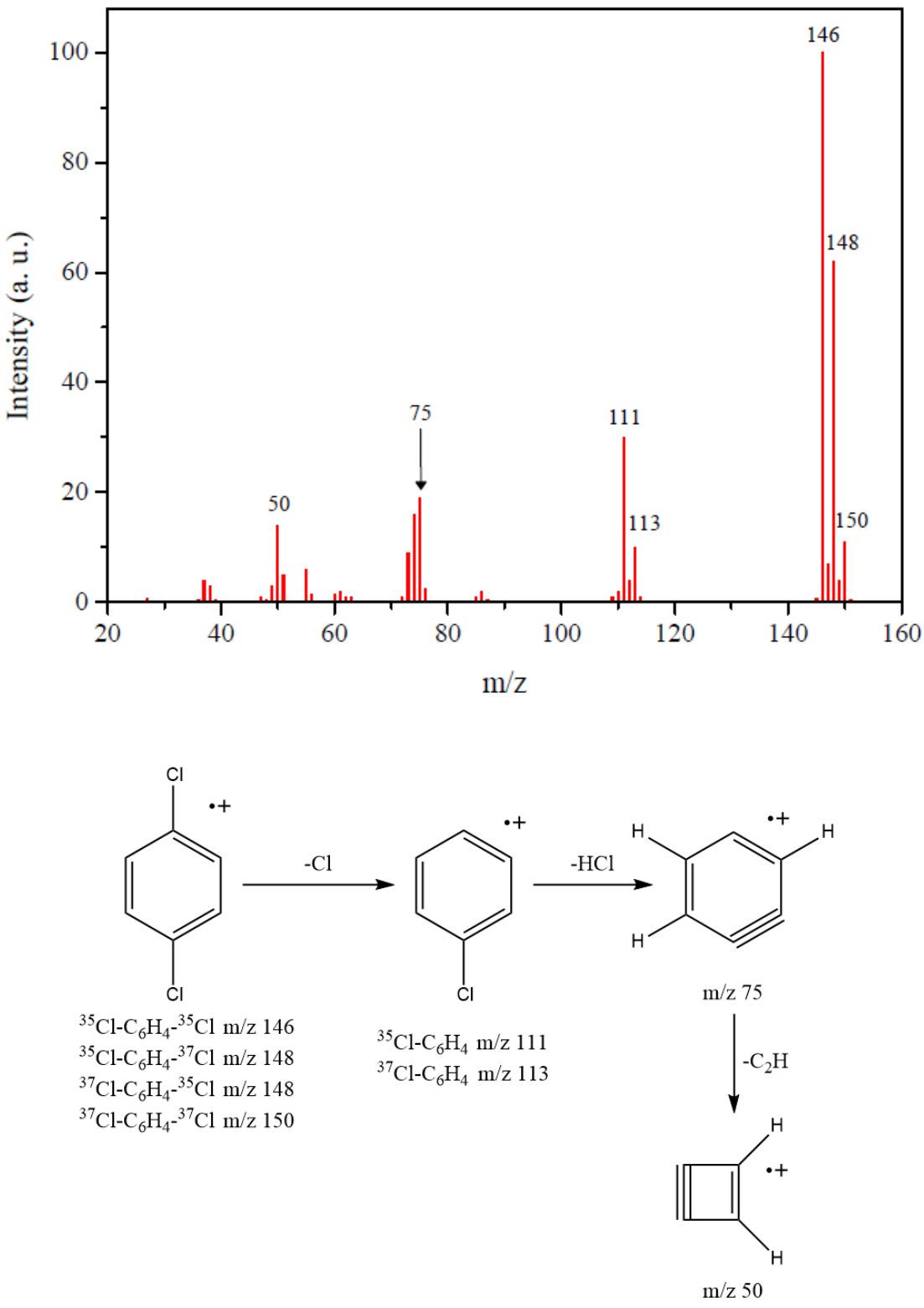

Fig. 21: The gas phase electron ionization mass spectrum of 1,4-dichlorobenzene taken from the NIST database. Below the spectrum, there is the suggested overall fragmentation mechanism interpreting the major peaks in the spectrum.

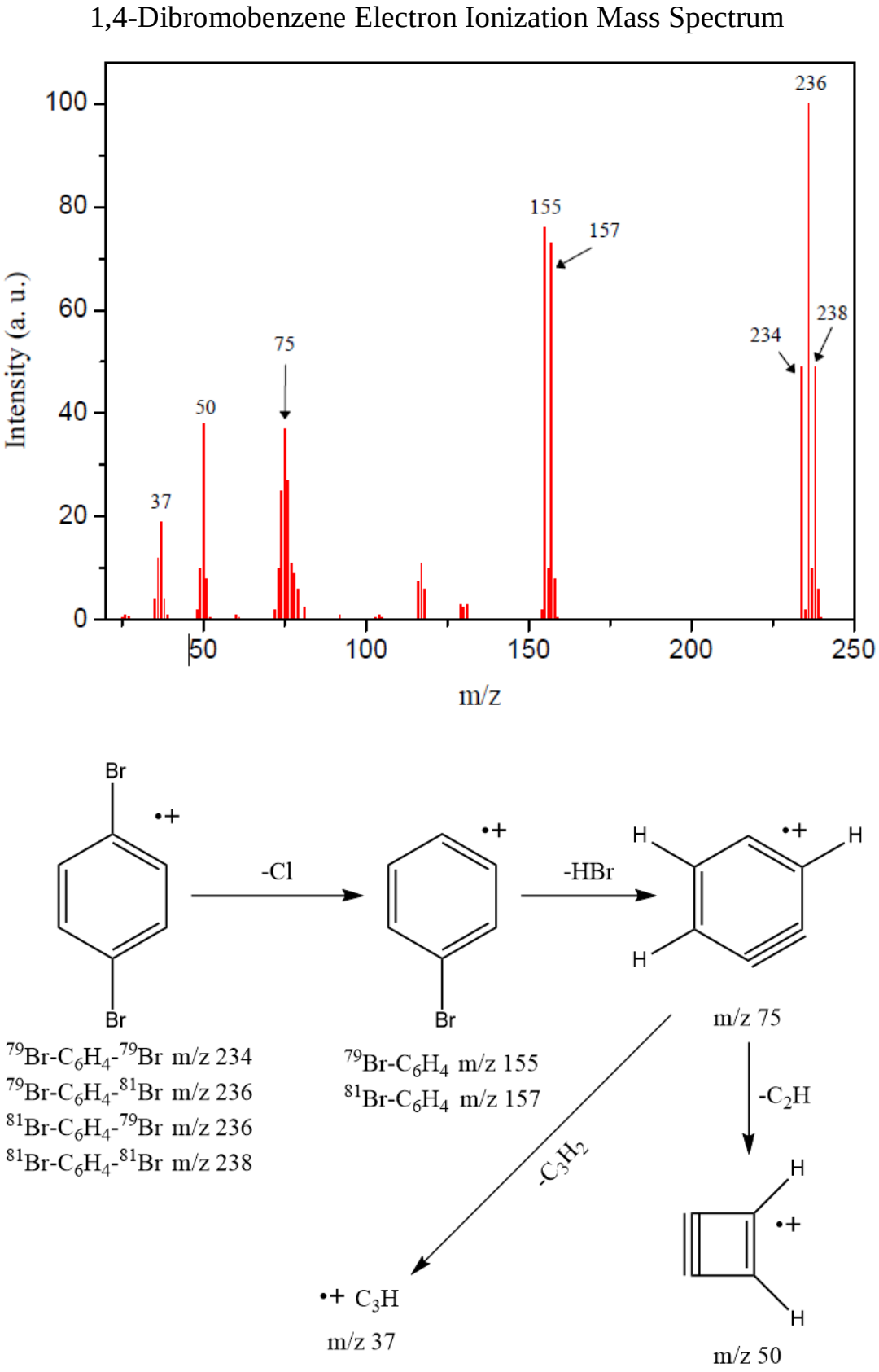

Fig. 22: The gas phase electron ionization mass spectrum of 1,4-dibromobenzene taken from the NIST database. Below the spectrum, there is the suggested overall fragmentation mechanism interpreting the major peaks in the spectrum.

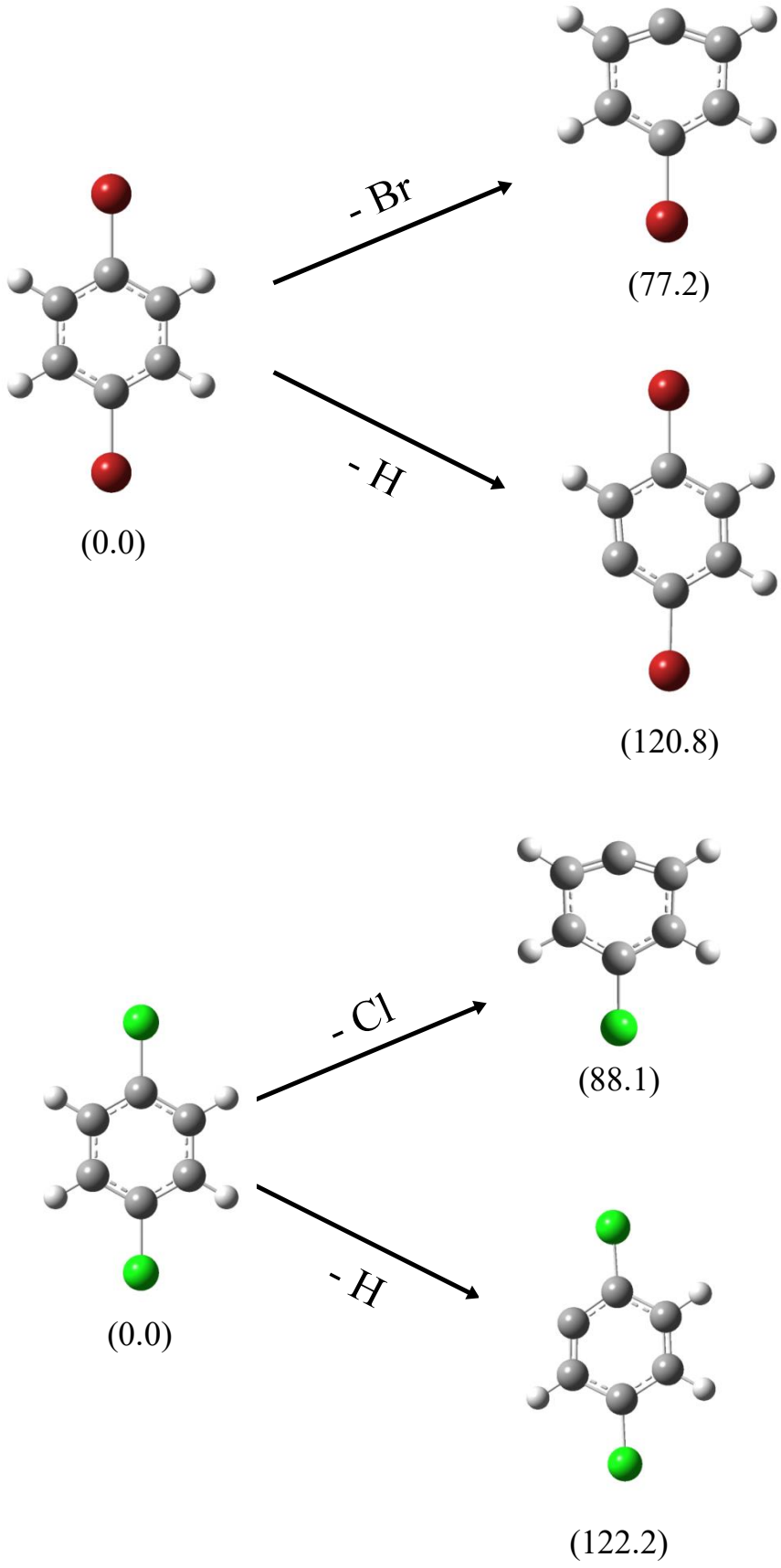

Fig. 23: Results from DFT calculations studying the fragmentation pathways of 1,4-dichlorobenzne (BOTTOM) and 1,4-dibromobenzne (TOP) upon electron ionisation. For both parent ions, there is a proton loss pathway and halogen atom loss pathway for initial fragmentation. All energy values are quoted in kcal/mol.

As expected from the lack of an M-1 peak in the NIST mass spectra, the energy required for proton loss is significantly greater than for halogen atom loss. The fragmentation energy was independent of isotope effects. Proton loss was found to be ~30 % greater for Cl loss and ~40 % greater for Br loss. Therefore, both molecules are unlikely to undergo proton loss in HeDs making them two additional candidate molecules for investigation in helium droplet electron ionization of aromatics.

4. Conclusions and future work

The helium droplet electron ionization mass spectrum of p-benzoquinone was recorded and shows a different behaviour to the previously recorded mass spectra of molecules in HeDs. The parent ion peak was significantly reduced, contradicting the theory of partial softening effects by indirect ionization and the fact that conjugated/aromatic systems typically show strong parent ion peaks. DFT calculations were used to study the energetics of the main fragmentation pathways and explained the lack of an M-1 peak in the mass spectra. Using the experimental data and theoretical calculations, a theory for this observation was developed. It is thought that the solvating 'cage' of helium atoms around the parent ion creates a significant energy barrier to ejection. Because of the cage, it becomes more energetically favourable for the parent ion to fragment and eject neutral C_2H_2/CO. The energy for proton loss from p-benzoquinone was calculated to be 2.5 times bigger than the energy for CO or C_2H_2 loss. The lightest neutral takes preference causing the p-benzoquinone parent ion to fragment and eject primarily C_2H_2 from the droplet in the initial fragmentation step. It is possible this theory could be tested using molecular dynamics to simulate the ionization process. However, prior to this it would be interesting to see if a similarly depleted parent ion signal is observed in the helium droplet mass spectra of other conjugated/aromatic systems. The DFT calculations on four candidate molecules have been performed and were shown to have a similar fragmentation process to p-benzoquinone in that proton loss is the least favourable initial pathway. If this prediction is correct, this work could help reveal more information about the influence the helium droplet matrix has on ions during the ionization process.

Chapter 2

Magnetic field assisted synthesis of iron oxide nanoparticles for biomedical applications

1. Introduction

1.1 An introduction to magnetic theory and magnetic nanoparticles

Magnetism is a physical phenomenon caused by the motion of electrons in atomic orbitals. There are various types of magnetic materials, whose properties are highly size dependent.[58] A vast number of magnetic materials, both bulk and nanoscale, are used in many everyday applications, such as data storage[59–61], catalysis[62,63], industrial and household appliances[64], energy technologies[65–67], biomedicine[68,69] and the environment[70,71].

1.1.1 Free atom magnetization

Starting from the atomic level, the magnetic moment of an atom is a result of the angular momentum of the electrons. The atomic angular momentum has both an orbital and spin contribution. The orbital moment arises from the motion of the electrons around the nucleus. The spin moment arises from the intrinsic spin of the electrons. The orbital (μ_L) and spin moments (μ_S) are given in equations 5 and 6:

$$\mu_L = -\frac{e}{2m_e}\boldsymbol{L} \quad \text{or} \quad \mu_L = \gamma_L \boldsymbol{L} \tag{5}$$

$$\mu_S = -\frac{e}{m_e}\boldsymbol{S} \tag{6}$$

Here, e is the charge, m_e is the mass of the electron, γ_L is the gyromagnetic ratio, $\boldsymbol{L}$ is the orbital annular momentum and $\boldsymbol{S}$ is the spin angular momentum. The absolute values of $\boldsymbol{L}$ and $\boldsymbol{S}$ are obtained from the total orbital and spin angular momentum quantum numbers, denoted as L and S, respectively.

$$|\boldsymbol{L}| = \sqrt{L(L+1)}\hbar \tag{7}$$

$$|\boldsymbol{S}| = \sqrt{S(S+1)}\hbar \tag{8}$$

L is calculated from the sum of the magnetic quantum number, m_l, and S is calculated from the sum of the spin angular momentum quantum number, m_s. In accordance with the Pauli Exclusion Principle, paired electrons are aligned anti-parallel, meaning only unpaired electrons contribute to S. The atomic spin and orbital angular momentum couple together to produce an overall atomic magnetic moment. This is known as spin-orbit coupling and the overall total angular momentum is given by $\boldsymbol{J}$ and is equivalent to the vector sum of $\boldsymbol{L}$ and $\boldsymbol{S}$.

$$|\boldsymbol{J}| = \sqrt{J(J+1)}\hbar \tag{9}$$

J is the total angular momentum quantum number and is the modulus of the sum of the orbital and spin momentum quantum numbers, L and S.

$$J = |L \mp S| \tag{10}$$

Therefore, the quantum numbers L, S, and consequently J, all depend on the values of m_l and m_s, both of which can take many different values for a multi-electron atom. Therefore, there are a standardised set of rules, known as Hund's Rules, that are used to work out L, S, and J. Hund's Rules are defined as follows:

(1) m_s must be maximised in accordance with the Pauli Exclusion Principle. This means the electron configuration which gives the highest S, and consequently the highest multiplicity (where the multiplicity equals $2S + 1$), is chosen.
(2) m_l must also be maximised to satisfy rule (1) and the Pauli Exclusion Principle.
(3) J is determined from L and S using the following rule: If the valence shells are less than half filled equation 10 becomes $J = |L - S|$. Conversely, if the valence shell are more than half filled equation 10 becomes $J = |L + S|$.

Using Hund's rules, the magnetic state of the atom/ion can be written in a shorthand notation called a term symbol.

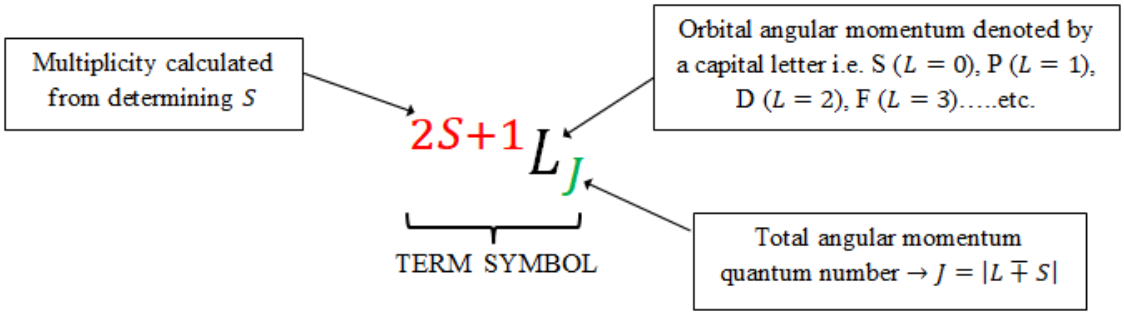

Because the coefficients for $\boldsymbol{L}$ and $\boldsymbol{S}$ are not equal, the total magnetic moment is not parallel to the total angular momentum ($\mu_{total} = \mu_L + \mu_S$). In fact, μ_{total} is forced to precess around $\boldsymbol{J}$ producing an effective total magnetic moment, μ_{eff}, given by:

$$\mu_{eff} = -g\frac{e}{2\,m_e}\boldsymbol{J} \tag{11}$$

where g is known as the Landé g-factor and is expressed as:

$$g = \frac{3}{2} + \frac{S(S+1) - L(L+1)}{2\,J(J+1)} \tag{12}$$

All the information describing spin-orbit coupling and the resulting magnetic moment is explained schematically in the diagram in Fig. 24.

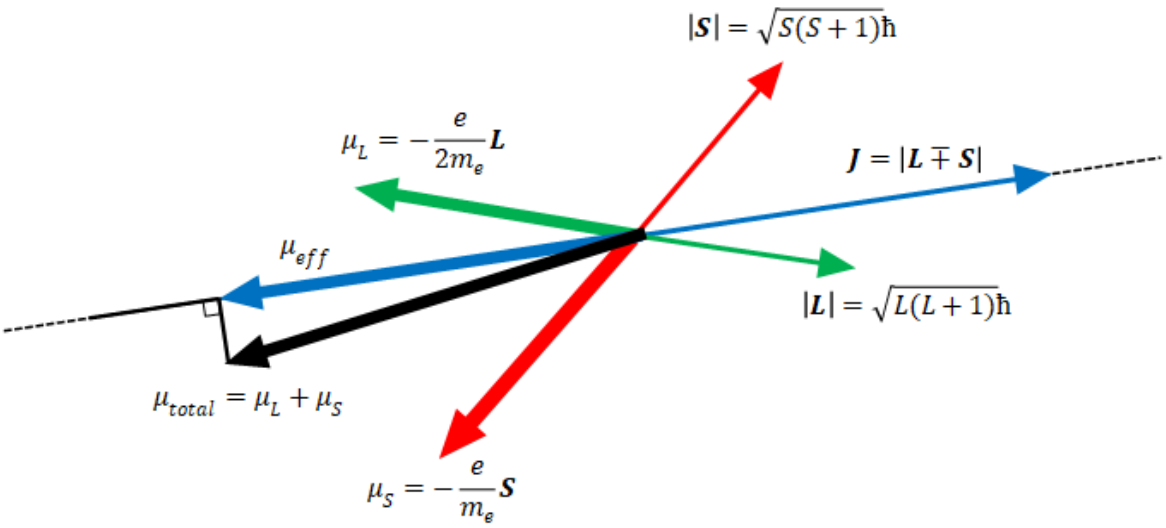

Fig. 24: Diagram showing the coupling of the spin and orbital angular momentum to give the total angular moment. The corresponding moments for each are shown, along with the effective magnetic moment. The total magnetic moment does not lie parallel to $\boldsymbol{J}$, but instead rotates around μ_{eff}.

The direction of μ_{eff} depends on $\boldsymbol{J}$. In no applied field, $\boldsymbol{J}$ points in any direction meaning to determine the atomic magnetic moment, the response to an external magnetic field must be measured. In an applied field, the magnetic energy is divided into $2J + 1$ energy levels from $+J_Z$ to $-J_Z$, assuming the magnetic field, $\boldsymbol{B}$, is applied along the *z*-axis of $\boldsymbol{J}$. The component of $\boldsymbol{J}$ along the *z*-axis is given by:

$$|\boldsymbol{J}_Z| = \hbar J \tag{13}$$

Therefore the maximum moment along the *z*-axis is given as:

$$|\boldsymbol{\mu}_Z| = g\, J\, \mu_B \tag{14}$$

where, μ_B is the Bohr magneton equal to:

$$\mu_B = \frac{e\,\hbar}{2\,m_e} \approx 9.27 \times 10^{-21}\ emu \tag{15}$$

Each energy level is aligned with $\boldsymbol{B}$ in a different direction. When all the atoms are in the lowest energy level, $-J_Z$, magnetic saturation is reached producing the maximum

magnetic moment in equation 14. When atoms are excited to higher magnetic energy levels, the measured magnetic moment along the *z*-axis is reduced. Excitation occurs as the temperature increases causing electrons to break Hund's Rules and be excited to higher magnetic energy levels. To achieve magnetic saturation, low temperatures and/or very high magnetic fields are needed to overcome thermal disturbance and keep all the atoms in the $-J_Z$ energy level. Macroscopically, this is effectively viewed as rotating μ_{eff} into the *z*-axis. At saturation, the net magnetization, *M*, is given by

$$M = N\boldsymbol{\mu}_Z \tag{15}$$

where N is the number of atoms.

For non-interacting atoms, the function which describes the external magnetic field and temperature dependence of the atomic magnetization is known as the Brillouin Function. The Brillouin Function can be used to re-express equation 15 as:

$$M = N\boldsymbol{\mu}_Z = Ng\,J\mu_B\left[\frac{2J+1}{2J}coth\left(\frac{2J+1}{2J}y\right) - \frac{1}{2J}\coth\left(\frac{y}{2J}\right)\right] \tag{16}$$

where, the Brillouin Function is:

$$B_J(y) = \left[\frac{2J+1}{2J}coth\left(\frac{2J+1}{2J}y\right) - \frac{1}{2J}\coth\left(\frac{y}{2J}\right)\right] \tag{17}$$

The temperature term is contained within y:

$$y = \frac{J\ g\ \mu_B\ B}{k_B\ T} \tag{18}$$

k_B is the Boltzmann constant and T is temperature. In no applied field, B equals zero, meaning $B_J(y)$ = 0 resulting no overall magnetization. In an applied field, the shape of the Brillouin function will depends on T, B and J.

Measuring atomic magnetization using the Brillouin Function requires magnetic saturation to be reached. This is not always easy, especially if very high fields are required for all atoms to reach the ground magnetic state. Alternatively, Curie's Law

can be used to determine the magnetic moment in low applied fields. At low fields, $\mu_B B \ll kT$. Hence, $y \ll 1$ meaning $\coth(y)$ can be approximated as:

$$coth(y) \cong \frac{1}{y} + \frac{y}{3} \tag{18}$$

Using this approximation, the Taylor series can then be applied to expand $coth\left(\frac{2J+1}{2J}y\right)$ and $coth\left(\frac{y}{2J}\right)$:

$$coth\left(\frac{2J+1}{2J}y\right) = \frac{2J}{(2J+1)y} + \frac{(2J+1)y}{6J} \tag{19}$$

$$coth\left(\frac{y}{2J}\right) = \frac{2J}{y} + \frac{y}{6J} \tag{20}$$

Substituting equations 19 and 20 into the Brillouin Function in equation 17 gives:

$$B_J(y) = \left[\frac{2J+1}{2J}\left(\frac{2J}{(2J+1)y} + \frac{(2J+1)y}{6J}\right) - \frac{1}{2J}\left(\frac{2J}{y} + \frac{y}{6J}\right)\right] \tag{21}$$

This simplifies to give the following magnetization expression:

$$M = \frac{N\,J(J+1)g^2\,{\mu_B}^2 B}{3k_B T} \tag{22}$$

Alternatively, the magnetization can be written in terms of p, the effective magneton number:

$$M = \frac{N\,p^2\,{\mu_B}^2 B}{3k_B\,T} \tag{23}$$

$$p = g\sqrt{J(J+1)} \tag{24}$$

1.1.2 Magnetism in many-atom systems

As indicated above, only atoms with unpaired electrons display magnetism. Hund's rules dictate that for multi-electron atoms where all the electrons are paired, both L and S equal zero. Therefore, they have no overall angular momentum ($J = 0$) and no overall magnetic moment. When speaking of magnetic materials, this typically refers to *3d* transition metals and *4f* rare earth elements as they have lots of unpaired electrons. Table 1 shows the electron configuration, the L, S and J quantum numbers, the theoretical effective magnetron number (calculated using equation 24) and the measured effective magnetron number, for a selection of transition metal and rare earth elements.

Table 1: Measured and calculated magneton numbers for a collection of rare earth and transition metal elements.

	Element	**Electron Configuration**	***S***	***L***	***J***	**State**	***p*** **(calculated)**	***p*** **(measured)**
Rare Earths	Nd^{+3}	$4f^{3}$	3/2	6	9/2	$^{4}I_{\frac{9}{2}}$	3.62	3.5
	Gd^{+3}	$4f^{7}$	7/2	0	7/2	$^{8}I_{\frac{7}{2}}$	7.94	8.0
	Tb^{+3}	$4f^{8}$	3	3	6	$^{7}I_{6}$	9.72	9.5
Transition Metals	Mn^{+4}	$3d^{3}$	3/2	3	3/2	$^{4}F_{\frac{3}{2}}$	0.77	4.0
	Fe^{+3}	$3d^{5}$	5/2	0	5/2	$^{6}S_{\frac{5}{2}}$	5.92	5.9
	Fe^{+2}	$3d^{6}$	2	2	4	$^{5}D_{4}$	6.7	5.4
	Co^{+2}	$3d^{7}$	3/2	3	9/2	$^{4}F_{\frac{9}{2}}$	6.54	4.8

Comparing the measured and calculated p values reveals important differences between the magnetic behaviour of rare earths and transition metal ions. Where p (calculated) and p (measured) are very similar for the rare earths, there is a large discrepancy

between the values for most of the transition metals, except for Fe^{+3} where the values agree well. This is because in rare earths magnetism arises from the 4*f* shell. The 4*f* shell lies close to the nucleus and has limited involvement in bonding. Hence, rare earths behave like 'isolated', non-interacting atom/ions. In transition metals, magnetism arises from the 3*d* shell which is a lot more involved in chemical bonding resulting in crystal field quenching. Crystal field quenching reduces the orbital contribution to the total magnetic moment. As a result, the measured atomic magnetization will always be lower than predicted for many-electron transition metal systems. Some 3*d* metals also experience quenching of the spin moment due to broadening of the energy levels into bands, further reducing the total atomic moment.

1.1.3 Types of magnetic materials

Following the discussion above, the main types of magnetic material can now be defined. These materials are:

- **Diamagnetic** - Material has atoms with completely paired electrons. As a result, there is no total angular momentum. However, because of Lenz's law, a weak opposing magnetic field is created in an applied magnetic field. Examples include: Au and Ag.
- **Paramagnetic** - Material possesses atoms with unpaired electrons, but magnetization is only achieved in an applied field. In no applied field, the atomic moments are randomised so there is no net magnetization. However, upon application of a magnetic field, the moments align with the *B* field and the material becomes magnetic. When the field is removed again, the magnetization decays as the moments randomise. Examples include: Mg, Al and Na.
- **Ferromagnetic** - Ferromagnetic materials have large numbers of unpaired electrons (e.g. transition metals). The exchange interaction causes atomic moments to align parallel even in the absence of a magnetic field so the magnetization is non-zero, irrespective of the presence of an applied field. The exchange interaction is purely quantum mechanical in nature and only acts between neighbouring atoms. The exchange energy between two neighbouring atoms with spins S_1 and S_2 is given by:

$$E_{ex} = -2\,J\,S_1.S_2 \tag{25}$$

Here, J is not the total angular momentum quantum number, but the exchange integral. J can be negative or positive. In ferromagnets, J is positive resulting in parallel alignment of spins. Typically, magnetization is divided up into magnetic domains in which anisotropy causes moments to point along certain crystallographic planes. This results in hysteresis when an external magnetic field is applied as more energy is required to break-up the domain structure and overcome the anisotropy energy barrier. Examples include: Fe, Ni and Co.

- **Anti-ferromagnetic** - The opposite of ferromagnetic. In these materials, the anti-ferromagnetic exchange interaction causes the magnetic moments to align anti-parallel and cancel each other out resulting in a net zero magnetic moment. This is a result of a negative exchange integral (J = –ve). Examples include: Cr, FeMn and NiO
- **Ferrimagnetic** - Has the same magnetic arrangement as an anti-ferromagnet. However, the magnitudes of the opposing magnetic moments are not equal producing a net magnetic moment. Examples include: iron oxides (e.g. Fe_3O_4) and yttrium iron garnets.

Fig. 25 depicts the behaviour of the magnetic moments for each of the above magnetic materials.

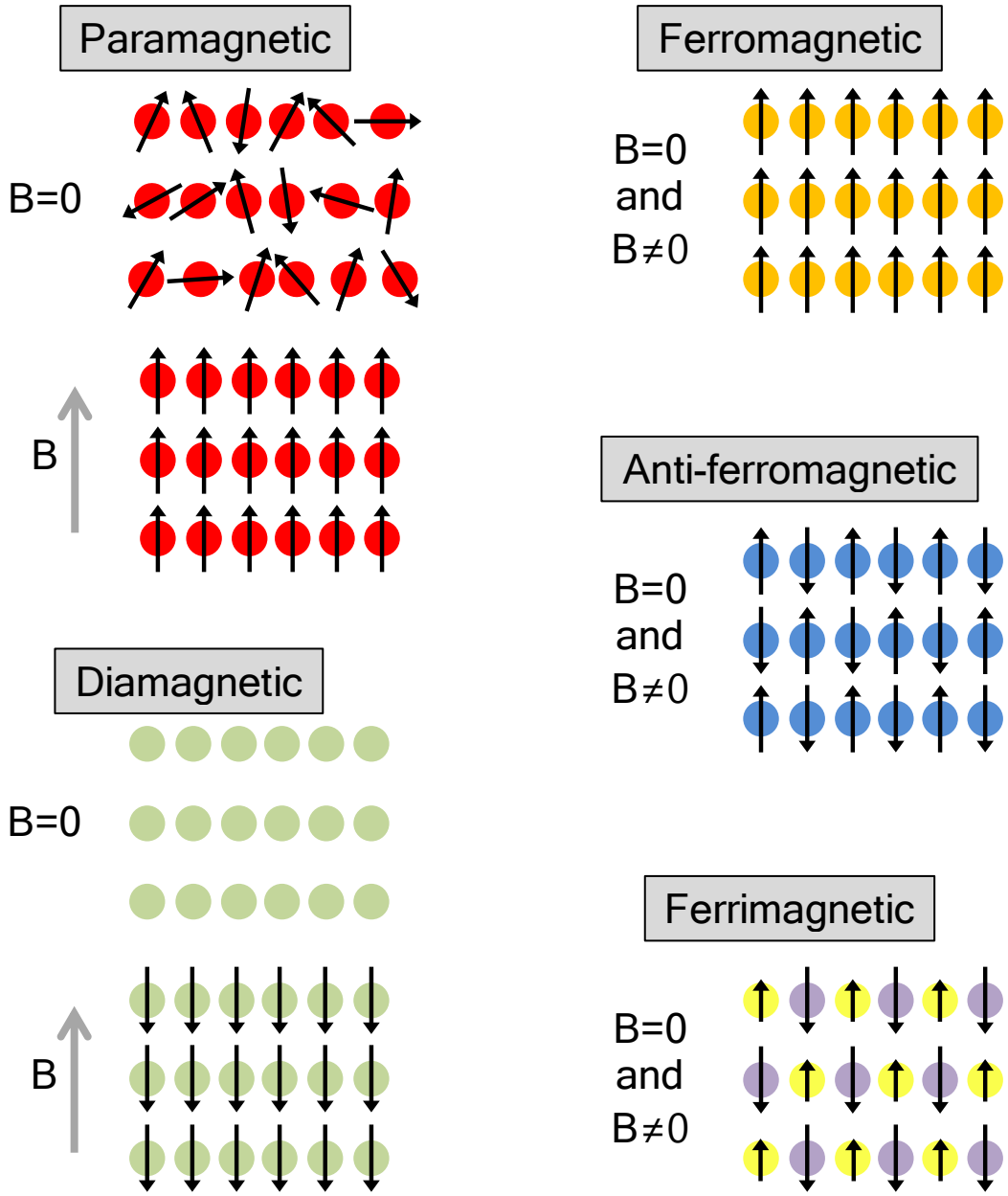

Fig. 25: Illustration of magnetic alignment in different types of magnetic materials.

1.1.4 Nanoscale magnetic materials – superparamagnetism

It has been well documented that nanoscale materials possess very different properties to the bulk because of the large number of under-coordinated surface atoms.[72–75] Under-coordination leads to a narrow energy band structure, and subsequently modifies the electronic, magnetic, optical and chemical properties, to the point where nanomaterials behave completely differently to their bulk counterparts. Certain nanoscale magnetic materials display an additional form of magnetism, known as superparamagnetism. The superparamagnetic state was first proposed by Frenkel and Doefman in 1930.[76]

Following a number of theoretical investigations, experimental evidence for superparamagnetism was first detected in the 1950s with nanoscale ferromagnetic and ferrimagnetic materials.[77–79] In bulk ferromagnets and ferrimagnets, magnetism is divided up into domains to reduce the magnetostatic energy. Magnetic domains are regions in which the magnetic moments are aligned (either parallel or anti-parallel (antiferromagnetic materials also show domain structure)) within the domain, but the direction of alignment between different domains is opposing. As the size of the material falls into the nano-regime, it eventually becomes energetically unfavourable to form domains because the cost of forming domain walls is not compensated by the reduction in the magnetostatic energy. Theoretically, the critical diameter for domain wall formation is ~25 nm, but the exact value varies depending on the material.[80] Particles below the critical diameter will be single domain and display superparamagnetism. In the absence of a magnetic field, the magnetic moments in a superparamagnetic material are randomly orientated. However, upon applying a magnetic field, the moments quickly align, aided by the exchange interaction, and become locked together to form a giant 'super-moment'. As a result, superparamagnetic materials can be viewed as behaving like paramagnets in no applied field, but because of the exchange interaction, are very strong ferromagnets in an applied field. As there are no domain walls, when the applied field is removed, the magnetization decays to zero with no hysteretic behaviour.

Fig. 26 compares the *M*-*H* curves and domain structure for a superparamagnet and ferromagnet. In the *M*-*H* curves, the *y*-axis is the measured magnetization (*M*) and the *x*-axis is the applied field (*H*). The *M*-*H* curve for ferromagnets shows the typical hysteresis curve observed. M_s is the saturation magnetization; M_R is the remnant magnetic field remaining after removal of the applied magnetic field; and M_c is the coercive field, which is the field strength require to return the magnetization to zero. The field can be applied in both directions producing saturation at 0° and 180° upon reversal of the field direction. The illustration below the curve shows the multi-domain structure of a ferromagnetic/ferrimagnetic particle. The curve for superparamagnetism displays the same magnetic saturation behaviour as the curve for ferromagnetism, but with no hysteresis i.e. $M_R = 0$ and $M_C = 0$. The diagram below the superparamagnetism *M*-*H* curve shows how the individual atomic moments cluster together to form a single domain particle with a 'giant' moment that can be described classically.

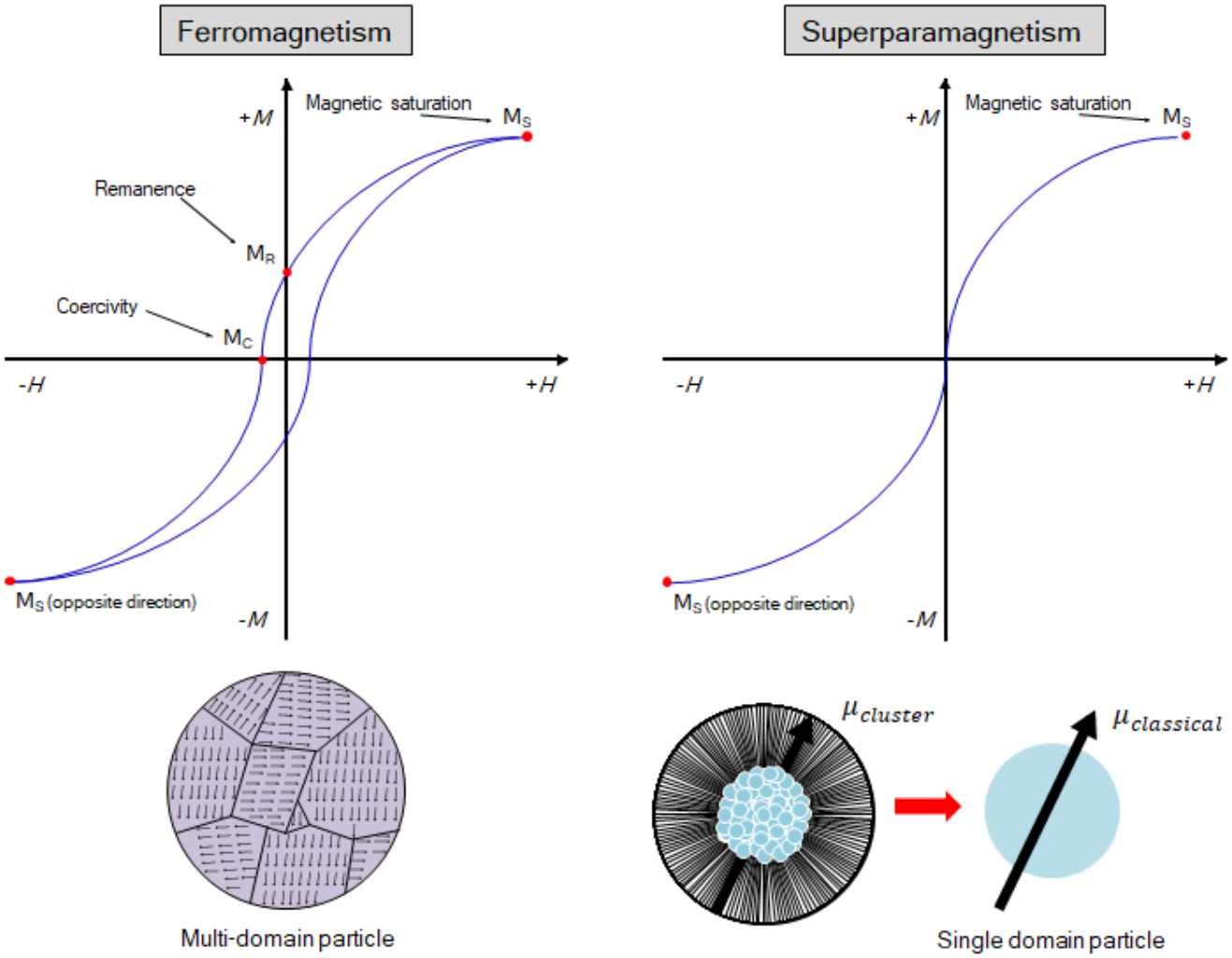

Fig. 26: Diagram illustrating the differences between the *M-H* curves for ferromagnets and superparamagnets. Below each *M-H* curve, there is an illustration of the domain structure of the magnetic material which is multi-domain for ferromagnets and single domain for superparamagnets.

Magnetization in superparamagnets is described using the Langevin function for paramagnetism. The Langevin function is the classical version of the Brillouin function. It is used to describe the overall magnetic moment of a collection of paramagnetic moments, instead of the moment of a single atom or ion. Superparamagnetic nanoparticles are essentially 'giant' paramagnets so can be described using the same equations. In the classical context, J can assume all values, thus the Brillouin function simplifies to:

$$L(x) = \coth(x) - \frac{1}{x} \tag{26}$$

In the Langevin Function, $x = \mu B / k_B T$ meaning the function has the same temperature and field dependence as in the Brillouin function. The magnetization expression therefore becomes:

$$M = N\mu \left[\coth\left(\frac{\mu B}{k_B T}\right) - \frac{k_B T}{\mu B}\right] = N\mu\, L(x) \tag{27}$$

When $B = 0$, $L(x) = 0$ so there is no net magnetization. However, then $B \to \infty$ or $T \to 0$, $L(x) \to \infty$ leading to a maximum magnetization of $M = N\mu$ i.e. the saturation magnetization. Saturation is achieved quickly for superparamagnets as the moments are highly responsive to the applied magnetic field. Therefore, for small x the Langevin function can be truncated after the first expansion in the Taylor series producing:

$$L(x) \approx \frac{x}{3} = \frac{\mu B}{3\, k_B T} \tag{28}$$

Substituting equation 28 into equation 27 gives:

$$M = \frac{N\mu^2 B}{3\, k_B T} \tag{29}$$

1.2 Introduction to superparamagnetic iron oxide nanoparticles and their applications

Because of their high magnetic susceptibility and on/off magnetization, superparamagnetic nanoparticles have achieved significant research interest in a number of areas. They have found applications in data storage[60,81,82], catalysis[83], batteries[84,85], magnetic separation[86], waste water treatment[70] and biomedicine[87–89]. Iron oxide (Fe_3O_4) is an example of a superparamagnetic material and displays room temperature superparamagnetism when the diameter falls below ~15 nm.[69] The biomedical applications of superparamagnetic iron oxide nanoparticles (SPION) have been extensively studied because they are biocompatible, biodegradable and non-toxic, making them well suited for various *in vivo* and *in vitro* applications.[90,91] For example, SPION are being used for both clinical treatment and research in areas such as disease detection[92,93], protein purification[86,94], disease treatment (magnetic hyperthermia

treatment[95–97], drug delivery[98–100], chemotherapy[101,102], magnetofection[103]), Magnetic Resonance Imaging (MRI)[104–106] and cell labelling/imaging[107–110]. Of these applications, SPION contrasts for MRI imaging and hyperthermia treatment have been particularly popular research topics.

1.2.1 Iron oxide nanoparticle contrasts for MRI imaging

A large proportion of the body is made of hydrogen and an MRI scanner generates images of organs and tissue by exciting hydrogen atoms aligned in a strong magnetic field using radio wave frequencies (RF). The excited hydrogen atoms resonate at a specific resonant frequency that depends on the local environment meaning the exciting RF must be varied to image different tissue regions.[111] When the RF signal is turned off, the resonating hydrogen atoms relax and emit an RF signal. The RF signal is detected and converted into an image. There are two modes of by which the hydrogens relax: (1) T_1 relaxation (spin-lattice relaxation) – time taken for the magnetization vector in the same direction as the applied field to return to its original state; and (2) T_2 relaxation (spin-spin relaxation) – time taken for the magnetization vector to stop precessing.[112] Positive contrast MRI images are generated from T_1 relaxation and negative contrast images are generated from T_2 relaxation. The relaxation time varies between tissue types creating contrast. Contrast can be increased by shortening the T_1 or T_2 relaxation time using a contrast agent that increases the relaxation rate of the surrounding hydrogen atoms.[113]

Contrast agents are used in a third of all MRI scans and are crucial to definitively identify tumours and lesions.[114] Chelated-gadolinium complexes have been used as paramagnetic positive (T_1) contrast agents since 1988, the first of which was gadopentetate dimeglumine (Magnevist®).[115] Gadolinium contrast agents are still widely used, yet they have a complex clinical history.[116] To perform an MRI scan, the contrast agent is injected some time prior to the measurement. The MRI scan is performed shortly after injection. The contrast remains in the body long enough to perform the scan, after which it should be excreted, primarily via the kidneys, within 24 hours.[117,118] In 2006, Grobner published findings which suggested a link between gadolinium contrast agents and nephrogenic systemic fibrosis (NSF) in patients with renal failure.[119] NSF is a potentially life-threatening disease involving tissue fibrosis (thickening) of the skin, and in some cases the internal organs[120] Subsequent

investigations established the link by revealing additional cases of NSF in renal failure patients.[121] These were mainly a result of gadodiamide (Omniscan®) injections and were attributed to dissociation of the gadolinium contrast agent.[121,122] In its chelated form, the contrast agent is non-toxic and is intended to be non-biodegradable whilst in the body to prevent release of the toxic Gd^{+3} ion. However, in patients with poor renal function, prolonged retention of the contrast agent led to dissociation in the kidneys releasing Gd^{+3}. As a result, administration of gadolinium contrasts was stopped for renal failure patients and there have been no new cases of NSF since 2009.[123]

Gadolinium contrast agents were still considered safe for patients without renal problems. That was until 2015 when Japanese researchers published evidence for gadolinium deposition in the brains of patients with normal renal function.[124] This second incident has made the use of gadolinium contrast agents an increasing concern, especially for patients who have undergone repeated contrast enhanced MRI scans.[125] In response to these findings, research has focused on replacing gadolinium with SPION because of their biocompatibility and larger magnetic moments, allowing the same high contrast to be achieved, but with lower doses.[126] Both ultra-small superparamagnetic iron oxide nanoparticles (USPION - diameter < 50 nm) and superparamagnetic iron oxide nanoparticles (SPION - diameter >50 nm) have been used as T_1, T_2 or dual (T_1/T_2) contrast agents, with numerous examples on the market.[113,117,127,128] Large SPION nanoparticles are typically used as generic contrasts and target all cells, whereas the few USPION that have reached the clinical market, have been developed to target specific organs, specifically the liver and lymph nodes.[91] Note, the diameters defined for SPION and USPION nanoparticles includes the iron oxide nanoparticle and the various functionalising groups encasing the nanoparticle.

Functionalisation of the SPION/USPION is an important step as this further improves the biocompatibility and ensures the nanoparticles are soluble in water. Various inorganic (silica, gold and carbon)[128–131] and organic coatings (water soluble polymers e.g. (poly(ethylene glycol), poly(acrylic acid), dextran and poly(D, L-lactide)[132–137] and biomolecules (liposomes, proteins and peptides)[138–140]) can be attached to the nanoparticle surface. This process is called functionalisation and it helps to stabilise SPION/SPION nanoparticles and prevent aggregation inside the body. The coating around the magnetic core has a large influence on the interaction with cells and even small changes in the coating can drastically affect the cell response.[141,142] Extensive

toxicity studies have to be performed on the nanoparticles to prove they are safe. The whole life cycle of the contrast agent should be analysed, from injection, contrast performance and cell interaction in the body, and finally to excretion. In addition to just making the magnetic contrast biocompatible, the surface groups can further be modified with antibodies which selectively bind to specific biomarkers the body, for example cancer markers.[143–145] This has been demonstrated by multiple groups as an effective way to concentrate the contrast agent and improve the image quality in the area of interest. Alternatively, this concept can be approached from an alternative angle. To concentrate the antibody labelled SPION at the target site, many antibody-target interactions are required. Instead, multiple iron oxide nanoparticles can be encapsulated inside a large liposome. The liposome surface contains a single antibody allowing many SPION to be delivered to the tumour with a single antibody-target binding interaction.[127,146] Because the liposome is so large, it can also act as a drug delivery vehicle by embedding drug molecules in the structure. He *et al.* have used this approach to develop a tumour-targeting SPION-lipids loaded with an anticancer drug. The anticancer drug successful inhibited the growth of breast cancer cells.[147] Moreover, the effect of the anti-cancer drug on the tumour could be monitored *in situ* using temporal ultra-sensitive MRI imaging after injection into tumour bearing mice. Therefore, the multi-functionalised liposome can selectively bind, image and treat the tumour, as well as monitor the effectiveness of the treatment. Instead of using anti-bodies, magnetic fields can also be used to concentrate the SPION-liposome delivery vehicles in the area of interest.[148] This technique is known as magnetofection. Delivery vehicles such as this are a part of a new field called theranostics as they allow both therapy and diagnosis of disease. Theranostics is gaining increasing interest across biomedicine.[149]

1.2.2 Iron oxide nanoparticles for magnetic hyperthermia treatment

Magnetic hyperthermia treatment is a cancer treatment which involves selectively heating the tumour to kill the cancerous cells. A colloidal solution (called a ferrofluid) is injected into the patient. Using magnetic fields, the iron oxide nanoparticles are concentrated at the tumour site. An oscillating external alternating magnetic field is then applied causing the nanoparticles to release energy in the form of heat. This raises the temperature of the cells above physiological temperature to between 41 to 47 °C, leading to cell death depending on the exposure time and where the temperature falls in this range.[150,151] Heat loss occurs via two mechanisms: (1) from Néel relaxation of the

moments within the nanoparticles and (2) Brownian motion of the particle.[152] All magnetic materials exhibit magnetic anisotropy, meaning the magnetic moments preferentially align across certain crystallographic axes known as the 'easy' axes. This is known as magnetocrystalline anisotropy, and is amongst one of the various types of magnetic anisotropy exhibited by magnetic materials. Other anisotropies include shape anisotropy, size anisotropy, surface anisotropy and exchange anisotropy. Superparamagnetic nanoparticles exhibit uniaxial anisotropy meaning there is one preferential 'easy' axis along which the moments point. The illustration in Fig. 27 shows that the uniaxial anisotropy energy is given by:

$$E_{uniaxial} = KV\ sin^2\theta \tag{30}$$

This equation represents how the anisotropy energy changes as the angle between the easy axis and direction of the cluster moment increases from 0° to 180°. The anisotropy energy is highest at 90°. For the magnetic moment to flip from 0° to 180°, the anisotropy energy barrier ($\Delta E = KV$) must be overcome. The time between flips is known as the Néel relaxation time, τ_N:

$$\tau_N = \tau_0\ exp\left(\frac{KV}{k_B T}\right) \tag{31}$$

τ_0 is the natural lifetime or value of the Néel relaxation time at the high temperature limit. If $KV \ll k_B T$, there is sufficient energy for the moment to overcome the anisotropy energy barrier and the moment will randomly flip between both directions along the easy axis. As it does, energy is released to the lattice in the form of phonons and magnons, before ordinary heat transport transfers the energy to the surrounding fluid. This heat loss mechanism is known as Néel relaxation. The other mechanism by which heat can be lost is Brownian relaxation. Brownian motion is the random motion of the particle in the solution. This leads to heat losses as the particle interacts with the surrounding ferrofluid and the overall moment tries to reorient itself with respect to the alternating magnetic field direction. Because the intracellular medium is more viscous than water, heat loss is believed to primarily occur via Néel relaxation.[153]

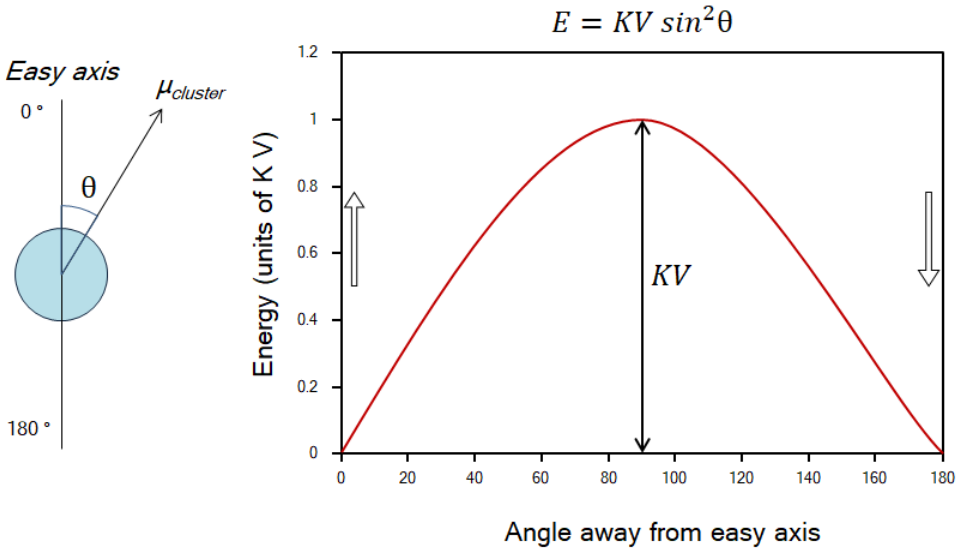

Fig. 27: Dependence of anisotropy energy on the magnetization direction along the easy axis for a nanoparticle with uniaxial anisotropy.

The heating efficiency of the tissue is measured using the specific absorption rate (SAR) and can be calculated for different nanoparticles:

$$SAR = \frac{C}{m}\frac{\Delta T}{\Delta t} \tag{32}$$

C is the specific heat capacity of the material, m is the amount of magnetic material per mass or per volume, and $\frac{\Delta T}{\Delta t}$ is the gradient of the temperature-time heating curve. The higher the value of the SAR, the better the hyperthermia performance. SAR values depend on a number of factors including: the intrinsic structure of the material, the magnetic saturation, magnetic anisotropy, size, shape, size distribution, functionalising groups and coatings, and the frequency and magnitude of the applied magnetic field. By studying the effect of these factors on the SAR value, researchers have discovered a multitude of ways to improve magnetic hyperthermia treatment. However, which method produces the 'best' nanoparticles is largely debated. For example, it has been found that the best SAR values are obtained with very monodisperse samples. This was predicted in early calculations by Rosensweig who found increasing the size distribution of the Fe_3O_4 ferrofluid, greatly degraded the heating performance.[154,155] The size of the nanoparticle itself has a dramatic influence on the SAR value as a consequence of the highly size dependent properties of nanoparticles.[58] Calculations by Habib *et al.*

indicated that the optimum size for monodisperse Fe_3O_4 nanoparticles was 19 nm.[156] Experimental findings indicate the highest SAR values are obtained for slightly larger sizes, for example, both Gonzalez-Fernandez *et al.* and Nemati *et al.* found higher SAR values for nanoparticles between 30-50 nm.[157,158] However, other studies confirm the predictions of Habib *et al.*, and some even suggest nanoparticles smaller than 19 nm exhibit the best SAR values.[155,159] This represents one of the main problems in nanoscience: results can vary between different papers depending on the synthetic procedure. Since the SAR depends on a number of factors, many of which are influenced by the synthesis method, changes in the conditions can strongly affect the results. It is the difficulty achieving reproducible results that makes legislation of nanoparticles for biomedical uses difficult without analysis on a case-by-case basis.

The shape of the nanoparticles has a large effect on the hyperthermia performance because this changes the magnetic anisotropy. For example, Martinez-Boubeta *et al.* have demonstrated the higher surface magnetic anisotropy of cubic Fe_3O_4 compared to spherical nanoparticles, produces a superior SAR for all nanoparticle sizes, with the greatest enhancement being seen for 20 nm cuboids.[160] The introduction of core-shell architectures can have an even more dramatic effect on heat losses. Noh *et al.* synthesised cubic $Zn_{0.4}Fe_{2.6}O_4$/ $CoFe_3O_4$ core-shell nanoparticles and compared the hyperthermia performance to single, spherical Fe_3O_4 nanoparticles.[161] The SAR was enhanced by 14 times as a result of exchange coupling between the magnetically soft core and hard shell.[162] Moreover, the advantage of core-shell nanoparticles is their properties can be very easily manipulated by changing the thickness of the shell layer. As well as doped Fe_3O_4 core-shell nanoparticles, pure shell Fe_3O_4/Au core-shell nanoparticles have been investigated and display similarly large SAR values.[163] Although, not all coatings have a positive effect on the magnetic properties and can passivate the surface layer of the nanoparticles by producing a magnetically 'dead' surface layer. This has been observed for SiO_2 coatings, as well as with polymers such as polyethylene glycol.[164,165]

A high SAR value is preferable; but it is important to recognise that the aim is not to achieve higher and higher temperatures. This could damage healthy tissues around the tumour and reduce the selectivity of the treatment. Instead, a concept known as 'smart therapy' can be employed. The basis behind smart therapy is the properties of the nanoparticles are designed to provide controlled treatment.[166] Similarly to adding

additional elements to Fe_3O_4 to make core-shell layers, 'smart hyperthermia' treatments can be made by doping the nanoparticles with transition metal elements. Doping has been used previously by Jang *et al.* to increase the M_S value of $(Zn_xMn_{1-x})Fe_2O_4$ nanoparticles to 175 emu g^{-1} (pure Fe_3O_4 saturates at ~98 emu g^{-1}).[167,168] Here, the intention was to increase M_s so the SAR increased meaning a lower dose of nanoparticles was required. However, the ratio of the dopant atom can also be selected so the Curie temperature, T_C, is only slightly above the therapeutic temperature for cell death. The Curie temperature is the temperature above which spins randomise because the thermal energy is greater than the interaction between the atomic moments. Therefore, the temperature will increase until T_C is reached when there is no more heat loss as the alternating magnetic field no longer affects the nanoparticles. Various 'smart' hyperthermia treatments have been suggested including $M_{1-x}Zn_xFe_2O_4$ (where M = Ni, Cu, Co or Mn), $ZnGd_xFe_{2-x}O4$, $Mn_{1+x}Ti_xFe_2O_4$ and $Mg_{1+x}Fe_{2-2x}Ti_xO_4$.[169–171] Temperature regulation is also attractive when developing combined treatments for example magnetic hyperthermia plus drug delivery. Like MRI contrast agents, cancer drugs can also be encapsulated or attached to the Fe_3O_4 nanoparticle. These are transported by the nanoparticle to the tumour site and are only released when the temperature exceeds a certain value, providing dual hyperthermia and drug treatment to specifically attack the cancer cells. The ability to regulate the temperature release allows the rate of drug release to be controlled during the treatment and can even be stopped and re-started.[172,173]

1.3 Synthetic approaches for making iron oxide nanoparticles

In nanoscience, there are two approaches for nanosynthesis: top-down and bottom-up. The top-down approach was first suggested by Richard Feynman in his famous American Physical Society lecture in 1959, *"There is plenty of room at the bottom"*, and involves slicing, grinding or successively cutting bulk materials until at least one dimension falls in the range of a few to several hundreds of nanometres.[174] In contrast, bottom-up methods start small by assembling atoms and molecules to construct nanometer-sized objects. This leads to much lower yields, but nanostructures with dimensions less than one nanometer to hundreds of nanometres can be made with greater size, shape and composition control. Hence, bottom-up approaches are often preferred as nanomaterials can be synthesised over a wide size, with well-defined features. Since the transition to the superparamagnetic state depends on particle size, the

majority of approaches for preparing USPION and SPION nanoparticles are bottom-up. Around ~90% of bottom-up methods for preparing USPION/SPION nanoparticles are chemical methods.[175] Chemical methods include co-precipitation[106,159,176], thermal decomposition[139,177,178], solvothermal synthesis[179,180], sonochemical synthesis[181], microemulsion synthesis[94], microwave synthesis[182], polymer-matrix synthesis[183], hydrothermal synthesis[184] and electrochemical deposition[185].

Co-precipitation is arguably the easiest method. Here, Fe^{+2} and Fe^{+3} salts are mixed with base to hydroxylate the ions, producing a Fe_3O_4 precipitate. However, the main disadvantage of co-precipitation is it often produces nanoparticles with a poor crystalline structure[144]. High crystallinity is important as structural defects reduce the magnetic saturation and dampen the superparamagnetic properties.[186] A high magnetic saturation is especially important for biomedical applications, such as MRI contrast agents and hyperthermia treatment. When designing T_2 contrast agents, a high M_S is desired as this creates a larger local magnetic field gradient, helping to de-phase the transverse magnetization of the surrounding protons quicker.[187] This increases the protons T_2 relaxation rate, enhancing the contrast.[186] If the nanoparticle has a low magnetic saturation, it can be difficult to identify tumours from other bright spots in the MRI image .[104] A higher relaxivity also means lower doses of contrast agents are required, making the procedure safer for the patient.[188] In magnetic hyperthermia treatment, a high M_S generates a greater SAR as the ferrofluid is more responsive to the oscillating magnetic field, improving heat losses.[189] In a wider context, it is also a limiting factor in other applications of SPION where high magnetic moments may be required. High temperature methods, such as thermal decomposition of a Fe complex, achieve more uniform crystallinity. However, a degree of magnetic disorder is still introduced in ultra-small nanoparticles whose higher curvature introduces surface defects.[190–192] Using high temperature methods also complicates the synthetic procedure and reduces the green credentials of the synthetic process, leading to a corresponding increase in the cost, all of which are unattractive aspects for industrial scale-up. Therefore, developing modified co-precipitation techniques with greater M_S values could produce high performance nanoparticles using a very simple method.

A number of researchers in the literature have experimented with magnetic field assisted nanosynthesis. This involves exposing the reaction vessel to a magnetic field during the nanoparticle growth. The concept behind this is that the magnetic field will

help align the magnetic moments of the Fe^{+2}/Fe^{+3} ions during growth and improve the crystallinity, hence producing nanoparticles with a higher magnetic saturation. Synthesis of Fe_3O_4 nanoparticles in the absence and presence of a magnetic field has been investigated and the results reflect this theory. Hu *et al.* showed that oxidative co-precipitation of $FeCl_2$ using NaOH and H_2O_2 in the presence of a very weak magnetic field of 22 mT raised the value of M_S by ~ 4 emu g^{-1}.[193] This is a small increase but rather impressive considering that the magnetic field strength used was only ~4 times that of a fridge magnet. Changes in the size distribution curve were also observed when performing the synthesis with increasing magnetic field strengths of 0, 11 and 22 mT. At 0 mT, the size distribution curve was skewed towards small sizes with the average nanoparticle size ~40 nm. However, as the field strength increased, the average nanoparticle size increased and the distribution became more symmetrical suggesting the magnetic field helped improve the size uniformity. As seen in Table 2, similar increases in M_S have been observed by others investigating field assisted synthesis. Table 2 compares the reaction temperature, field strength and M_s values (with and without an applied field) for various magnetic field assisted co-precipitation experiments.

Table 2: Comparison of results from research papers investigating magnetic field assisted co-precipitation synthesis of magnetic nanoparticles. The table shows the material, method, reaction temperature, magnetic field strength (mT) and M_S (without and with the applied field). The nanoparticle size corresponding to each M_S value is shown in brackets.

Material	Method	Reaction Temperature	Magnetic field strength (mT)	M_s (applied field) (emu g^{-1})	M_s (no applied field) (emu g^{-1})	Ref.
$CoFe_2O_4$	Co-precipitation	60-80 °C	30	54 (22 nm)	61(23 nm)	[194]
Fe_3O_4	Oxidative co-precipitation	70 °C	22	68 (~50 nm)	72 (~50 nm)	[193]
Fe_3O_4	Co-precipitation	25 °C	1000	7 (4 nm)	15 (10 nm)	[195]
Fe_3O_4	Co-precipitation	70 °C	ACMF	61 (201 nm)	69 (208 nm)	[196]

In all the examples in Table 2, M_S was increased in the presence of a magnetic field. The largest increase seen was by Wang *et al.* who applied a 1000 mT field around the reaction vessel using an electromagnet.[195] The value of M_S increased by over 8 emu g^{-1} for the USPION Fe_3O_4 nanoparticles. USPION nanoparticles display a very low magnetic saturation. This limits their application in biomedicine where they are highly sought as a smaller nanoparticles have greater cell penetration and administer less iron to the patient.[127,197] However, as Wang *et al.* noted, there is a large difference in the nanoparticle size between M_S (applied field) and M_S (no applied field). Larger nanoparticles have larger M_S values because there are less surface atoms. The lower the number of surface atoms, the less susceptible the nanoparticle is to over-oxidation and/or spin-canting effects that lead to the formation of a magnetically dead surface-layer.[198–201] Spin canting is where the high curvature of the particle causes the atomic moments at the surface to cant away from the external magnetic field, reducing the net magnetization of the nanoparticle. In the Wang *et al.* study, it is difficult to determine the extent to which the increase in the particle size vs. improved crystallinity affected the magnetic saturation. It would be interesting to see whether similar results are obtained with weaker magnetic fields. If weaker fields have less effect on the nanoparticle size, it may be possible to compare the effect of the magnetic field purely based on the structural changes. In addition, many studies have looked at larger SPION nanoparticles synthesised using weak fields and high temperatures, therefore it would be good to further investigate room temperature magnetic field co-precipitation of USPION.[193,194,196,202]

2. Experimental

2.1 Synthesis of Fe_3O_4 using magnetic field assisted co-precipitation

Iron oxide (Fe_3O_4) nanoparticles were prepared via the Massart method[203] using a procedure adapted from ref.[104] Ultrapure water (20 mL) and poly(ethylene glycol) (PEG) (3 mL, MW ~400 g mol^{-1}) were added to a 100 mL round bottom flask fitted with a reflux condenser and bubbled under nitrogen for 1 hour. The reflux condenser was used as an adaptor for the nitrogen bubbler, not for heating. Then $FeCl_3.6H_2O$ and $FeCl_2.6H_2O$ (2:1 ratio) in ultrapure water (1 mL) were injected into the polymer mixture. The polymer mixture was allowed to degas for a further 30 minutes. Upon addition of NaOH (1mL) dropwise, a black precipitate formed immediately. The pH of

the reaction solution was measured as pH = 12.1. Bubbling was continued throughout addition of the base to agitate the reaction mixture. Stirring using a magnetic stirrer bead could not be used as this would just attract to the magnets when making the nanoparticles in the presence of a field. The reaction was allowed to bubble for a further 30 minutes. The reaction mixture was then aged at high pH for two days, before the nanoparticles were separated using a magnet and washed with ethanol and deionized water until the pH was neutralised. The same procedure was used to make the Fe_3O_4 nanoparticles in the presence of a magnetic field. The magnetic field was produced by placing two neodymium disc magnets (N45) around the reaction vessel with their poles aligned. The distance between the magnets was 70 mm. The field strength was measured using a Tesla meter and found to be 40 mT in the centre of the magnets and 120 mT at the edges of the magnets. Fig. 28 shows a picture of the reaction set-up, alongside an illustration.

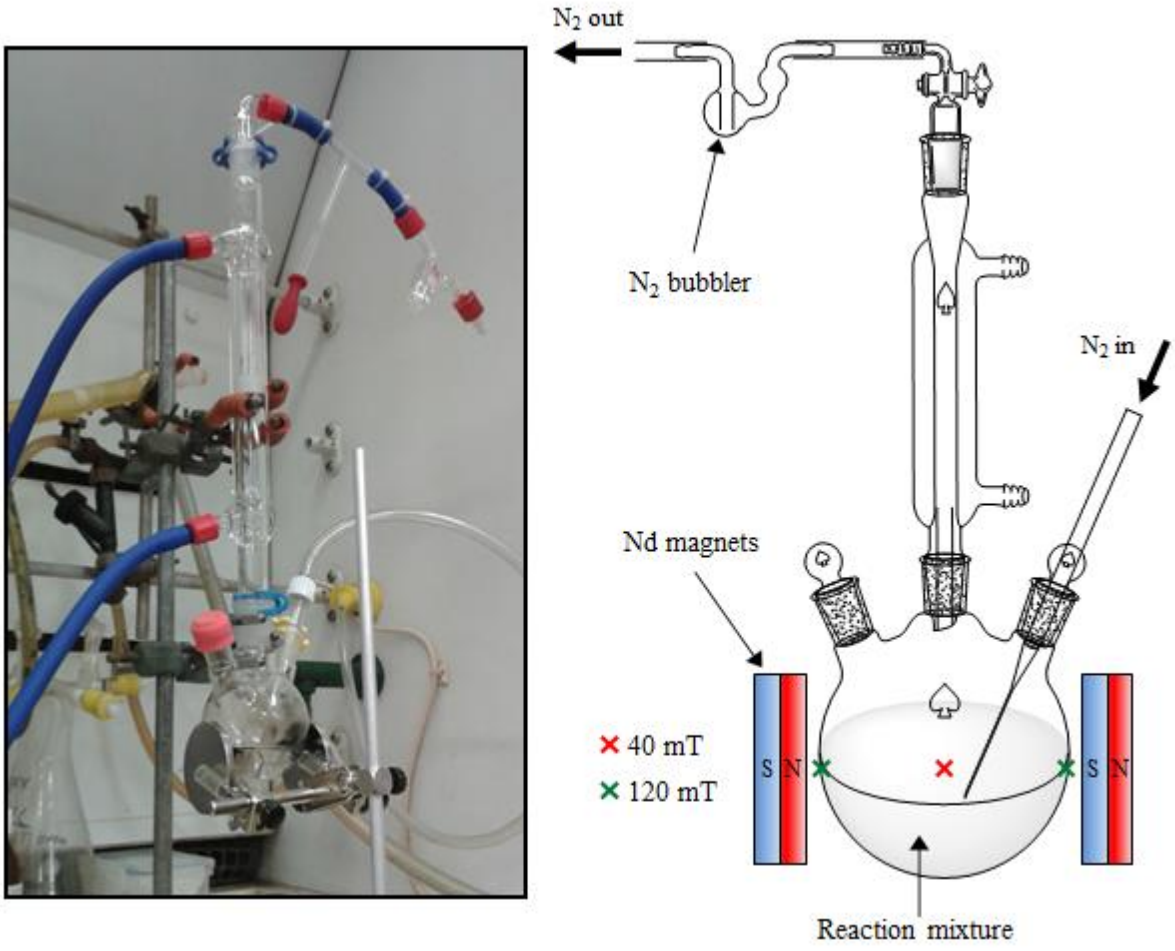

Fig. 28: Picture of the reaction set-up for co-precipitation synthesis of Fe_3O_4 nanoparticles. Next to the picture is an illustration of the reaction set-up, where the field strength at the centre of the two neodymium magnets is indicated by the RED cross and the field strength at the edges of the magnets indicated by the GREEN crosses.

2.2 TEM analysis of nanoparticles

Transmission electron microscopy (TEM) analysis was performed by depositing the nanoparticles onto lacy carbon on copper TEM grids. A few drops of the nanoparticle solution was diluted in methanol (1 mL) and sonicated for 1 ½ hours. Then 1 drop of the diluted nanoparticle solution was pipetted onto the TEM grid. The solvent was allowed to dry in air at room temperature, casting the nanoparticles onto the grid. The grids were then analysed using a JEOL (JEM-2100F) Field Emission Gun (FEG) transmission electron microscope using an electron acceleration voltage of 200 kV. Analysis of the TEM images was performed in ImageJ using the method described in Appendix C.

2.3 SQUID analysis of nanoparticles

Magnetic characterisation was performed using a superconducting quantum interference device (SQUID) magnetometer. A SQUID magnetometer consists of two Josephson junctions across which the voltage is measured. The Josephson junctions are connected to a magnetic coil. Changing the magnetic flux inside the coil induces a voltage response in the Josephson junction, allowing the SQUID to detect very weak magnetic fields. For example, SQUID is often used to detect weak magnetic fields in biological systems. Both the Fe_3O_4 samples prepared with and without a magnetic field were analysed in the SQUID using the same method.[204] A few milligrams of sample was placed into a gel capsule and loaded into a straw which was inserted into the SQUID. *M-H* curves were recorded at both 300 K and 10 K by measuring the magnetization from an applied field of +50 kOe (5 T) to -50 kOe and then back to +50 kOe. Magnetization vs. temperature (*M-T*) curves were also produced for each sample using the zero field cooling warming (ZFCW) - field cooled cooling (FCC) procedure.[205,206] This involved cooling the sample to 5 K in the absence of a magnetic field. *M* vs. *T* data was then collected in an applied field of H = 100 Oe (ZFCW measurement). The sample was the cooled back down to 5 K in the 100 Oe applied field and *M* vs. *T* data collected (FCC measurement).

3. Results

3.1 Analysis of TEM images of Fe_3O_4 nanoparticles

The TEM images of the Fe_3O_4 nanoparticles prepared with and without a magnetic field are shown in Fig. 29. Analysis of the particle size distribution in Fig. 30 shows the average nanoparticle size in image A was 6.96 ± 3.1 nm and in image B was 9.24 ± 3.4 nm. This size increase suggests the application of the magnetic field influenced the growth process and led to the production of larger nanoparticles. The same change in the shape of the distribution curves seen by Hu *et al.* was also observed in Fig 30.[193] The magnetic field reduced the skewness of the lognormal distribution curve towards smaller nanoparticles and shifted the centre towards larger nanoparticles. Furthermore, looking at the TEM images shows differences in the shape of the nanoparticles. Measuring the roundness of the nanoparticles in the images shows neither the nanoparticles in image A or image B are perfectly spherical (i.e. roundness <1). The average nanoparticle roundness for both images was ~0.69 (see Appendix C for calculation). The TEM images suggest the imperfect roundness in image A is exhibited as quasi-spherical polyhedral nanoparticles. Most of the nanoparticles in image B also appear to be quasi-spherical; however, there are more nanoparticles with a more cubic structure, especially in the lower part of the image. Both the increase in the nanoparticle size and morphology changes suggests an improvement in the nanoparticle crystallinity.

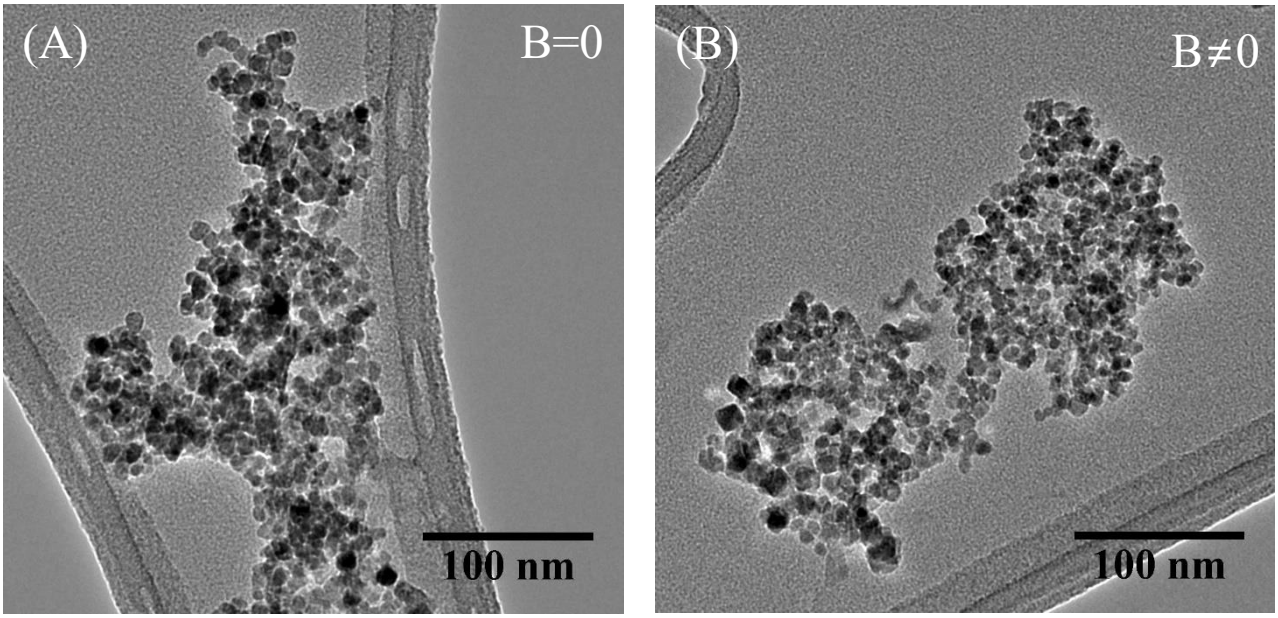

Fig. 29: TEM images of Fe_3O_4 nanoparticles prepared in the absence of a magnetic field (A) and in the presence of a magnetic field (B).

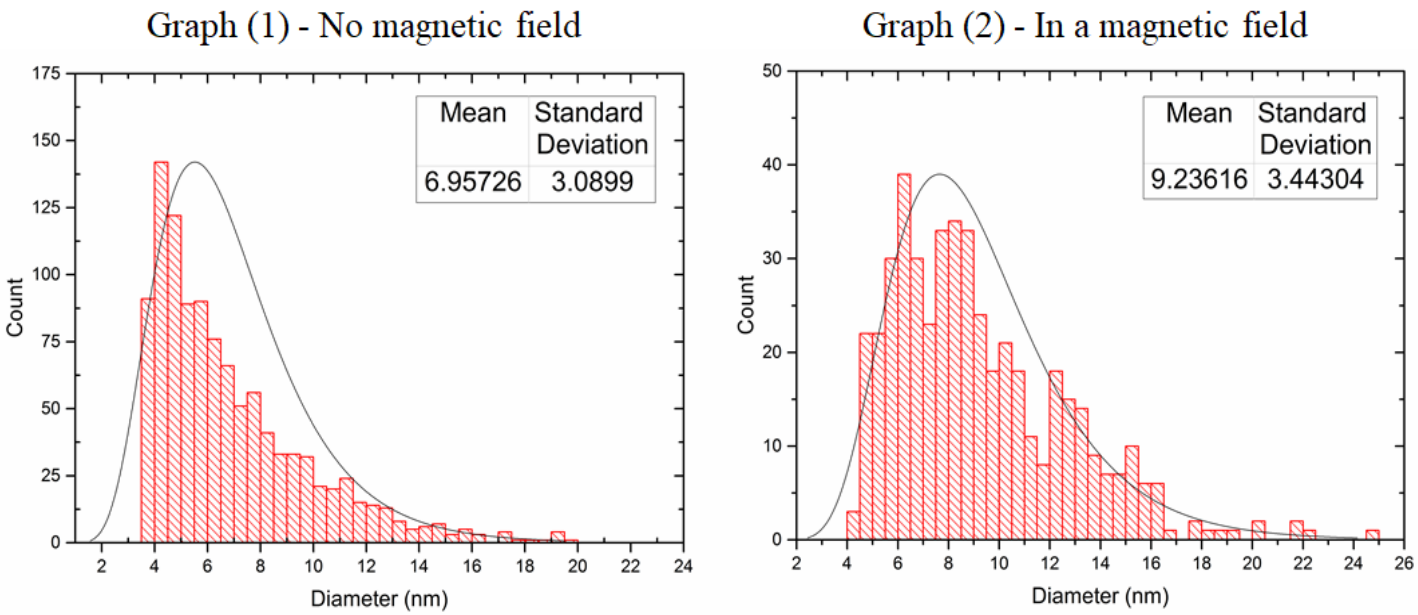

Fig. 30: Histograms for nanoparticle size distribution analysis for the nanoparticles in image A (Graph 1- no magnetic field) and image B (Graph 2- in a magnetic field).

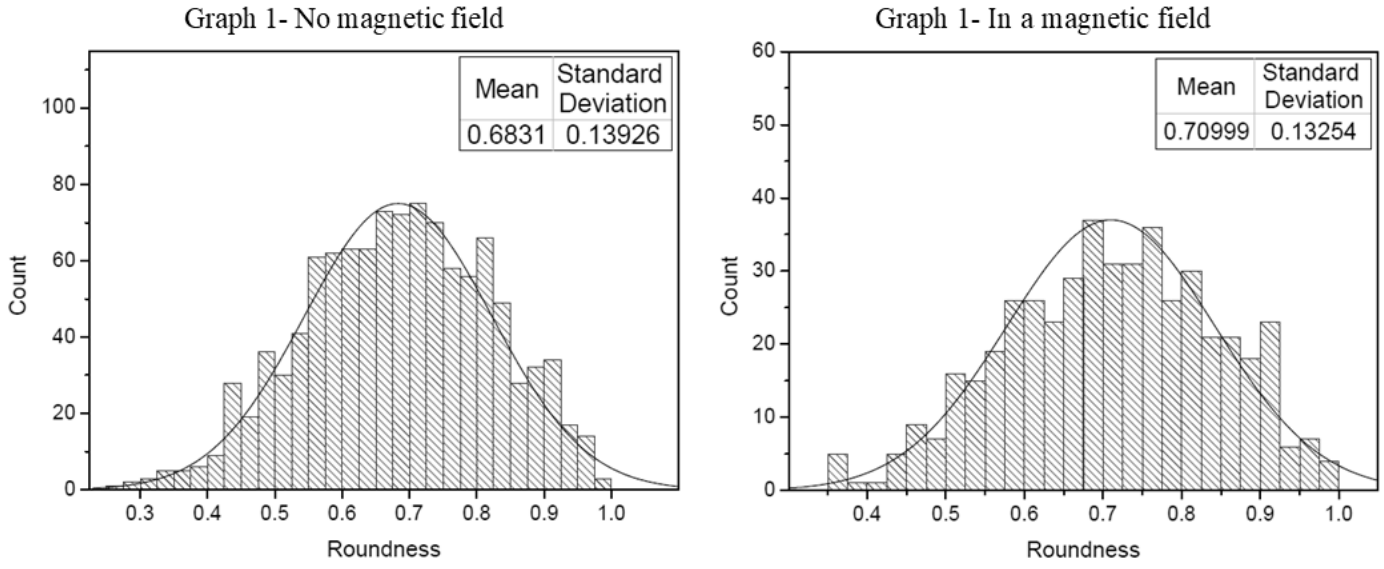

Fig. 31: Histograms for nanoparticle roundness in TEM image A (Graph 1- no magnetic field) and image B (Graph 2- in a magnetic field).

The crystallinity of the nanoparticles was evaluated using high resolution transmission electron microscopy (HRTEM) analysis. The nanoparticles synthesised in the presence and absence of a magnetic field had a single crystal phase indicative of Fe_3O_4. The HRTEM images of nanoparticles prepared in the absence of a magnetic field in Fig. 32 image C had a d-lattice spacing of 4.9 Å, corresponding to the (111) lattice plane of Fe_3O_4.[207] Similarly, HRTEM images of the nanoparticles prepared with a magnetic field had a d-lattice spacing of 2.9 Å, which agrees with the previously recorded lattice spacing for the (220) plane (see Fig. 33 image C).[207,208] Therefore, both images suggest the nanoparticles are Fe_3O_4. Energy dispersive x-ray (EDX) analysis of the TEM images in Fig. 34 concluded that other than elemental contributions from the TEM grid, the sample predominantly contained Fe and O, suggesting the nanoparticles were pure. Other elements were detected (Cl, and Ca, Mg) but can be discounted as they were only detected in small amounts and are likely to come from errors in the detection and/or minor grid contamination during drop-casting. Note, the nanoparticles could not conclusively be identified as Fe_3O_4 without x-ray diffraction (XRD) analysis. Unfortunately, powder-XRD could not be performed. As well as Fe_3O_4 (often called magnetite), there are numerous other phases of iron oxides, for example, maghemite (γ-Fe_2O_3), geothite (α-FeO(OH)), ferrihydrite, wüstite (FeO) etc.[165] Maghemite has the same inverse spinel crystal structure as magnetite. Hence, their crystal structure is very similar making it difficult to distinguish the structures, particularly via HRTEM as their d-lattice spacings are almost the same. The presence of maghemite can be determined by the presence of two additional peaks in the diffraction pattern at 23.77° and 26.10° corresponding to the (210) and (211) phase, respectively.[209] As XRD was not possible, it cannot be ruled out that as well as magnetite, some maghemite structures were also present, most likely on the surface of the nanoparticle where there is greater chance of over-oxidation leading to the formation of γ-Fe_2O_3.[210]

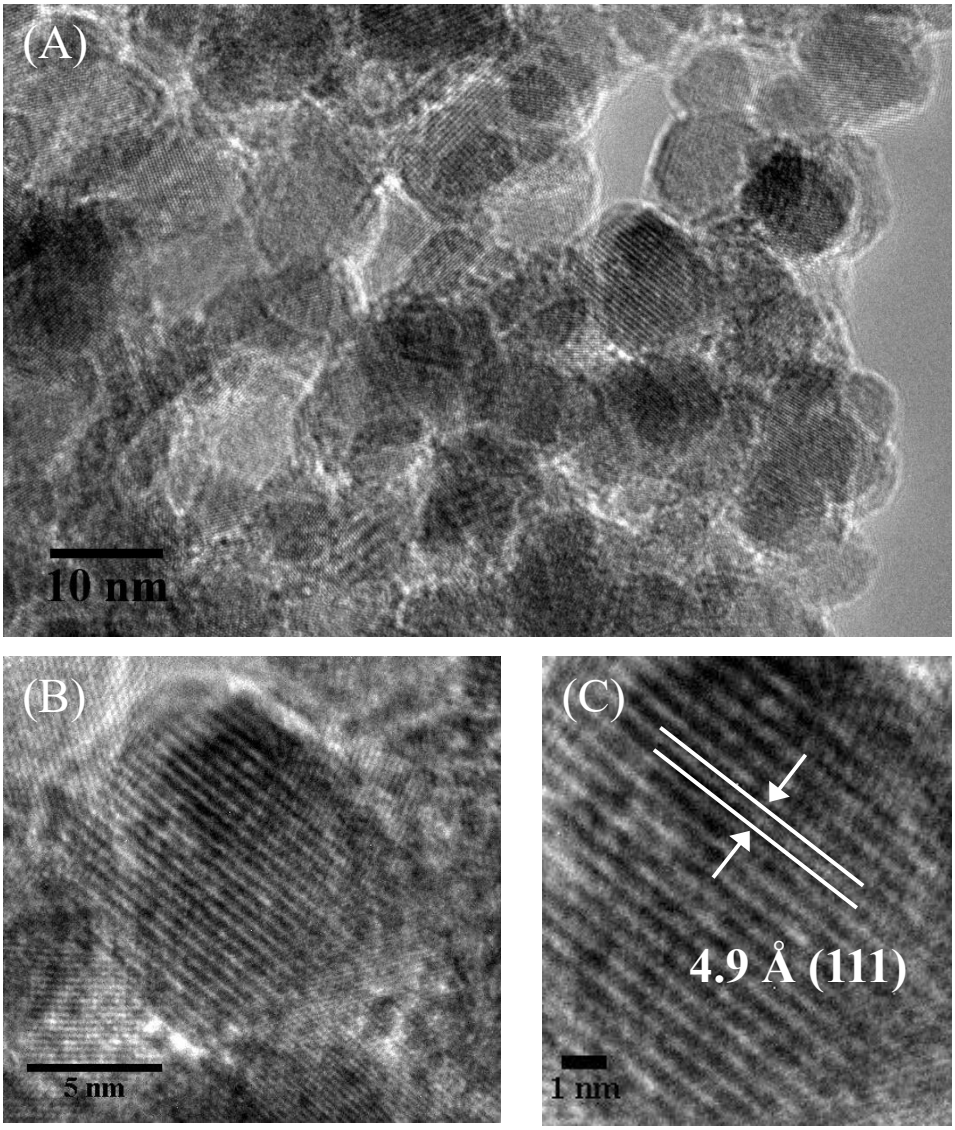

Fig. 32: HRTEM images of Fe_3O_4 nanoparticles prepared in the absence of a magnetic field. (A) Wide field of view image showing the crystalline structure for multiple nanoparticles; (B) crystalline structure of a single nanoparticle; and (C) image showing d-lattice spacing of the nanoparticle in image b.

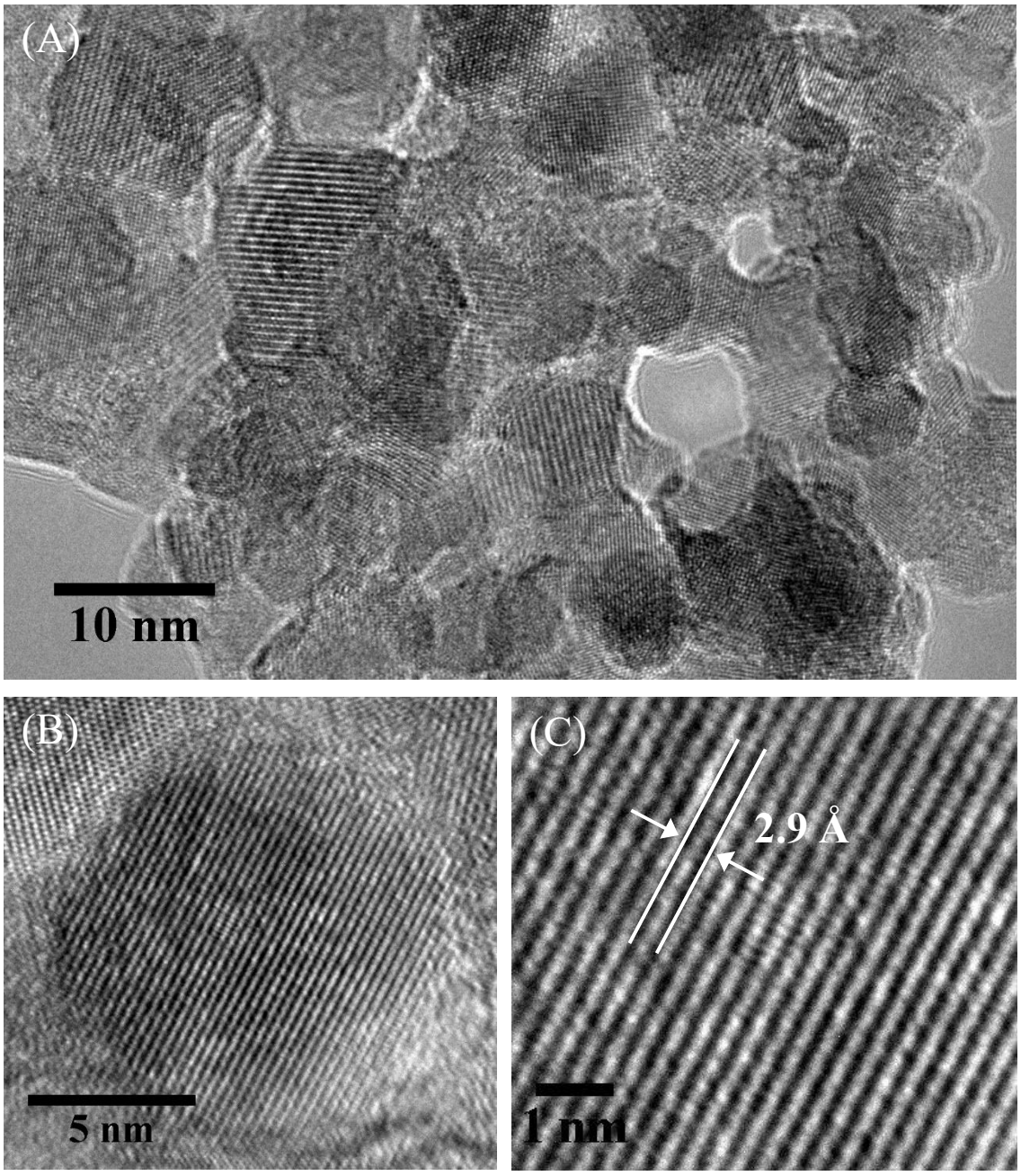

Fig. 33: HRTEM images of Fe_3O_4 nanoparticles prepared in the presence of a magnetic field. (A) Wide field of view image showing the crystalline structure for multiple nanoparticles; (B) crystalline structure of a single nanoparticle; and (C) image showing d-lattice spacing of the nanoparticle in image b.

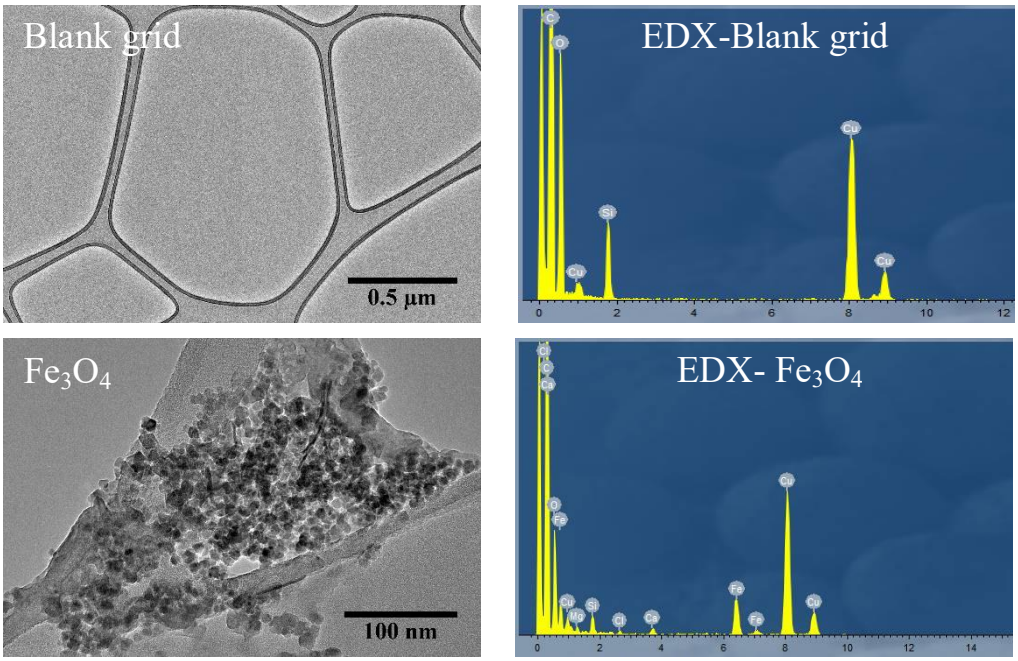

Fig. 34: EDX analysis of a blank TEM grid vs. a TEM grid loaded with Fe_3O_4 nanoparticles.

3.2 Magnetic characterisation of the nanoparticles

A simple observation showing magnetic nanoparticles had been prepared was achieved by placing a fridge magnet next to the dispersed nanoparticle solution. The pictures in Fig. 35 show that after ~15 minutes, the nanoparticles had all been attracted to the side of the beaker where the magnets field strength was greatest.

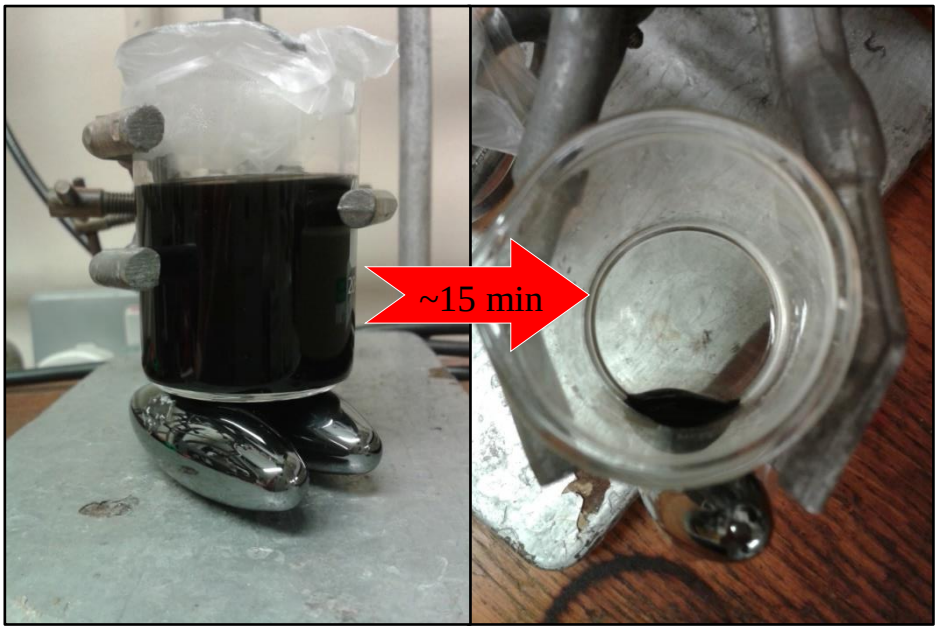

Fig. 35: Pictures illustrating magnetic separation of the Fe_3O_4 nanoparticles using a simple fridge magnet after ~15 minutes.

The magnetization under an applied field between -50 kOe to +50 kOe was measured for both samples at 300 K. Fig. 36 shows the resulting M vs. H curves. Both curves quickly saturate at low fields to a saturation magnetization of 58.2 emu g^{-1} for Fe_3O_4 nanoparticles prepared without a magnetic field and 61.4 emu g^{-1} for Fe_3O_4 nanoparticles prepared with a magnetic field. Therefore, application of the 40 mT field increased the magnetic saturation of the nanoparticles by 3.2 emu g^{-1}. At 300 K, no hysteresis was observed for both samples. However, the inset in Fig. 36 showing the curves behaviour about zero field would suggest there is some remanent magnetization. This is not true as the curves are in fact 'unphysical' in this region. This is because the magnetization measured when the applied field was being decreased to -50 kOe, lied below the magnetization when the field was increasing. This behaviour is caused by the superconducting coil in the SQUID. In a superconducting coil, the trapped field in the coil close to 'zero' field is always slightly negative after decreasing the field from a large positive field. The opposite is true when decreasing the field from a large negative field leading to a slightly positive field. This is the cause of the curve separation about zero-field, not hysteresis. Hysteresis is therefore unobservable meaning the nanoparticles display typical superparamagnetic behaviour.

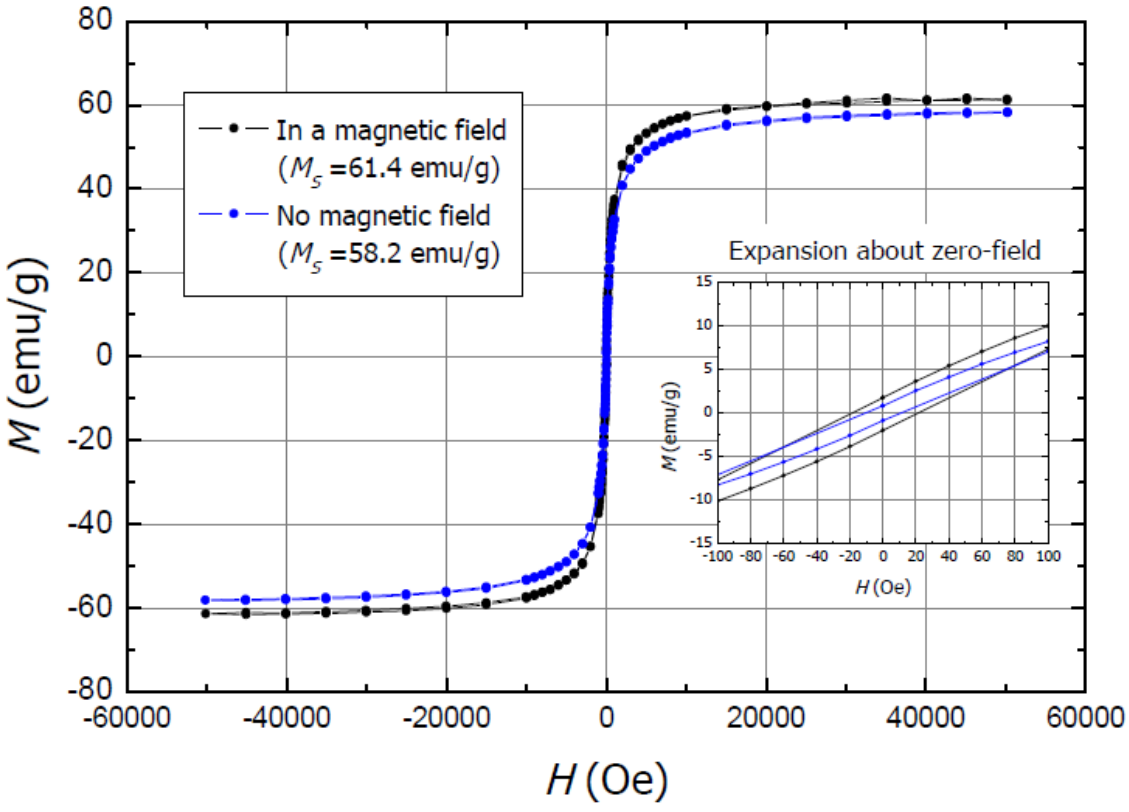

Fig. 36: Magnetization vs. applied field (*M-H*) curve for nanoparticles prepared in the absence (blue curve) and presence of a magnetic field (black curve) at 300 K. The expansion shows the magnetization behaviour about zero-field.

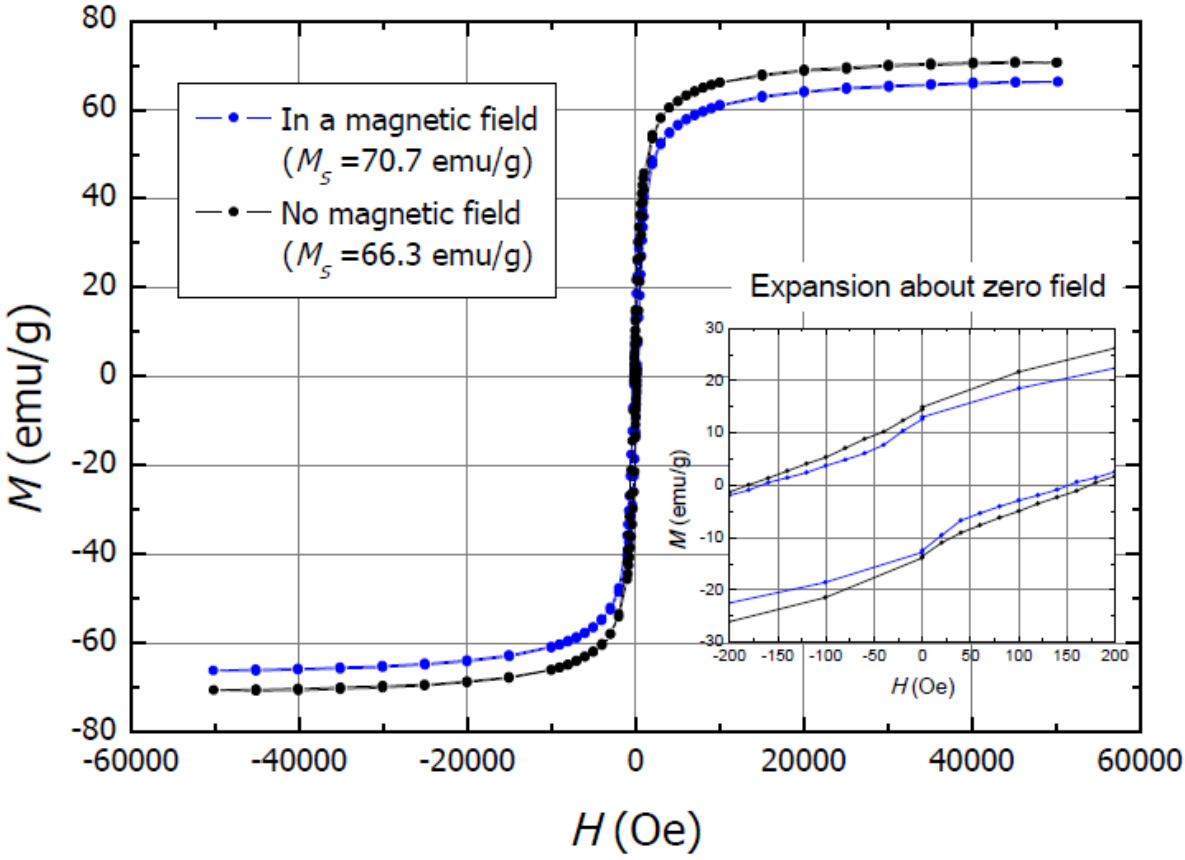

Fig. 37: Magnetization vs. applied field (*M-H*) curve for nanoparticles prepared in the absence (blue curve) and presence of a magnetic field (black curve) at 10 K. The expansion shows the magnetization behaviour about zero-field, which shows low temperature hysteresis.

The *M* vs. *H* curves measured at 10 K are displayed in Fig. 37. As expected, the magnetic saturation at 10 K is higher than the magnetic saturation at 300 K for both samples. Looking at the expansion about zero field shows there is some hysteresis in both curves showing the nanoparticles are well below their blocking temperature. As discussed in section 2.2 of this chapter, if the energy is sufficient, the magnetic moments will randomly flip between the two most favourable orientations along the easy axis, where the time between flips is called the Néel relaxation time, τ_N. As the temperature is reduced, τ_N increases as there is less and less thermal energy to excite the magnetization vector and overcome the anisotropy energy barrier. The temperature at which the time between flips becomes longer than the measurement time is known as the blocking temperature, T_B. The direction of the moment stays the same throughout

the measurement, hence it is said to be 'blocked'. Below T_B the magnetization curve exhibits hysteresis because after applying a large field there is not enough time for the moments to relax back to their thermal equilibrium magnetization at zero field. T_B is given by the following equation:

$$T_B = \frac{K\,V}{k_B \ln\left(\frac{\tau_m}{\tau_0}\right)} \tag{33}$$

k_B is the Boltzmann constant, τ_m is the measurement time and τ_0 is the natural lifetime. The value of the blocking temperature can be determined from the *M* vs. *T* curve. During the initial ZFCW process, the sample is cooled in the absence of a magnetic field causing the moments to become frozen in random directions. A weak field is then applied and the ZFCW magnetization measured with increasing temperature. This is reflected by the black arrow in the *M* vs. *T* curve for the nanoparticles prepared without a magnetic field (Fig. 38). Initially, the magnetization is low as the thermal energy (k_BT) is much lower than the anisotropy energy (KV). There is not enough energy for the frozen moments to respond to the applied field producing a weak net magnetization. As the temperature increases, the magnetization grows rapidly as more moments gain enough energy to overcome the anisotropy energy barrier until the equilibrium magnetization is reached. At this point, the material transitions back into a superparamagnet. As the temperature increases further, the magnetization starts to decline as it becomes harder to align the moments in the direction of the magnetic field because of their high thermal energy. The blocking temperature is represented by the inflection point on the ZFCW curve. In contrast, measuring the magnetization while cooling in the presence of a weak magnetic field (FCC) leads to a gradual increase in magnetization when following the blue arrow in Fig. 38. This is because the weak magnetic field helps align the moments in the direction of the magnetic field producing a highly ordered state upon reaching 5 K. The blocking temperature for the nanoparticles prepared without a magnetic field was determined as T_B= 186. 33 K. Fig. 39 shows the *M* vs. *T* curve for the nanoparticles prepared in a magnetic field was T_B= 219.60 K.

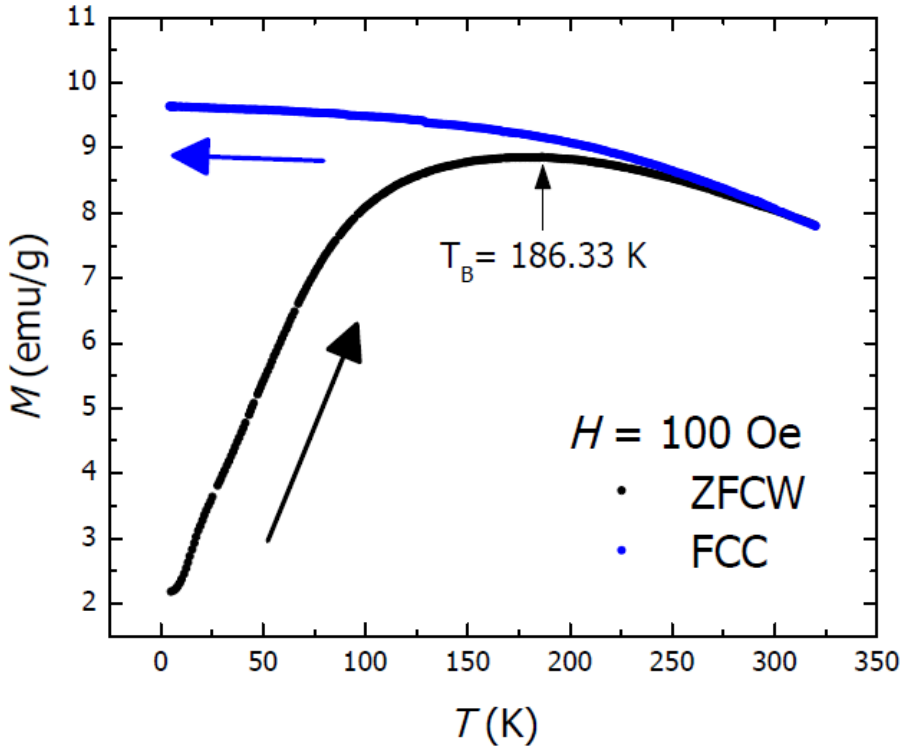

Fig. 38: Magnetization vs. temperature (*M-T*) curve for nanoparticles prepared in the absence of a magnetic field measured using a constant applied field of 100 Oe. The blocking temperature is indicated at the inflection point on the ZFCW curve.

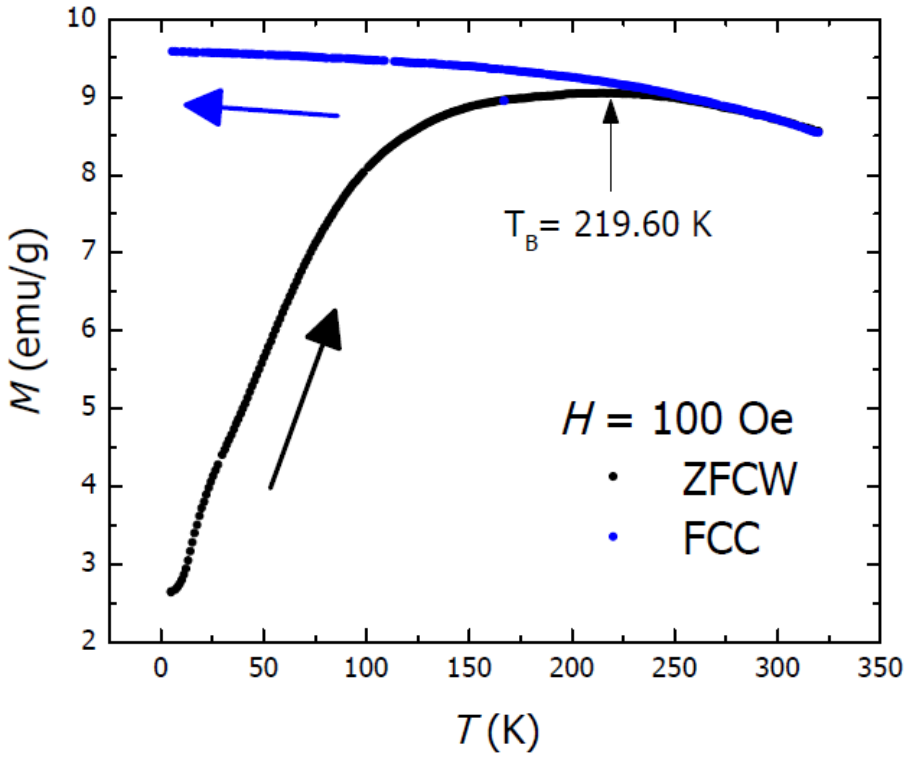

Fig. 39: Magnetization vs. temperature (*M-T*) curve for nanoparticles prepared in the presence of a magnetic field measured using a constant applied field of 100 Oe. The blocking temperature is indicated at the inflection point on the ZFCW curve.

4. Discussion

A number of explanations can be applied to explain the increase in the magnetic saturation from 58.2 emu g^{-1} to 61.4 emu g^{-1} at 300 K. The formation of Fe_3O_4 is thought to occur via the following mechanism[211]:

$$Fe^{+3} + 3OH^- \rightarrow Fe(OH)_3$$

$$Fe(OH)_3 \rightarrow FeOOH + H_2O$$

$$Fe^{+2} + 2OH^- \rightarrow Fe(OH)_2$$

$$2FeOOH + Fe(OH)_2 \rightarrow Fe_3O_4 \downarrow + 2H_2O$$

Some have suggested the magnetic field could hasten the diffusion of Fe^{+3}, Fe^{+2} and OH^- ions in the reaction solution.[212] This makes reactions between the paramagnetic ions more likely aiding the formation of Fe_3O_4. However, the susceptibility of these paramagnetic ions was studied in superconducting magnets under field gradients of 410 kOe^2 cm^{-1}.[213,214] This is substantially greater than the field strength the neodymium magnets used here could have provided. Consequently, the magnetic response of the paramagnetic ions is likely to have been minor, meaning enhanced diffusion is unlikely. Instead, the FeOOH intermediate has been reported to magnetise easily in the direction of weak static magnetic fields as low as 0-250 Oe.[196] The magnetic field strength in the centre of the reaction vessel was 40 mT (400 Oe). Therefore, it is perfectly feasible that FeOOH was influenced by the magnetic field. Alignment with the magnetic field would assist the phase transformation of FeOOH into Fe_3O_4 and encourage nanoparticle growth along the most easily magnetized axis. This results in more controlled crystal growth, producing nanoparticles with less defects and surface disorder, both of which improve the overall crystallinity. It is likely the preferred growth direction is along the (111) crystal plane as this leads to cubic structures.[215] Higher crystallization strengthens the superexchange interaction between the Fe-O-Fe sites throughout the structure.[195] In Fe_3O_4, magnetic interactions occur between ferric ions indirectly via orbital overlap with surrounding O^{-2} or OH^- ions. This type of interaction is known as superexchange and is strongest when the Fe-O-Fe bond angles are between 120-180°.[216] Crystal defects cause the bond angles to deviate, weakening the magnetic interaction and reducing the overall magnetic moment. Uniform crystallisation also reduces the thickness of the

magnetically dead surface layer, preventing canting of the surface spins and increasing the proportion of the magnetic moments which can respond to the applied magnetic field.

However, similarly to previous studies, the average nanoparticle size increased making it difficult to discern whether the size effects or improved crystallinity had the greatest contribution to M_S. Although the HRTEM images show the nanoparticles are crystalline, stronger evidence for improved crystallinity would have come from measuring the XRD pattern of the nanoparticles. If the theory is correct, the diffraction peaks for the magnetic field grown nanoparticles would have been stronger. Since one of the main arguments to explain the enhanced M_S value is improved crystal growth in the presence of a magnetic field, it seems more than feasible that as well as improving structural growth, this also increases the rate growth around the nanoparticle nuclei producing larger nanoparticles. In this case, the average nanoparticle size increased from 6.96 ± 3.1 nm to 9.24 ± 3.4 nm with field assisted synthesis. An increase of 2.28 nm may seem insignificant, but even a small change in size is enough to have an observable influence on the properties. The fraction of surface atoms decreases dramatically with increasing nanoparticle size. Therefore, it is equally plausible that the increase in M_S could be due to the reduction in the thickness of the magnetically dead surface layer as a consequence of the increased diameter. In addition, the distribution curves in Fig. 30 show although the average nanoparticle size is 9.24 ± 3.4 nm for field assisted growth, there are a large proportion of nanoparticles with diameters over 10 nm. These large nanoparticles could have made a greater contribution to M_S than the improved crystallisation.

The presence of large nanoparticles explains why the blocking temperature is higher for nanoparticles synthesised in a magnetic field. T_B can be used as an indication of particle size. As the particle size increases, the magnetocrystalline anisotropy energy increases due to more spin-orbit coupling interactions.[217] This increases the anisotropy energy barrier meaning more thermal energy is required to overcome KV. Now, higher temperatures are required for the nanoparticles magnetic moments to transition from the blocked state to the superparamagnetic state. The results from the *M* vs. *T* curves in Fig. 38 and Fig. 39 are consistent with this concept as T_B= 186.33 K for the 6.96 nm and T_B= 219.60 K for the 9.24 nm nanoparticles. However, others have reported much lower blocking temperatures for similarly sized nanoparticles. For example, Lee *et al.*

synthesised Fe_3O_4 nanoparticles of various sizes using the reverse micelles approach and found for 7 nm spherical nanoparticles, T_B= 105 K.[218] The broadness of the ZFCW curve about the inflection point in both Fig. 38 and Fig. 39 supports contributions from multiple nanoparticle sizes. As well as size, the blocking temperature is also very sensitive to interparticle interactions. Large variations in particle size and interactions between particles, can lead to strong coupling between nanoparticles, adding to the anisotropy energy barrier and making it harder to unblock the magnetic moments of interacting particles.[219,220] Given the size distribution curves are broad it is likely both contributions from different nanoparticle sizes and interparticle interactions were responsible for the elevated T_B values.

5. Conclusions

The results show that even weak magnetic fields can increase the magnetic saturation of ultra-small iron oxide nanoparticles with dimeters in the USPION size range. The room temperature magnetic saturation increased from 58.2 emu g^{-1} to 61.4 emu g^{-1} using this simple magnetic field assisted co-precipitation approach. This method could very easily be applied to increase the magnetization of biocompatible Fe_3O_4 nanoparticles for applications as T_2 MRI contrast agents and magnetic hypothermia treatments, where high M_S values are often required. However, although the magnetic saturation increased as expected, this study revealed the same problem encountered by others researching magnetic field assisted synthesis. It is difficult to determine whether the increase in M_S is a result of improved crystallinity, or the increase in nanoparticle size. This was especially true in this study as XRD analysis could not be used to quantitatively interpret the crystalline structure if the samples. It is possible the magnetic field improves the quality of the growth process, whilst also increasing the rate of nanoparticle growth. This leads to larger nanoparticles, with an improved crystal structure. However, the magnetic field may just make nanoparticle formation easier meaning the improved magnetic properties are a result of size effects. More information about the influence the magnetic field has on the intermediates and the growth process is needed to make predictions about whether the size or improved crystal structure has the greatest effect on M_S.

Chapter 3

Designing a new method for the production of ultra-small high moment magnetic nanoparticles

1. Introduction

1.1 Challenges facing production of ultra-small magnetic nanoparticles

In Chapter 2, the properties and applications of iron oxide nanoparticles were discussed in detail. Control over the magnetic properties was shown to be an important factor when synthesising iron oxide nanoparticles for biomedical applications. Magnetic field assisted co-precipitation was investigated as a route to control the nanoparticles magnetic saturation and produce nanoparticles with higher M_S values. However, as seen in Chapter 2, co-precipitation synthesis led to a broad nanoparticle size, and although the average size fell into the ultra-small nanoparticle range, there were a number of diameters greater than 10 nm. Formation of ultra-small magnetic nanoparticles with diameters >5 nm with narrow size distributions remains a significant challenge.[221] Not only is this synthetically challenging as control over synthesis becomes more difficult at smaller scales, in most cases size reduction also sacrifices the magnetic properties of the nanoparticles. Ultra-small magnetic nanoparticles have much lower magnetic saturation compared to larger nanoparticles. This occurs for a number of reasons including: (1) higher curvature increasing the risk of spin canting; (2) higher surface to volume ratio increasing the probability of over-oxidation; (3) more protecting agents required during synthesis which can negatively influence magnetic ordering; and (4) the introduction of crystal defects.

Ultra-small nanoparticles below 5 nm are of great interest as they are often seen as bridging the gap between the single atomic/molecular level and nanolevel.[222] Hence, they can be regarded as a separate sub-class of nanoparticles with applications in a number of areas. As discussed in Chapter 2, smaller nanoparticles are preferred in biomedical applications as this reduces the payload of inorganic material delivered to the patient and increases cell penetration. In addition, the nanoparticles are more likely

to reach the target treatment site instead of being detected by the immune system leading to unfavourable pharmacokinetic processes such as accumulation in the spleen or liver.[223,224] This lengthens the nanoparticle residence time in the circulatory system and is advantageous in biomedical imaging techniques like magnetic resonance angiography (MRA).[225] MRA is a form of MRI which images blood vessels to detect abnormalities in blood flow around circulatory system.[226] Ultra-small iron oxide nanoparticles perform as T_1 contrast agents for MRA and are preferred as they are excreted over the course of a few days.[227,228] This means they reside in the blood stream long enough for imaging but do not accumulate in the body. In contrast, gadolinium agents are rapidly excreted after entering the body, limiting the length of the imaging window.[104,229] However, although the timescale for imaging is improved, the quality of the image can often be better with gadolinium because of the size effects affecting the magnetic behaviour of USPIONs. To phase out toxic gadolinium contrast agents, the performance of nanoparticle replacements should be equally, if not more competitive.

One solution to overcome the decline in the magnetic properties is to replace iron oxide with zero-valent iron. Zero-valent iron nanoparticles possess a higher magnetization compared to Fe_3O_4 and were recently shown to be superparamagnetic below ~ 5 nm by Tuček *et al.*.[230,231] Remarkably, the corrected magnetic saturation was found to be 185 emu/g, over twice that of bulk magnetite (92 emu/g).[232] Tuček *et al.* also examined the T_2 contrast ability of the Fe nanoparticles (~3.5 nm diameter) prepared by thermal decomposition of iron nitrate. The Fe/TRGO/PEG nanoparticles had a T_2 relaxivity twice that of FeraSpin XXL, a commercially available T_2 contrast agent. This is an excellent result, but is only achievable if measures are taken to prevent oxidation, otherwise the iron nanoparticle will completely oxidize to the metal oxide. In the Tuček *et al.* study, oxidation prevention was achieved by performing the reaction in a hydrogen atmosphere and protecting the iron core with a graphite oxide matrix (TRGO), before functionalisation with biocompatible poly(ethylene glycol) (PEG). However, to achieve this, the nanoparticles had to be prepared under harsh conditions, specifically 1000 °C heating in a quartz glass reactor, and although the individual nanoparticles themselves were less than 5 nm, they were clustered into rings. Therefore, it is more than possible the interparticle interactions contributed to the magnetic response of the nanoparticles. Also, despite the paper showing positive cytotoxicity results, the pharmacological and physiochemical interactions of unusually shaped nanomaterials

with cells have not been profiled to the same extent as spherical nanoparticles.[233]

Alternatively, others have suggested introducing iron through core-shell metal/metal oxide architectures. For example, Yoon *et al.* produced Fe/Fe_3O_4 core-shells by thermal decomposition of $Fe(CO)_5$ under vacuum and nitrogen conditions.[234] The iron cores were first synthesised as seeds followed by annealing in the presence of more iron reagent to form Fe/Fe_3O_4 core-shell nanoparticles with diameters of 16 nm. Yoon *et al.* compared the Fe/Fe_3O_4 nanoparticles with Fe/FeO nanoparticles of the same size and showed without the iron oxide shell, the magnetization declined rapidly. For the Fe/Fe_3O_4 nanoparticles, the magnetization was higher to begin with (142 emu/g instead of 92 emu/g for Fe/FeO) and only slightly declined after 83 days. Similar results have been obtained by Zhang *et al.* and Yang *et al.* using microemulsion and solvothermal techniques where in both cases M_S exceeded 100 emu/g.[235,236] It has also been noted that in addition to an increase in the magnetic moment, exchange coupling between the ferrimagnetic Fe_3O_4 shell and Fe core can unlock a number of new properties. What more these properties could be tuned by varying the thickness of the core-shell layer to modify the exchange interaction.[237,238] However, in most cases, the dimeter of the Fe/Fe_3O_4 core-shells falls outside the ultra-small range considered here. Synthesis of core-shells less than 5 nm in dimeter will be difficult to characterise due to the thinness of the layers. It is also likely the thickness of the shell will not be sufficient to prevent oxidation of the underlying core. Therefore, coating inert metals such as gold is likely to provide better protection for very small nanoparticles.

1.2 New electrochemical method for synthesising ultra-small iron nanoparticles

As discussed above, one of the main difficulties synthesising ultra-small biocompatible magnetic nanoparticles <5 nm, is obtaining a method which is both simple and prevents oxidation of the iron core. The most preferable synthetic methods from an industrial perspective are methods which produce high quality nanoparticles using few steps, little resources (i.e. reagents, energy and waste) and avoid toxic chemicals.[146] Electrochemical methods have been far less exploited for nanosynthesis, despite having a number of attractive advantages over wet chemical and physical methods. These advantages include, but are not limited to:

(1) Simple design. Electrochemical reactions are relatively easy to set-up and are one of the simplest methods of preparing pure metal nanoparticles, compared to

other physical methods such as cluster beam assemblies. Cluster beam synthesis of nanomaterials involves evaporating the target material (e.g. via laser pyrolysis, resistive heat or ablation)[239–242] into a carrier gas in which the atoms aggregate to form nanoclusters. Where these methods require vacuum equipment and high energy sources, electrochemical synthesis is simply achieved by passing a current through an electrode(s) into an electrolyte.[243,244] The simplicity of the method also makes it more adaptable to changes in reactor design intended to optimize nanosynthesis. For example, the design can be adapted to allow continuous flow synthesis.

(2) Inexpensive. In line with point (1), simple design often goes hand in hand with low costs. This is true for electrochemical methods as once the reactor has been built the major costings are electrical use and reagent materials.

(3) Electrochemical methods offer much greater control over the reaction. Kinetic control can be employed by altering the current through the electrochemical cell. Thermodynamic control is exerted by changing the cell potential. This allows more flexibility to optimize the reaction conditions and can even allow *in situ* control during the reaction. This is arguably one of the most attractive features of electrochemical methods.

One electrochemical method that has recently been applied to nanosynthesis is plasma electrochemistry. Plasmas are one of the four states of matter, along with gases, liquids and solids. Plasmas are made when enough energy is provided to make atoms release electrons, forming a partially- or fully-ionized medium of electrons, ions and neutrals. Negative and positive species are present in equal amounts maintaining charge neutrality. The high density of ions makes plasmas a highly oxidising environment that has been exploited in various plasma technologies across science and in the wider World.[245] In the scientific world, plasmas have been used to study the break-down of gases and liquid. The earliest example of this dates back to 1785 when Henry Cavendish produced nitric acid by plasma discharge in air.[246] Plasmas are also used in analytical chemistry to prepare samples for analysis.[247,248] Other applications include electrical switching devices[249], waste water treatment[250,251], materials processing[252,253], sterilization[254], medical treatment (e.g. wound healing and tissue ablation)[255], and more recently nanosynthesis[256].

The behaviour of the plasma state in liquids is less well studied compared to in the gas phase. Consequently, much of the fundamental properties, such as generation, interactions and active chemistry, are poorly understood.[257] The reason for this is the complexity of the interactions between the plasma species and surrounding liquid. Nanosynthesis formation is possible using gas phase plasma methods, but these methods are very similar to cluster beam step-ups i.e. they require complex electrode design and vacuum conditions.[258–260] Liquid phase plasmas are far simpler, more adaptable and allow nanoparticles to be prepared in various conductive liquid media.[261] As a general 'rule of thumb', the best solvent in which to perform nanosynthesis, is the solvent that matches the environment for their intended use. For example, biological systems are aqueous; therefore nanoparticles designed for both *in vivo* and *in vitro* biomedical applications are most often prepared in water.

The limited use of liquid phase plasma methods means plasma nanosynthesis is largely in its infancy, with few reports pre-2005.[262] However, in more recent years, a variety of nanostructures composed of both single, alloy or core-shell materials in a variety of shapes have been synthesised using liquid plasmas. This includes ultra-small nanoparticles composed of PtAu alloy[263], Au[264,265] and Pt[266], where the average diameters were between approximately 2 nm to 7 nm. In all these reports, the nanoparticles were highly crystalline and non-aggregated. In the case of PtAu and Au, the nanoparticles were made using a pin-to-pin electrode geometry. Application of a high voltage (HV) to one of the pins produces a plasma when placed millimetres from the other pin electrode acting as the ground. Consequent Joule heating of the HV electrode releases metal ions into the solution. These ions are subsequently reduced and aggregate at the cathode to produce ultra-small nanoparticles in the surrounding solution. In contrast, ultra-small Pt nanoparticles were synthesised using a pin-to-plate geometry. In this case, plasma discharge from the stainless steel pin electrode was used to reduce H_2PtCl_6 dissolved in water to form Pt nanoparticles. The ground electrode was a plate lying at the bottom of the reaction container.

In 2014, Kelgenbaeva *et al.* demonstrated solution plasma discharge could be used to make pure iron nanoparticles.[267] This was done by immersing two 5 mm pure Fe electrodes into a beaker of toluene and water so the inter-electrode gap was 1 mm. An alternating current (AC) (100 V, 6 A) supply was provided to one of the electrodes generating a pulsed plasma discharge, while the other electrode was vibrated to help

ensure uniform discharge.[268] Kelgenbaeva *et al.* claim that the toluene-water emulsion prevented the formation of reactive oxygen (O_2^-) and hydroxyl (OH^-) species avoiding oxidization the pure nanoparticles. Pure α-Fe nanoparticles with an average dimeter of 9.5 nm and saturation magnetization of 125 emu/g were produced. In addition, the nanoparticles were prepared without the need for surfactants and capping agents as aggregation was minimal. Formation of non-aggregated ultra-small magnetic nanoparticles without the need for organic protective agents is attractive in many respects. It simplifies the synthesis and allows for further functionalisation later on in the process. More importantly, this could help preserve the magnetization of the nanoparticles. Capping agents are known to have varying effects on the surface magnetization of nanoparticles, and in some cases can enhance spin-canting effects and increase the thickness of the magnetically dead surface layer.[269] These results are encouraging and suggest an analogous method could easily be designed to produce ultra-small iron nanoparticles.

1.3 Designing a novel liquid plasma reactor for synthesis of ultra-small iron nanoparticles

The aim of Chapter 3 is to propose a novel design for liquid phase plasma nanosynthesis of pure iron nanoparticles. To do this, the suitability of various electrode geometries will be investigated. This is arguably one of the most important design considerations as it will ultimately determine the nature and properties of the plasma. The proposed mechanism for plasma formation will also be described. Another important feature is the arrangement of the electrodes with regard to the solution. Ideally, the design should make it easy to separate the nanoparticles from the solution and also have the flexibility to add more components to the reactor. The scalability of the design towards large scale synthesis will also be reflected upon.

2. Experimental – developing the design for a liquid plasma reactor to make ultra-small iron nanoparticles

2.1 Power source for plasma generation

Liquid plasma discharges can be produced by various methods. These include:

(1) Direct discharge between two closely spaced electrodes submerged in an electrolyte
(2) Gas discharge between the electrode and electrolyte
(3) Contact discharge between the electrode and electrolyte
(4) Laser, radio frequency and microwave generation.

Direct discharge and contact discharge are most commonly used for plasma nanosynthesis. Examples of direct and contact discharge electrode geometries are shown in Fig. 40. Both methods essentially involve connecting the electrode to a power supply which feeds a specified current and voltage to the working electrode. If the voltage is low and the current high, an electric arc is produced.[270] These conditions are typically used for large electrode diameters in constant application, which normally applies to contact discharge conditions (e.g. in Fig. 40 (F)). Alternatively, high voltages and low currents can be used creating a corona discharge.[271] Both direct and contact the discharge can be continuous, alternating or pulsed. Continuous discharge conditions are generally harder to maintain and less reproducible.[271] Therefore, many liquid plasma sources operate using alternating or pulsed power supplies. Reproducibility is particularly important as variations in the discharge conditions could have a large impact on the nanoparticle morphology. Because of this, the power source will be a pulsed high voltage (HV) power source with a direct discharge electrode geometry. The exact voltage at which discharge will occur depends on various factors, namely the electrode surface area, pulse width, dielectric strength of liquid, electrode polarity, inter-electrode distance, electrode shape, electrode dimensions and symmetry (i.e. identical anode and cathode (symmetric), non-identical anode and cathode (asymmetric)).[272] Numerous papers have reported using voltages less than 1 kV with currents less than a few amps to produce plasma nanoparticles.[263,266,267,273,274] Such power can easily be provided using low cost power supplies.

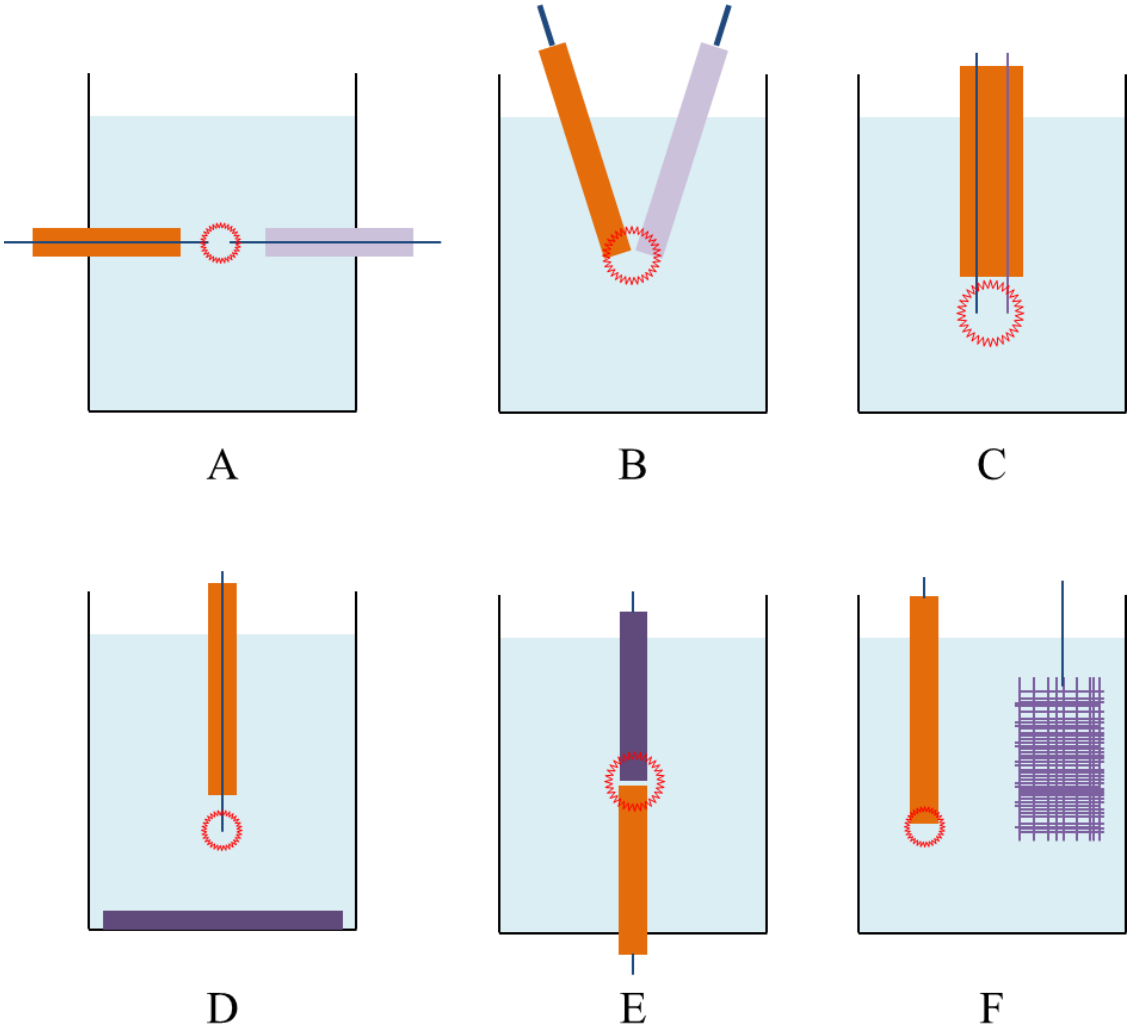

Fig. 40: Schematics of the various direct discharge (A-E) and contact discharge (F) electrode geometries. The geometries can be described as follows: **(A)** pin-to-pin; **(B)** angled rod-rod; **(C)** sideways pin-to-pin; **(D)** pin-to-plate; **(E)** rod-to-rod; and **(F)** rod-to-mesh**.**

2.2 Electrode geometry and reactor design

As seen in Fig. 40, there are various electrode geometries to choose from for direct discharge. From these geometries, it is clear some are suited to batch nanoparticle synthesis, whereas others could be adapted to allow continuous synthesis. By ‘batch synthesis’ this means the electrode discharge is powered for an allotted amount of time and the nanoparticles are collected in the reactor vessel, often falling to the bottom. The opposite of this is continuous nanosynthesis where plasma discharge operates non-stop, generating a constant supply of nanomaterial. Continuous synthesis is attractive for a number of reasons. Firstly, continuous reactor designs are less susceptible to changes in

reaction conditions that are inherently introduced in batch designs by stopping and restarting the reaction. Secondly, continuous synthesis is easier to scale-up as multiple continuous reactors can be arranged side-by side. This leads onto the third point, which is increased reaction yield as nanomaterial is continually being produced. Liquid plasma has already been hailed as the electrochemical method which could bridge the gap between the low yield physical methods and high yield wet chemical methods currently used for nanoparticle synthesis. For example, some have quoted energetic yields of 0.02 mg J^{-1} for liquid plasma systems.[275] The working below shows this corresponds to a yield of ~43 g of nanomaterial over the course of one hour.

$$Power\ (W) = Voltage\ (V)\ \times\ Current\ (I) = 100\ V\ \times 6\ A = 600\ W$$

$$Joules\ (J) = Power\ (W) \times time\ (s) = 600\ W\ \times\ 3600\ s = 2.16\ \times\ 10^{6}\ J$$

$$Nanoparticle\ yield\ per\ hour\ (g) = (2.16\ \times 10^{6}\ J)\ \times\ (2\ \times 10^{-5}\ g\ J^{-1}) = 43.2\ g$$

Others have suggested yields as high as 100 g per hour can be obtained.[276] Fourthly, continuous synthesis avoids aggregation or agglomeration as the electrolyte is continuously moving.[277] Of these various direct discharge geometries, the rod-to-rod (E) and pin-to-pin geometry (A) appear to be particularly suited to continuous design. It can be imagined that a reactor could easily be built where the electrodes are inserted into a vessel where fluid can flow perpendicular to the electrodes and through the inter-electrode gap. Continuous synthesis has been identified as one of the most important features when designing new liquid plasma reactors and there a few existing examples.[278] One of the few examples was provided by Lee and co-workers. They developed a continuous plasma reactor whereby the electrolyte is pumped through a cell containing two tungsten electrodes in a pin-to-pin geometry (see Fig. 41 for a simplified schematic of the reactor design). They have used this to synthesise silver nanoparticles by cycling $AgNO_3$ in water and tcetyltrimethylammounium bromide (CTAB) surfactant past the plasma discharge generated by connecting the electrodes to a pulse power supply.[279] Discharge at 200 V led to reduction of Ag^{+} to form Ag nanoparticles, whose size increased over time as the clusters repeatedly cycled through the inter-electrode gap. In a separate study, Lee *et al.* also demonstrated they could use this same continuous reactor design for applications beyond nanosynthesis. Instead of nanoparticle formation, plasma discharge at the tungsten electrodes was used to destroy

rhodamine B polluted water.[280] This is a common problem due to the wide use of rhodamine B in textiles and food.

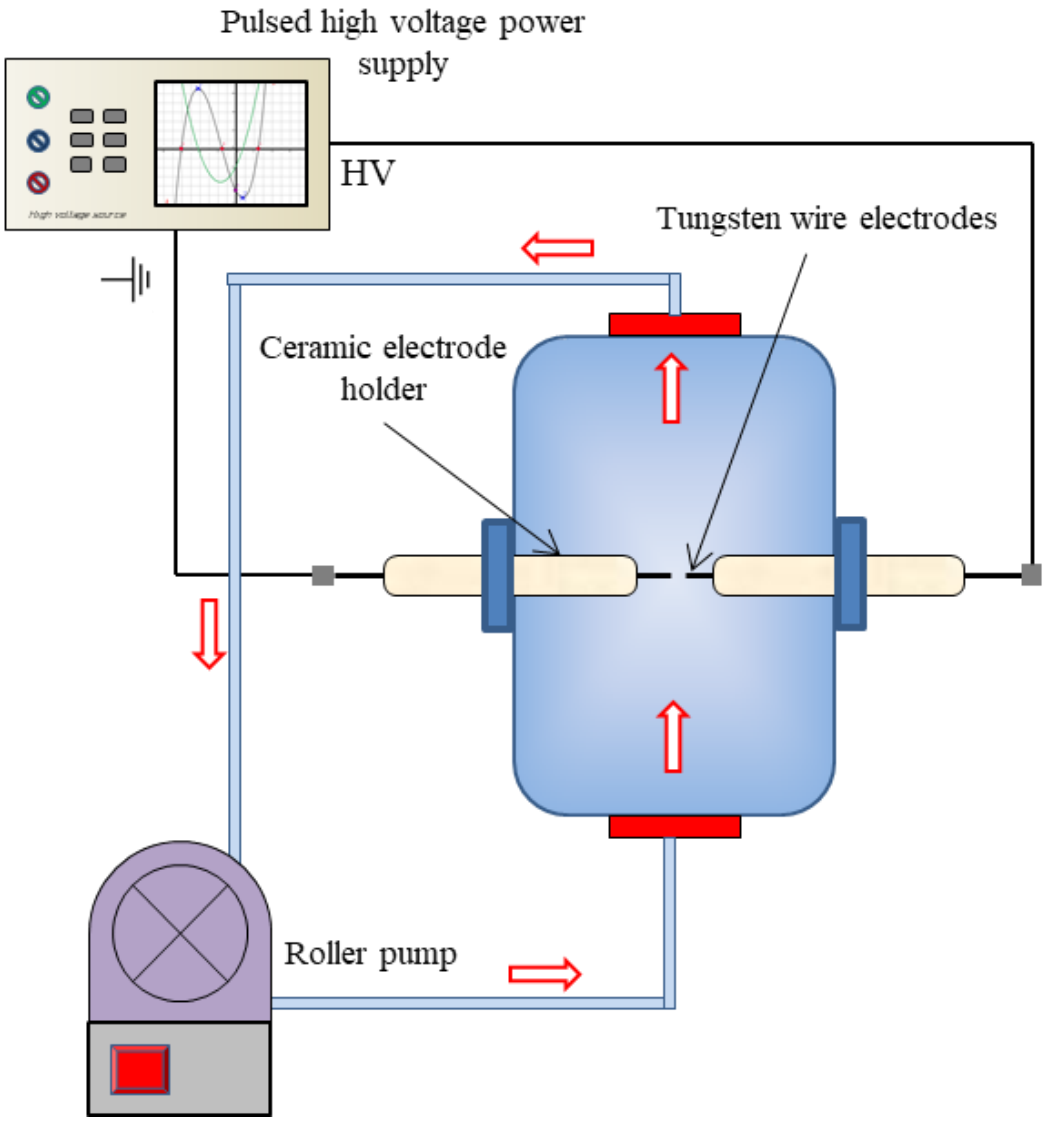

Fig. 41: Adapted illustration of reaction set-up used in the Lee *et al.* study for continuous liquid plasma synthesis of silver nanoparticles.[278]

In another example, Dzimitrowicz and co-workers have produced a number of papers on their continuous flowing liquid electrode design reproduced in Fig. 42.[281] Here, the reaction solution containing the nanoparticle precursor flows from a reservoir and up through a capillary. As the solution comes out the top of the capillary, it falls down the sides under gravity. The solution spilling over the edge is in contact with a tungsten cathode and graphite covered Pt anode, generating a discharge which reduces the metal ion to produce nanoparticles. The nanoparticle solution is collected in a well at the base of the reactor and pumped out into a second reservoir. Dzimitrowicz *et al.* have used this flowing liquid plasma reactor to make gold, platinum and silver nanoparticles.[282–286]

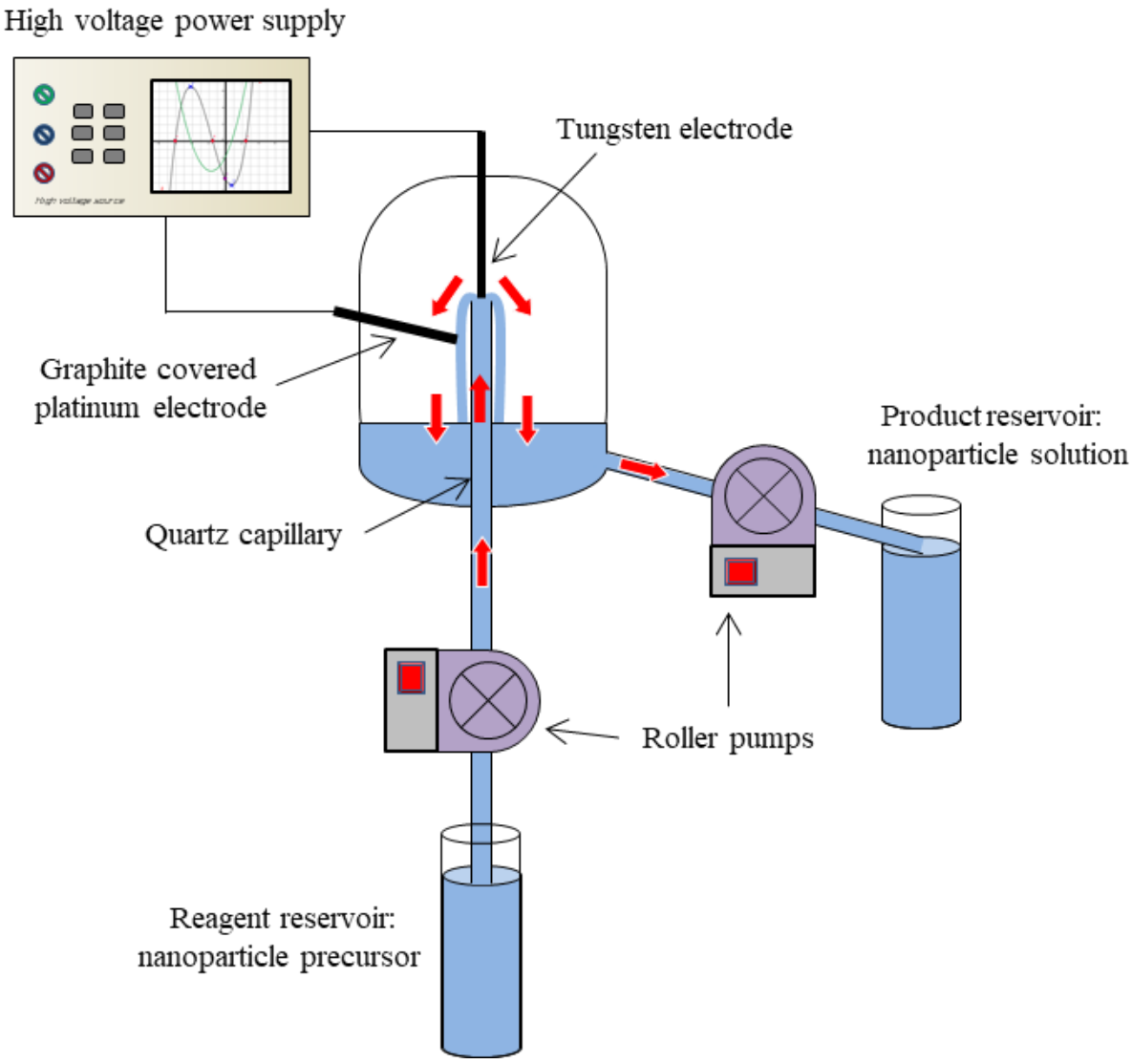

Fig. 42: Continuous flowing liquid plasma reactor designed by Dzimitrowicz *et al.* [280]

The disadvantaged of the approach used in the Dzimitrowicz *et al.* study is the reaction system is not a closed cycle. The precursor solution has to be continually fed with fresh reagent to keep the flow through the reactor constant. However, in the design by Lee *et al.*, the solution could be cycled around in a closed loop. Yet, as eluded earlier, this could lead to 'over-processing' of the nanoparticles as they encounter the plasma more than once during the reaction cycle. This identifies on of the main problems with continuous plasma reactors. It is difficult to separate the nanoparticles from the electrolyte whilst the process is running. This can lead to an increase in the average diameter and is a particular problem when designing a liquid plasma reactor to synthesise ultra-small nanoparticles. That is unless the intention is to make magnetic nanoparticles. In which case, it seems more than feasible that this problem could be overcome by incorporating a magnetic filter into the flow system.

3. Results and discussion

3.1 Proposed design for liquid plasma synthesis of iron nanoparticles

The design considerations discussed in the experimental section have been adapted to design a liquid plasma system to synthesise ultra-small ion nanoparticles (<5 nm) for various applications. A schematic of the design is shown in Fig. 43. The reactor allows nanoparticles to be continuously produced by cycling the electrolyte through the plasma discharge in a closed loop system. The main components along the synthesis loop are labelled alphabetically. The sequence of the synthesis process is as follows:

Step 1: The electrolyte reservoir (A) – This marks the initial starting point along the loop, where the chosen electrolyte is stored. The reservoir container is fitted with a dual particulate and magnetic filter. The job of the particulate filter is to remove any debris which could damage the diaphragm pump. The filter will also contain magnets to remove any remaining magnetic nanoparticles which were not separated by the magnetic nanoparticle filters (K). The electrolyte is pumped out of the reservoir using a diaphragm pump (B). All the internal components of the diaphragm pump in contact with the electrolyte are plastic. In fact, all the components in the reactor cycle are insulators (plastic or glass) to avoid charging as a result of discharge into the conductive electrolyte.

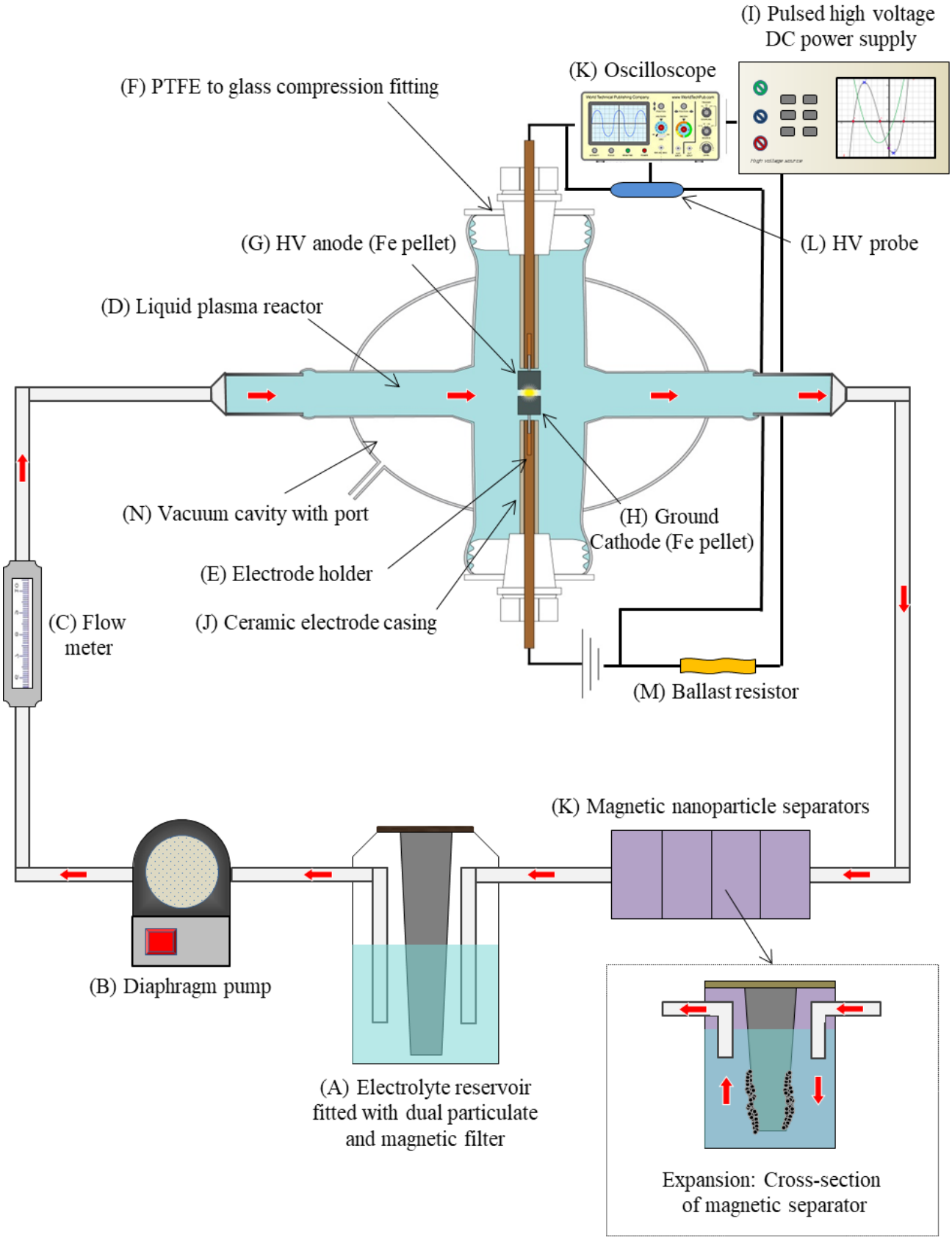

Fig. 43: Proposed design for liquid plasma system to make ultra-small iron nanoparticles.

Step 2: Flow meter (C) – The flow meter indicates the rate at which the electrolyte flows around the cycle in litres per minute (L/min). The flow can be controlled in various ways. One method is to vary the direct current supplied to the pump using a variable switch to change the motor speed. Alternatively, the flow rate could be adjusted using a regulating valve at the end of the cycle in-between the magnetic separator (K) and reservoir (A). As the valve is closed a differential pressure between the fluid coming from the pump and fluid returning to the reservoir is created reducing the flow rate. The accuracy of this method depends on the quality of regulator and this puts a limit on the maximum flow rate which can be obtained. In the long term, the first method is more accurate and reproducible, but the second approach can be implemented for initial testing.

Step 3: The fluid enters the glass liquid plasma reactor (D) and flows thorough the discharge zone between the electrodes. The electrodes are symmetrical and both composed of pure iron pellets (99.95+% purity, 3.5 mm diameter) mounted onto a stainless steel (SS) electrode holder (E) using a threaded SS bar which screws into the tapped holes in the pellet and electrode holder. The electrode was designed in this way so the electrode pellet can be easily exchanged. The electrodes are positioned parallel using a polytetrafluoroethylene (PTFE) compression fitting (F) that screws into a threaded glass port. Which electrode is the anode (G) or cathode (H) depends on the polarity of the high voltage direct current (DC) power source (I). The power source is connected to both the Fe electrodes using the electrode holder as the conductive contact. The bottom surface of the electrode should be polished to a mirror shine to create an even surface and improve homogenous discharge. The surface of the electrode should be investigated by Scanning Electron Microscopy (SEM) before and after to identify changes in the surface morphology during the discharge process. This will give an indication of the lifetime of the electrode and nature of the discharge process. Electrode lifetime is an important factor to consider given the reactor is intended to operate for long periods of time. The electrodes were surrounded by a ceramic casing (J). It has been observed that encasing the electrode in an insulating ceramic or glass sheath helps to achieve controlled discharge and reduced degradation of the electrode surface.[287] In this instance, the electrode gap will remain fixed at 0.5 mm. The inter-electrode gap is known to have an effect on the discharge voltage; however, precise control over the gap distance complicates

the design. For the preliminary experiments, it is easier to adjust the applied voltage. The output voltage from the power supply is measured using an oscilloscope (K). The actual voltage applied to the electrodes is measured using the second channel of the oscilloscope with a high voltage probe (L). The output is connected to a ballast resistor (M) which prevents the current from rising too high causing arc formation.

A mechanism for nanoparticle formation under pulsed DC discharge conditions has been suggested and is detailed as follows.[264,288–290] When the pulsed high voltage is initially applied, the response is a large increase in the current due to the formation of an electrical double layer at the electrodes. An electrical double layer forms whenever a surface is exposed to a liquid. Depending on the charge of the surface, oppositely charged species will be attracted to the surface, while similarly charged species are repelled creating a potential gradient across the interface. The potential gradient is high at the surface, but decays to zero as the distance from the surface increases, at which point the bulk solution is reached. As the voltage increases during the pulse, the formation of a vapour sheath around the electrode due to evaporation of the electrolyte takes over causing the electrical double layer to collapse. The current decreases because the electrode and electrolyte are no longer touching. The thickness of the vapour sheath (or plasma sheath) can vary between 10 μm to 1 mm.[291] This vapour layer contains gaseous reactive ions and neutrals from the electrolyte, and its collapses at the end of the pulse causes bubbles and streamers to the ejected into the solution. This process occurs repeatedly for each pulse resulting in Joule heating which melts the electrode and results in ejection of metal ions/atoms into the electrolyte every time the vapour layer collapses. As the discharge region cools down between pulses, the atoms aggregate and condense as they collide with species in the surrounding electrolyte leading to nanoparticle formation. This is depicted in Fig. 44.

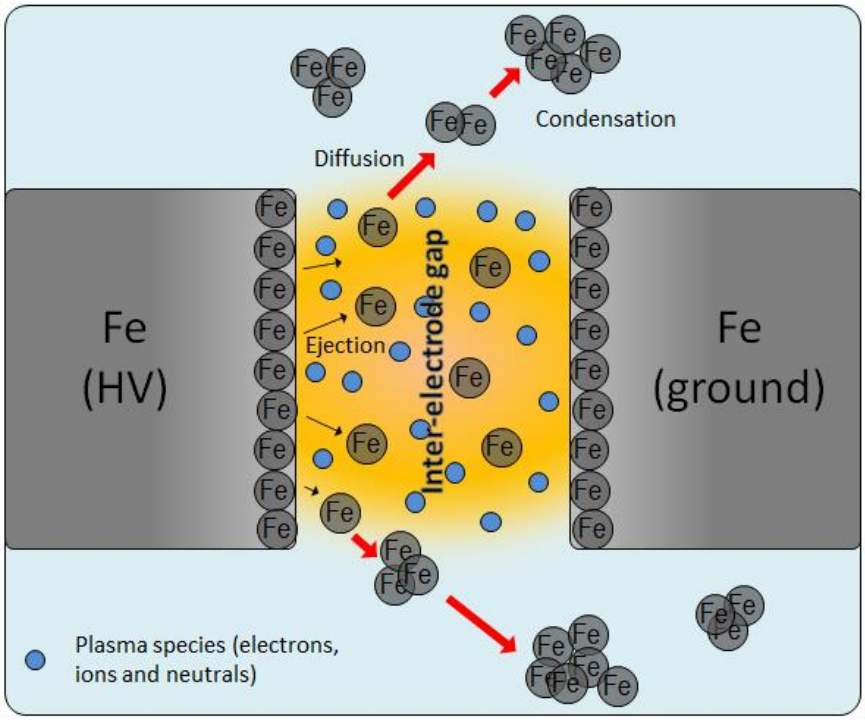

Fig. 44: Proposed mechanism for nanoparticle formation during pulsed plasma discharge in an electrolyte.

Step 4: Magnetic separation – The final step in the cycle is separation of the nanoparticles from the electrolyte fluid coming from the plasma reactor. The proposed method for doing this is to have a series of magnetic separators where fluid undulates through a series of magnets. As the nanoparticles travel though the separators, they become attracted to the magnets and are removed from the solution (as shown in the expansion in Fig. 43). The pure electrolyte can then flow back to the reservoir and go around the cycle again. Since the magnetic susceptibility of the nanoparticles decreases with size, a strong magnetic field will be required trap the nanoparticles. For this reason, there are a series of magnetic separators to trap as many nanoparticles as possible. This may also lead to size separation of the nanoparticles as the larger nanoparticles are likely to be easily trapped by the first separator, while the smaller nanoparticles will the filtered out by subsequent separators. It may be worthwhile designing the separators so the magnetic field strength increases through the series to ensure adequate separation. This could be advantageous for improving size uniformity.

3.2 Experimental parameters to investigate

There are a number of experimental parameters to investigate. All these parameters can be tuned and optimized to achieve the desired nanoparticle characteristics and are detailed in the following sub-sections.

3.2.1 Choice of electrolyte

Various liquids can be used as the electrolyte as long as they are conductive. Example electrolytes include water, hexane, ethanol, emulsions (e.g. water + toluene) and even liquid nitrogen. The voltage at which discharge occurs will vary depending on the conductivity of the liquid.[261] If desired, surfactants can also be added to perform synthesis and functionalisation in one step. It would be interesting to investigate synthesis with and without a surfactant to determine whether non-aggregated nanoparticles can be made without protecting groups. Since the aim is to make pure iron nanoparticles, the chosen electrolyte must not contain reactive oxygen species to avoid iron oxide formation. Plasma nanoparticle synthesis in liquid nitrogen has been performed by various groups and could be a method to avoid oxidation.[264,270,276,292,293] However, this is definitely not something to attempt before testing the experiment with liquids which are easier to handle. Cycling liquid nitrogen around the system would involve using a pressurised dewar and all the components in the reactor would have to be adapted to withstand temperatures of -196 °C. Suitable materials would be either glass or PTFE. The liquid plasma reactor (D) has been designed with use of liquid nitrogen and other cold liquids in mind. The glass reactor has been custom made so the crosspiece is enclosed in a glass vacuum cavity (N) which can be pumped out to prevent condensation around the reactor making it difficult to observe the electrode discharge. The vacuum cavity can be seen more clearly in the 3D CAD drawings of the plasma reactor in Fig. 45.

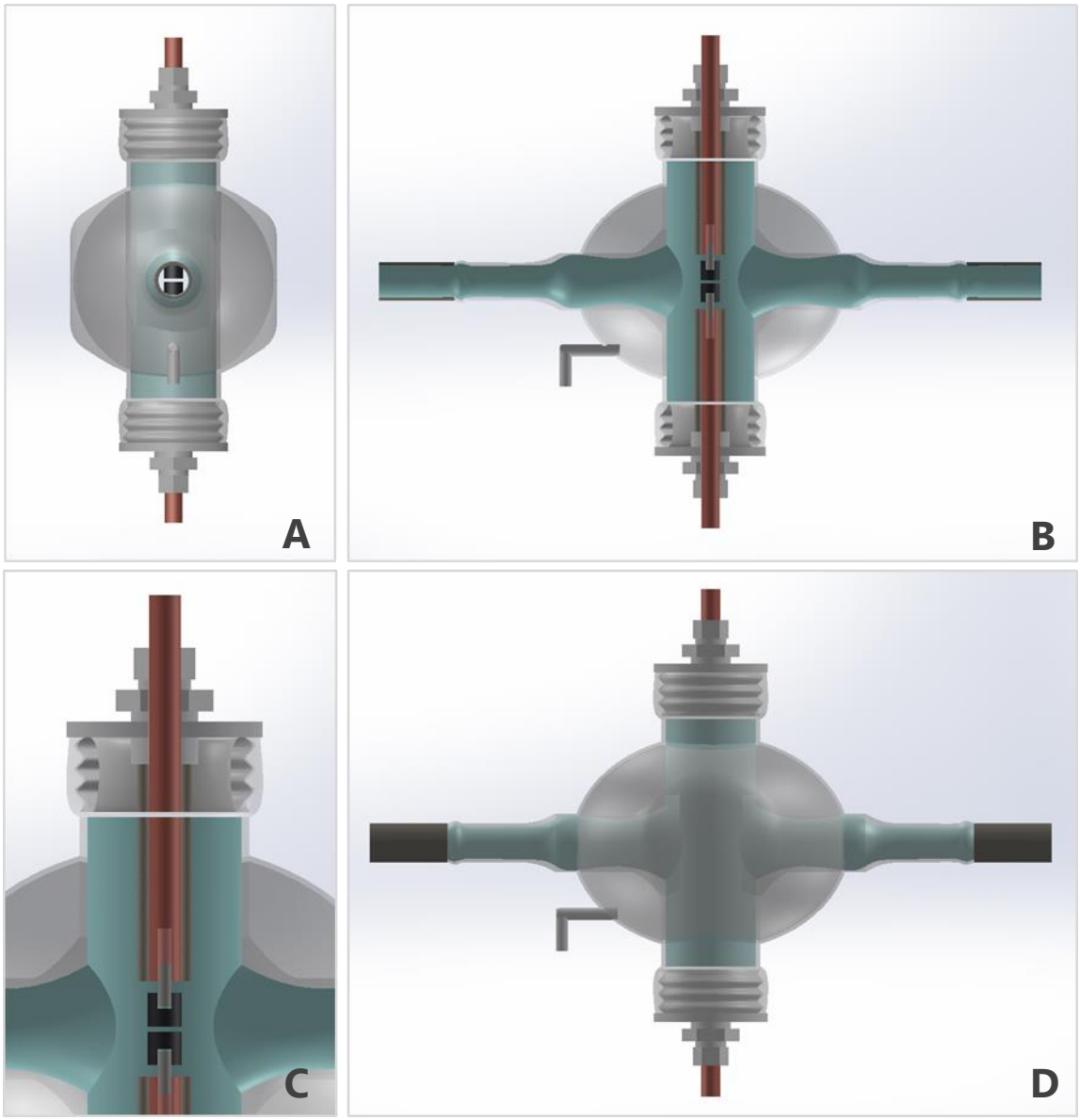

Fig. 45: 3D computer aided design (CAD) drawings of the liquid plasma reactor from various angles. Designs were created using SolidWorks. (A) Shows the side-view of the plasma reactor. Observe the flattened sides which allow a magnet to be placed close to the discharge zone. (B) A cross-sectional view through the centre showing the electrode configuration. (C) An expanded image of the cross-sectional view in (B) showing the electrode design. (D) View of the plasma reactor from the front showing the vacuum cavity around the discharge zone.

3.2.2 Flow rate of electrolyte

Intuitively, the motion of the solution through the inter-electrode gap is more than likely to affect the distribution and diffusion of reactive electrons, ions and neutrals in the discharge zone. Ultimately, the rate of flow will have an effect on the nanoparticle size, and possibly the nanoparticle morphology. Dzimitrowicz *et al.* observed such an effect with their flowing liquid electrode reactor. By measuring the absorption wavelength the gold nanoparticles, they observed the nanoparticle size decrease with increasing flow rate through the capillary. Gold nanoparticles exhibit surface plasmon resonance (SPR) and absorb visible light at specific wavelengths, whose exact value depends on their size. Consequently, SPR is often used as a cross-reference technique to check average nanoparticle size determined from TEM analysis. Therefore, flow rate is an important parameter to investigate. By varying the flow rate, it may be possible to tune the average nanoparticle size from the USPION to SPION size range.

3.2.3 Discharge voltage

The discharge voltage is a very important parameter to investigate. For controlled discharge, the pulse voltage should be optimized to find the value at which plasma formation is visible. By visible this means light, bubble and streamers can be seen to propagate from the discharge region. This represents the point at which the current starts to drop due to break down of the electrical double layer. As the pulse voltage is increased, the plasma region extends further and the plasma sheath thickens around the electrode, which glows more intensely due to the increased light discharge. When this condition is reached the electrode is said to be in a full-plasma state with the current completely depleted. The full plasma state is more uncontrolled and the discharge sporadic in nature, often leading to the formation of over-oxidized products with an ill-defined morphology.[287] Therefore, the intention is not to keep ramping up the voltage until pulsed discharge assumes the full plasma state. Instead, by selecting a series of gradually increasing voltages in-between the partial-plasma (the state before transition to full plasma where the current varies) and edge of the full-plasma state, the effect of the voltage on the nanoparticle size and morphology can be investigated. It has been found that the average nanoparticle size decreases with increased voltage.[294] This has been explained by Toriyabe *et al.* who synthesised Ni, Ti, Ag and Au nanoparticles using plasma discharge.[273] It is proposed that as the amount of inputted heat improves

thermal diffusion between the current hotspot and the surrounding area, causing Joule heating to become less localised. As a result, instead of the metal vapour being concentrated at the current hotspot, it is more extensive, allowing the metal species to spread further as the electrode material is ejected into the solution. This means fewer collisions between metal atoms/ions in the electrolyte producing smaller aggregates. Others have also observed changes in nanoparticle shape with increasing voltage, for example transitions from spherical nanoparticles to nano-flowers.[295]

3.2.4 Effect of magnetic field on plasma discharge

It is no surprise that the electric field of a plasma would respond to the presence of a magnetic field. However, there are few reports where a magnetic field has been introduced to the electrode region. The few studies which have been conducted suggest the magnetic field can enhance the synthesis of carbon nanomaterials made in the discharge zone between carbon electrodes. Keidar *et al.* report the length of single walled carbon nanotubes increased upon application of a magnetic field.[296] The nanotubes also had increased purity and fewer structural defects. Keidar and co-workers also applied a magnetic field to synthesise graphene flakes by placing a permanent magnet 1.2 kG (0.12 T) next to the carbon electrodes.[297] They reported an increase in the plasma density and improved heating; and ultimately improved the growth rate of the nanostructures. Performing discharge experiments with and without a magnetic field would be interesting to see if there were any size changes or improvements in crystallinity. For this reason, the sides of the reaction vessel have been flattened to allow a permanent magnet(s) to be placed either side of the discharge region as seen in Fig. 45 image A.

3.2.5 Re-configuration of the liquid plasma reactor to form multi-element nanostructures

It is also possible the plasma reactor can be adapted to synthesise multi-element nanostructures, for example alloys and core-shells. As demonstrated here and in Chapter 2, bimetallic nanoparticles are as equally valued as pure nanoparticles, as the introduction of new elements can improve and allow for manipulation of the properties. Alloy nanoparticles can quite easily be prepared by using a bimetallic alloy electrode. By choosing alloys with different compositions, the metal ratio can be adjusted. Recently, Kabbara *et al.* have demonstrated synthesis of core-shell Cu/ZnO

architectures by plasma discharge in liquid nitrogen.[293] This involved a two stage batch process where the core material was synthesised by discharge from copper electrodes. The copper electrodes were then removed from the reactor and replaced with zinc. Discharge into the pre-loaded mixture coated the copper nanoparticles with Zn. Zn quickly oxidized to form a ZnO layer around the copper core. The Cu/ZnO core-shell structure could be clearly distinguished from TEM images. The main problem with this approach is the need to switch the electrodes. The synthesis would be far simpler if the core-shell architectures could be made in a single step. This may be possible using the plasma design proposed here. For instance, by adding another plasma reactor before or after the iron plasma reactor it may be possible to make core-shell structure, or even multi-core shell structures by having more than two plasma reactors in series. This would be particularly advantageous when trying to make pure iron nanoparticles. As the illustration in Fig. 46 shows, the pure iron nanoparticles made by discharge in the first plasma reactor cell could be transported to a second plasma reactor cell composed of gold or silver electrodes. This would create a biocompatible noble metal shell around the iron core, protecting it oxidation and preserving the magnetic moment.

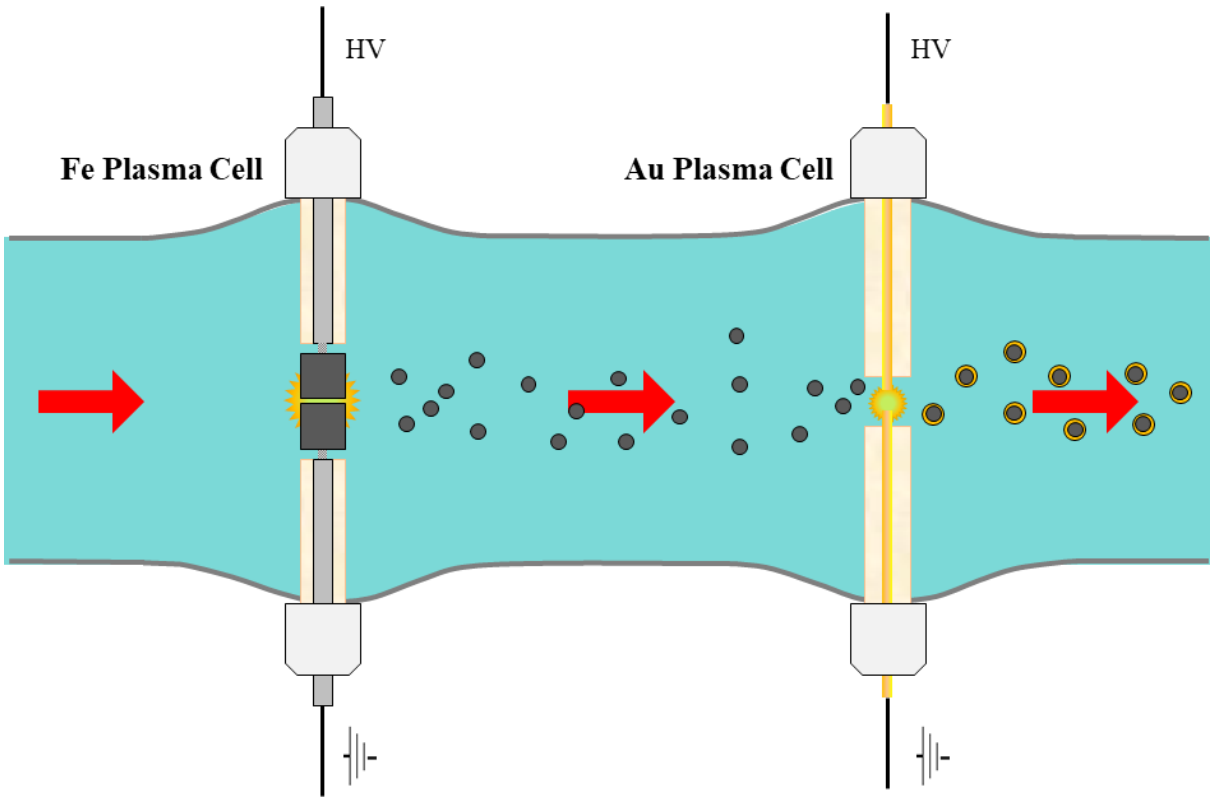

Fig. 46: Illustration of adapted plasma reactor design to produce core-shell nanoparticles. The electrolyte flows through two plasma reactor cells in series. Iron nanoparticles are produced by discharge in the first cell, and then travel onto the second plasma cell where they are coated in gold to produce core-shell structures.

4. Conclusion and future work

In this chapter, a design for a novel liquid plasma reactor has been suggested to synthesise high moment iron nanoparticles. The design has been developed to produce biocompatible magnetic nanoparticles exhibiting a high magnetic saturation in the lower portion of the ultra-small size regime, where the diameter is <5 nm. Other design features such as scalability and adaptiveness have also been considered. By combining continuous discharge and magnetic separation, the reaction is designed to operate as a continuous closed loop. This is attractive for scale-up because it is a single-step process, reduces variability in reaction conditions, and increases the nanoparticle yield. Once built, there are various parameters to investigate to determine the optimal synthesis conditions, including the electrolyte, voltage, response to magnetic fields and flow rate. No doubt these experiments will foster new ideas and/or improve other elements of the design. It is possible the reactor could be adapted in future versions to allow core-shell synthesis by placing two discharge reactor cells in sequence. This could further protect the magnetic moment of the pure iron nanoparticle from oxidation if the shell was an inert and biocompatible material, such as gold or silver.

Conclusion to Thesis

This thesis has investigated two very different research topics. The first research topic was based upon superfluid helium droplet science and was discussed in Chapter 1. In Chapter 1, computational studies were performed to understand the fragmentation of conjugated molecules in superfluid helium droplets upon electron ionisation. This work was stimulated by the unusual p-benzoquinone fragmentation pattern which showed almost complete loss of the parent ion peak in the helium droplet mass spectrum. This is very unusual as conjugated molecules tend to have high molecular ion peaks and the helium droplet is expected to 'soften' electron ionisation. Density functional calculations were used alongside the experimental data to propose a model explaining the reduced parent ion signal. The calculations suggest that for the parent ion to 'escape' from the droplet, it must either fragment and lose CO/C_2H_2, or be ejected intact. This is because there is no proton loss pathway due to the large energy required to remove a proton from the carbon ring. Ejection of the large parent ion from the droplet poses a high energy barrier, forcing most of the molecule to dissociate and eject a C_2H_2. More experimental evidence is needed to determine whether other conjugated molecules fragment in the same way. A number of candidate molecules, which were shown to have similarly high energy proton loss channels, have been proposed. This would strengthen the theory and encourage further computational studies that could reveal more information about the helium droplet electron ionization process.

The second research topic was the focus of Chapters 2 and Chapters 3 and involved investigating methods to prepare high moment iron oxide/iron nanoparticles. Iron oxide nanoparticles have many applications, however synthesising magnetic nanoparticles with high magnetic moments remains a challenge. In Chapter 2, magnetic field assisted synthesis was applied to the co-precipitation method. This approach has been previously successful at increasing the value of M_S for iron oxide nanoparticles. Here, the aim was to investigate the influence of weak magnetic fields on ultra-small nanoparticle growth. SQUID magnetometry showed an increase in the magnetic moment (58.2 emu g^{-1} to 61.4 emu g^{-1}) for Fe_3O_4 nanoparticles upon application of an external magnetic field (40 mT), suggesting an improved crystalline structure. However, one of the main issues of this technique is a broad nanoparticle size, which was observed in this study. It is also difficult to achieve magnetic saturation values close to that of bulk Fe_3O_4. One idea to

make biocompatible magnetic nanoparticles with even higher moments is to replace Fe_3O_4 with pure Fe. This can be achieved using an electrochemical method known as liquid plasma nanosynthesis. In Chapter 3, a design for a continuous liquid plasma reactor to make pure iron nanoparticles in the ultra-small (<5 nm) region was proposed. Future work would involve constructing the design and testing the various parameters to optimize the experimental procedure. This could allow the production of exceedingly high moment nanoparticles for biomedical applications in high yields using a scalable method. In addition, the design could be adapted to synthesise various other nanomaterials for similar and alternative applications.

References

1. Gomez, L. F., Loginov, E., Sliter, R., Vilesov, A. F. Sizes of large He droplets. *J. Chem. Phys.* **135**, 154201 (2011)

2. Sliter, R., Gomez, L. F., Kwok, J. & Vilesov, A. Sizes distributions of large He droplets. *Chem. Phys. Lett.* **600**, 29 (2014)

3. Yang, S., Ellis, A. M. Helium droplets: a chemistry perspective. *Chem. Soc. Rev.* **42**, 472 (2013)

4. Grebenev, S., Hartmann, M., Havenith, M., Sartakov, B., Toennies, P., Vilesov, A. F. The rotational spectrum of single OCS molecules in liquid ^{4}He droplets. *J. Chem. Phys.* **112,** 4485 (2000)

5. Toennies, J. P., Vilesov, A. F. Superfluid helium droplets: A uniquely cold nanomatrix for molecules and molecular complexes. *Angew. Chem. Int. Ed.* **43**, 2622 (2004)

6. Toennies, J. P., Vilesov, A. F., Whaley, K. B. Superfluid Helium Droplets: An Ultracold Nanolaboratory. *Phys. Today* **54**, 31 (2001)

7. Stringari, S., Treiner, J. Systematics of liquid helium clusters. *J. Chem. Phys.* **87**, 5021 (1987)

8. Chin, S., Krotscheck, E. Systematics of pure and doped ^{4}He clusters. *Phys. Rev. B. Condens. Matter* **52**, 10405 (1995)

9. Kamerlingh, H. Huygens Institute -Royal Netherlands Academy of Arts and Sciences (KNAW). **11**, 168 (1909).

10. Landau, L. Theory of the superfluidity of helium II. *Phys. Rev.* **60**, 356 (1941)

11. Tisza, L. Transport Phenomena in Helium II. *Nature* **141,** 913 (1938)

12. Andronikashvili, E. Direct observation of two types of motion in helium II. *J. Phys. USSR* **10,** 201 (1946)

13. Guénault, T. Basic Superfluids. *Taylor & Francis* London**,** pp.1–51 (2003)

14. Hartmann, M., Miller, R. E., Toennies, J. P., Vilesov, A. Rotationally resolved spectroscopy of SF6 in liquid helium clusters: A molecular probe of cluster temperature. *Phys. Rev. Lett.* **75**, 1566 (1995)

15. Grebenev, S. Superfluidity Within a Small Helium-4 Cluster: The Microscopic Andronikashvili Experiment. *Science* **279,** 2083 (1998)

16. Mateo, D., Gonzalez, F., Eloranta, J. Rotational superfluidity in small helium droplets. *J. Phys. Chem. A* **119**, 2262 (2015)

17. Patel, M. V, Viel, A., Paesani, F., Huang, P., Whaley, K. B. Effects of molecular rotation on densities in doped ^{4}He clusters. *J. Chem. Phys.* **1181,** 2341 (2003)

18. Lewerenz, M., Schilling, B., Toennies, J. P. Successive capture and coagulation of atoms and molecules to small clusters in large liquid helium clusters. *J. Chem. Phys.* **102,** 8191 (1995)

19. Lewis, W. K. *et al*. Electron impact lonization in helium nanodroplets: Controlling fragmentation by active cooling of molecular ions. *J. Am. Chem. Soc.* **126**, 11283 (2004)

20. Nauta, K., Miller, R. E. Formation of Cyclic Water Hexamer in Liquid Helium: The Smallest Piece of Ice. *Science* **287**, 293–5 (2000)

21. Lehmann, K. K. Potential of a neutral impurity in a large ^{4}He cluster. *Mol. Phys.* **97**, 1 (1999)

22. Toennies, J. P., Vilesov, A. F. Spectroscopy of atoms and molecules in helium droplets. *Annu. Rev. Phys. Chem.* **49,** 1 (1998)

23. Tiggesbäumker, J., Stienkemeier, F. Formation and properties of metal clusters isolated in helium droplets. *Phys. Chem. Chem. Phys.* **9,** 4748 (2007)

24. An Der Lan, L., Bartl, P., Leidlmair, C., Schöbel, H., Denifl, S., Märk, T. D., Ellis, A. M., Scheier, P. Submersion of potassium clusters in helium nanodroplets. *Phys. Rev. B - Condens. Matter Mater. Phys.* **85,** 115414 (2012)

25. An Der Lan, L., Bartl, P., Leidlmair, C., Schöbel, H., Jochum, R., Denifl, S., Märk, T. D., Ellis, A. M., Scheier, P. The submersion of sodium clusters in helium nanodroplets: Identification of the surface → interior transition. *J. Chem. Phys.* **135,** 44309 (2011)

26. Onsager, L. *Nuovo Cim. Suppl.* **6,** 249 (1949).

27. Feynman, R. P. Application of quantum mechanics to liquid helium in: "Progress in Low Temperature Physics". *North-holl. Publ. Co.* Amsterdam , Chapter 11 (1955)

28. Donnelly, R. J. Discovery and Properties of Quantized Vortices in Helium II in: "Advances in Cryogenic Engineering". *Springer Sci. Bus. Media* New York, pp. 25–34 (1990)

29. Gross, E. P. Observations on Single Vortex Lines in Rotating Superfluid Helium4. *Nuovo Cim. Ser.* **10**, 454 (1961)

30. Barenghi, C. F. "Introduction to qunatised vortices and turbulence" in Vor. Turbul. Very Low Temp. *Springer*, Vienna **7,** 1 (2008)

31. Yarmchuk, E. J., V Gordon, M. J., Packard, R. E. observation of Stationary Vortex Arrays in Rotating Superfluid Helium. *Phys. Rev. Lett.* **43**, 214 (1979)

32. Donnelly, R. J. Quantized Vortices in helium II. *Cambridge Univ. Press* New York pp. 1–15 (1991)

33. Gomez, L. F., Loginov, E., Vilesov, A. F. Traces of vortices in superfluid helium droplets. *Phys. Rev. Lett.* **108**, 155302 (2012)

34. Scheidemann, A., Schilling, B., Toennies, J. P. Anomalies in the reactions of helium(1+) with sulfur hexafluoride embedded in large helium-4 clusters. *J. Phys. Chem.* **97**, 2128–2138 (1993)

35. Lewis, W. K., Lindsay, C. M., Bemish, R. J., Miller, R. E. Probing charge-transfer processes in helium nanodroplets by Optically Selected Mass Spectrometry (OSMS): Charge steering by long-range interactions. *J. Am. Chem. Soc.* **127**, 7235 (2005)

36. Shepperson, B., Liu, J., Ellis, A. M., Yang, S. Ionization of doped helium nanodroplets: Residual helium attached to diatomic cations and their clusters. *J. Phys. Chem. A* **115**, 7010 (2011)

37. Ellis, A. M., Yang, S. A model for the charge transfer probability in helium nanodroplets following electron impact ionization. **44**, 032714 (2007)

38. Schöbel, H., Bartl, P., Leidlmair, C., Daxner, M., Zöttl, S., Denifl, S., Märk, T. D., Scheier, P., Spångberg, D., Mauracher, A., Bohme D. K. Sequential penning ionization: Harvesting energy with Ions. *Phys. Rev. Lett.* **105**, 243402 (2010)

39. von Issendorff, B., Haberland, H., Frochtenicht, R., Toennies, J. Spectroscopic observation of a metastable electronically excited He^{4+}. *Chem. Phys. Lett.* **233**, 23 (1995)

40. Yang, S., Brereton, S. M., Wheeler, M. D., Ellis, A. M. Soft or hard ionization of molecules in helium nanodroplets? An electron impact investigation of alcohols and ethers. *Phys. Chem. Chem. Phys.* **7**, 4082 (2005)

41. Ovchinnikov, M., Grigorenko, B. L., Janda, K. C., Apkarian, V. A. Charge localization and fragmentation dynamics of ionized helium clusters. *J. Chem. Phys.* **108**, 9351 (1998)

42. Lewis, W. K., Applegate, B. E., Sztáray, J., Sztáray, B., Baer, T., Bemish, R. J., Miller, R. E. Electron impact lonization in helium nanodroplets: Controlling fragmentation by active cooling of molecular ions. *J. Am. Chem. Soc.* **126**, 11283 (2004)

43. Yang, S., Brereton, S. M., Ellis, A. E., Electron Impact Ionization of Haloalkanes in Helium Nanodroplets. *J. Phys. Chem. A* **110**, 7 (2006)

44. Yang, S., Brereton, S. M., Ellis, A. M. Electron impact ionization mass spectrometry of aliphatic alcohol clusters in helium nanodroplets. *Int. J. Mass Spectrom.* **253**, 79 (2006)

45. Shepperson, B. Tandy, J., Boatwright, A., Feng, C., Spence, D., Shirley, A., Shengfu Yang, Ellis, A. E. Electronic spectroscopy of toluene in helium nanodroplets: Evidence for a long-lived excited state. *J. Phys. Chem. A* **117**, 13591 (2013)

46. Goulart, M., Kuhn, M., Rasul, B., Postler, J., Gatchell, M., Zettergren, H., Scheier, P., Echt, O. The structure of coronene cluster ions inferred from H2 uptake in the gas phase. *Phys. Chem. Chem. Phys.* **19**, 27968 (2017)

47. Krasnokutski, S. A., Huisken, F. Ultra-low-temperature reactions of C ($^3P_0$) atoms with benzene molecules in helium droplets. *J. Chem. Phys.* **141**, 214306 (2014).

48. Buchenau, H. , Knuth, E. L., Northby, J., Toennies, J. P., C. Winkler, C. Mass spectra and time-of-flight distributions of helium cluster beams. *J. Chem. Phys.* **92**, 6875–6889 (1990)

49. Gomez, L. F., Loginov, E., Sliter, R., Vilesov, A. F. Sizes of large He droplets. *J. Chem. Phys.* **135**, 154201 (2011)

50. Hohenberg, P., Kohn, W. Inhomogeneous Electron Gas. *Phys. Rev.* **136,** 864 (1964)

51. Jensen, F. Introduction to Computational Chemsitry. *John Wiley Sons Ltd.* West Sussex, Chapter 6 (2007)

52. Tirado-Rives, J., Jorgensen, W. L. Performance of B3LYP density functional methods for a large set of organic molecules. *J. Chem. Theory Comput.* **4**, 297 (2008)

53. O'Neal, M. J., Wier, T. P. Mass Spectrometry of Heavy Hydrocarbons. *Anal. Chem.* **23**, 830 (1951)

54. Rashman, R. M., Oliver, R. W. A. Mass Spectrometry of Quinones. Part II. A Study of the Distinguishing Features found in the Mass Spectra of 1,2- and 1,4-Naphthaquinones.

J. Chem. Soc. B **0**, 341 (1971)

55. Roithová, J., Schröder, D., Schwarz, H. Decomposition of neutral, singly and doubly protonated benzoquinone in the gas phase. *Chem. Eur. J.* **11**, 628 (2005)

56. Lauer, G, Schafer, W., Schweig, A. Assignment of the four lowest ionized states of p-benzoquinone and the question of 'lone pair splitting' in this system. *Chem. Phys. Lett.* **33**, 312–315 (1975)

57. Müller, S., Mudrich, M., Stienkemeier, F. Alkali-helium snowball complexes formed on helium nanodroplets. *J. Chem. Phys.* **131**, 044319 (2009)

58. Li, Q., Kartikowati, C. W., Horie, S., Ogi, T., Iwaki, T., Okuyama, K. Correlation between particle size/domain structure and magnetic properties of highly crystalline Fe_3O_4 nanoparticles. *Sci. Rep.* **7**, 9894 (2017)

59. Kossut, J. Squeeze or stretch? *Nat. Mater.* **8**, 8–9 (2009)

60. Moser, A., Takano, K., Margulies, D. T., Albrecht, M., Sonobe1, Y., Ikeda1, Y., Sun, S., Fullerton, E. E., Magnetic recording: Advancing into the future. *J. Phys. D. Appl. Phys.* **35**, 157 (2002)

61. Piramanayagam, S. N., Chong, T. C. Developments in Data Storage: Materials Perspective. *John Wiley Sons Ltd.* New Jersey (2012)

62. Li, S., Zhai, S. -R., Zhang, J. -M., Xiao, Z. -Y., An, Q. -D., Li, M. -H., Song, X. -W. Magnetic and stable $H_3PW_{12}O_{40}$-based core@shell nanomaterial towards the esterification of oleic acid with methanol. *Eur. J. Inorg. Chem.* **0**, 5428 (2013)

63. Vono, L. L. R., Damasceno C. C., Matos, J. R., Jardim, R. F., Landers, R., Masunaga, S. H., Rossi, L. M. Separation technology meets green chemistry: Development of magnetically recoverable catalyst supports containing silica, ceria, and titania. *Pure Appl. Chem.* **90**, 13 (2018)

64. Monfared, B., Furberg, R. & Palm, B. Magnetic vs. vapor-compression household refrigerators: A preliminary comparative life cycle assessment. *Int. J. Refrig.* **42,** 69–76 (2014).

65. Xu, Y., Pi, H., Ren, T., Yang, Y., Ding, H., Peng, T., Li, L., Design of a Multipulse High-Magnetic-Field System Based on Flywheel Energy Storage. IEEE Trans. Appl. Supercond. **26**, 5207005 (2016)

66. Liu, L., Lei, X., Tang, H., Zeng, R., Chen, Y., Zhang, H. Influences of la doping on magnetic and electrochemical properties of $Li_3V_2(PO_4)_3$/C cathode materials for lithium-ion batteries. *Electrochim. Acta* **151,3**78 (2015)

67. Balasubramanian, B., Das, B., Skomski, R., Zhang, W. Y., Sellmyer, D. J. Novel nanostructured rare-earth-free magnetic materials with high energy products. *Adv. Mater.* **25**, 6090 (2013)

68. Vallabani, N. V. S., Singh, S. Recent advances and future prospects of iron oxide nanoparticles in biomedicine and diagnostics. *3 Biotech* **8**, 279 (2018)

69. Wu, W., Wu, Z., Yu, T., Jiang, C., Kim, W.-S. Recent progress on magnetic iron oxide nanoparticles: synthesis, surface functional strategies and biomedical applications. *Sci. Technol. Adv. Mater.* **16**, 023501 (2015)

70. Teremova, M. I., Petrakovskaya, E. A., Romanchenko, A.S., Tuzikov, F. V., Gurevich,

Y. L., Tsibina, O.V., Yakubailik E. K., A. Ferritization of Industrial Waste Water and Microbial Synthesis of Iron-Based Magnetic Nanomaterials From Sediments. *Environ. Sci. Technol.* **33**, 482 (2014)

71. Yavuz, C. T, Mayo, J. T., Yu, W. W., Prakash, A., Falkner, J. C., Yean, S., Cong, L., Shipley, H. J., Kan, A., Tomson, M., Natelson, D., Colvinl, V. L. MagneticLow-Field Magnetic Separation of Fe_3O_4 Nanocrystals. *Science* **314,** 964 (2006)

72. Benelmekki, M. 'An introduction to nanoparticles and nanotechnology' in Designing Hybrid Nanoparticles. *Morgan Claypool Publ.* California**,** Chapter 1 (2015)

73. Eustis, S., El-Sayed, M. A. Why gold nanoparticles are more precious than pretty gold: Noble metal surface plasmon resonance and its enhancement of the radiative and nonradiative properties of nanocrystals of different shapes. *Chem. Soc. Rev.* **35**, 209 (2006)

74. Vatta, L. L., Sanderson, R. D., Koch, K. R. Magnetic nanoparticles: Properties and potential applications. *Pure Appl. Chem.* **78**, 1793 (2006)

75. Haruta, M. When gold is not noble: Catalysis by nanoparticles. *Chem. Rec.*, **3**, 75 (2003)

76. Frenkel, J., Doefman, J. Spontaneous and Induced Magnetization in Ferromagnetic Bodies. *Nature* **23**, 274 (1930)

77. Bean, C. P., Livingston, J. D. Superparamagnetism. *J. Appl. Phys.* **30**, 120 (1959)

78. Bean, C. P. Hysteresis Loops of Mixtures of Ferromagnetic Micropowders. *J. Appl. Phys.* **26**, 1381 (1955)

79. Kittel, C. Theory of the Structure of Ferromagnetic Domains in Films and Small Particles. *Phys. Rev.* **70**, 965 (1946)

80. Krishnan, K. M. Pakhomov, A. B., Bao, Y., Blomqvist, P., Chun, Y., Gonzales, M., Griffin, K., Ji, X., Roberts, B. K. Nanomagnetism and spin electronics: Materials, microstructure and novel properties. *J. Mater. Sci.* **41**, 793 (2006)

81. Bedanta, S., Kleemann, W. Supermagnetism. *J. Phys. D. Appl. Phys.* **42**, 013001 (2009)

82. Terris, B. D., Thomson, T., Hu, G. Patterned media for future magnetic data storage. *Microsyst. Technol.* **13,** 189 (2007)

83. Lim, C. W., Lee, I. S. Magnetically recyclable nanocatalyst systems for the organic reactions. *Nano Today* **5**, 412 (2010)

84. Khan, M., Duan J., Chen, Y., Yao, H., Lyu, S., Shou, H., Heng, K., Xu, Q. Superparamagnetic nickel–substituted manganese ferrite ($Mn_{0.8}Ni_{0.2}Fe_2O_4$) nanoplates as anode materials for lithium-ion batteries. *J. Alloys Compd.* **701**, 147 (2017)

85. Tuçek, J., Kemp, K. C., Kim, K. S., Zboṛil, R. Iron-oxide-supported nanocarbon in lithium-ion batteries, medical, catalytic, and environmental applications. *ACS Nano* **8,** 7571 (2014)

86. Shao, M., Ning, F., Zhao, J., Wei, M., Evans, D. G., Duan, X., Preparation of Fe_3O_4@SiO_2@layered double hydroxide core-shell microspheres for magnetic separation of proteins. *J. Am. Chem. Soc.* **134**, 1071 (2012)

87. Jing, Y., He, S., Kline, T., Xu, Y., Wang, J. P. High-magnetic-moment nanoparticles for biomedicine. *Proc. 31st Annu. Int. Conf. IEEE Eng. Med. Biol. Soc. Eng. Futur. Biomed.*

EMBC, 4483–4486 (2009)

88. Laurent, S., Forge, D., Port, M., Roch, A., Robic, C., Elst, L. V., Muller, R. N., Magnetic Iron Oxide Nanoparticles: Synthesis, Stabilization, Vectorization, Physicochemical Characterizations, and Biological Applications. *Chem. Rev.* **108**, 2064 (2008)

89. Pankhurst, Q. A., Connolly, J., K, J. S., Dobson, J. Applications of magnetic nanoparticles in biomedicine. *J. Phys. D* **36**, 167 (2003)

90. Reddy, L. H., Arias, J. L., Nicolas, J., Couvreur, P. Magnetic nanoparticles: Design and characterization, toxicity and biocompatibility, pharmaceutical and biomedical applications. *Chemical Reviews* **112**, 5818 (2012)

91. Mahmoudi, M., Hofmann, H., Rothen-Rutishauser, B., Petri-Fink, A. Assessing the in vitro and in vivo toxicity of superparamagnetic iron oxide nanoparticles. *Chemical Reviews* **112**, 2323 (2012)

92. Yang, Y., Jiang, X., Chao, J., Song, C., Liu, B., Zhu, D., Sun, Y., Yang, B., Zhang, Q., Chen, Y., Wang, L., Synthesis of magnetic core-branched Au shell nanostructures and their application in cancer-related miRNA detection via SERS. *Sci China Mater* **60**, 1129 (2017)

93. Busquets, M. A., Sabaté, R. , Estelrich, J. Potential applications of magnetic particles to detect and treat Alzheimer's disease. *Nanoscale Res. Lett.* **9**, 538 (2014)

94. Okoli, C., Boutonnet, M., Mariey, L., Arås, S., Rajarao, G. Application of magnetic iron oxide nanoparticles prepared from microemulsions for protein purification. *J Chem Technol Biotechnol* **86**, 1386 (2011)

95. Mahmoudi, K., Bouras, A., Bozec, D., Ivkov, R., Hadjipanayis, C. Magnetic hyperthermia therapy for the treatment of glioblastoma: a review of the therapy's history, efficacy and application in humans. *Int. J. Hyperth.* **34**, 1316 (2018)

96. Kafrouni, L., Savadogo, O. Recent progress on magnetic nanoparticles for magnetic hyperthermia. *Prog. Biomater.* **5**, 147(2016)

97. Simeonidis, K., Li´ebana-Vi˜nas, S., Wiedwald, U., Ma, Z., Li, Z., Spasova, M., Patsia, O., Myrovali, E., Makridis, A., Sakellari, D., Tsiaoussis, I., Vourlias, G., Farle, M., Angelakeris, M. A versatile large-scale and green process for synthesizing magnetic nanoparticles with tunable magnetic hyperthermia features. *RSC Adv.* **6**, 53107–53117 (2016)

98. Liu, Q., Song, L., Chen, S., Gao, J., Zhao, P., Du, J. A superparamagnetic polymersome with extremely high T2relaxivity for MRI and cancer-targeted drug delivery. *Biomaterials* **114**, 23 (2017)

99. Kansara, K., Patel, P., Shukla, R. K., Pandya, A., Shanker, R., Kumar, A., Dhawan, A., Synthesis of biocompatible iron oxide nanoparticles as a drug delivery vehicle. Int. J. Nanomedicine **13**, 79–82 (2018)

100. Wahajuddin , Arora, S. Superparamagnetic iron oxide nanoparticles: Magnetic nanoplatforms as drug carriers. *International Journal of Nanomedicine* **7**, 3445 (2012)

101. Sanson, C. Diou, O., Thevenot, J., Ibarboure, E., Soum, A., Brulet, A., Miraux, S., Thiaudiere, E., Tan, S., Brisson, A., Dupuis, V., Sandre, O., Lecommandoux, S. Doxorubicin loaded magnetic polymersomes: Theranostic nanocarriers for MR imaging and magneto-chemotherapy. *ACS Nano* **5**, 1122 (2011)

102. Thakor, A. S., Gambhir, S. S. Nanooncology: The future of cancer diagnosis and therapy. *CA. Cancer J. Clin.* **63**, 395 (2013)

103. Plank, C., Zelphati, O., Mykhaylyk, O. Magnetically enhanced nucleic acid delivery. Ten years of magnetofection-Progress and prospects. *Advanced Drug Delivery Reviews* **63**, 1300, (2011)

104. Wang, G. Zhang, X., Skallberg, A., Liu, Y., Hu Z., Mei, X., Uvdal, K. One-step synthesis of water-dispersible ultra-small Fe3O4 nanoparticles as contrast agents for T1 and T2 magnetic resonance imaging. *Nanoscale* **6**, 2953 (2014)

105. Shen, Z., Wu, A., Chen, X. Iron Oxide Nanoparticle Based Contrast Agents for Magnetic Resonance Imaging. *Mol. Pharm.* **14**, 1352 (2017)

106. Li, Z. Yi, P. W., Sun, Q., Lei, H., Zhao, H. L., Zhu, Z. H., Smith, S. C., Lan, M. B., Lu, G. Q. Ultra-small water-soluble and biocompatible magnetic iron oxide nanoparticles as positive and negative dual contrast agents. *Adv. Funct. Mater.* **22**, 2387 (2012)

107. Wilhelm, C., Gazeau, F. Universal cell labelling with anionic magnetic nanoparticles. *Biomaterials* **29**, 3161 (2008)

108. Correia Carreira, S., Armstrong, J. P. K., Seddon, A. M., Perriman, A. W., Hartley-Davies, R., Schwarzacher, W. Ultra-fast stem cell labelling using cationized magnetoferritin. *Nanoscale* **8**, 7474 (2016)

109. Cabrera, M. P., Cabral Filho, P. E., Silva, C. M. C. M., Oliveira, R. M., Geraldes, C. F. G. C., Castro, M. M. C. A., Costa, B. F. O., Henriques, M. S. C., Paixão, J. A., Carvalho Jr, L. B., Santos , B. S., Hallwass , F., Fontes, A., Pereira, G. A. L, Highly fluorescent and superparamagnetic nanosystem for biomedical applications. *Nanotechnology* **28**, 285704 (2017)

110. Berman, S. C., Walczak, P., Bulte, Jeff W.M. Tracking stem cells using magnetic nanoparticles. *Wiley Interdiscip Rev Nanomed Nanobiotechnol.* **3**, 343 (2011)

111. HOW DOES IT WORK? Magnetic resonance imaging. *Clin. Rev.* **234**, 35 (2002).

112. Grover, V. P. B., Tognarelli, J. M., Crossey, M. M. E., Cox, J. I, Taylor-Robinson, S. D., McPhail, M. J. W. Magnetic Resonance Imaging: Principles and Techniques: Lessons for Clinicians. *Journal of Clinical and Experimental Hepatology*, **5**, 246 (2015)

113. Yan, G. -P., Robinson, L., Hogg, P. Magnetic resonance imaging contrast agents: Overview and perspectives. *Radiography* **13**, 5 (2007)

114. Yan, X., Yi-Jie, W., Wen-Jun, Z., Xiao-Jing, L., Feng-Kui, P. Research Progress of Magnetic Resonance Imaging Contrast Agents. *Chinese Journal of Analytical Chemistry* **39**, 757 (2011)

115. Lohrke, J., Frenzel, T., Endrikat, J., Caseiro Alves, F., Grist, T. M., Law, M., Min Lee, J., Leiner, T., Li, K. -C., Nikolaou, K., Prince, M. R., Schild, H. H., Weinreb, J. C., Yoshikawa, K., Pietsch, H., 25 Years of Contrast-Enhanced MRI: Developments, Current Challenges and Future Perspectives. *Adv Ther* 33, 1 (2016)

116. Wang, Y.-X. J. Superparamagnetic iron oxide based MRI contrast agents: Current status of clinical application. *Quant Imaging Med Surg* **1,3**5 (2011)

117. Xiao, Y. D. Paudel, R., Liu, J., Ma, C., Zhang, Z. -S., Zhou, S. -K. MRI contrast agents: Classification and application (Review). *International Journal of Molecular Medicine* **38**, 1319 (2016)

118. Ledneva, E., Karie, S., Launay-Vacher, V., Janus, N., Deray, G. Renal Safety of Gadolinium-based Contrast Media in Patients with Chronic Renal Insufficiency. *Radiology* **250**, 618 (2009)

119. Grobner, T. Gadolinium – a specific trigger for the development of nephrogenic fibrosing dermopathy and nephrogenic systemic fibrosis? *Nephrol Dial Transpl.* **21** 1104 (2006)

120. Kuo, P. H., Kanal, E., Abu-Alfa, A. K., Cowper, S. E. Gadolinium-based MR Contrast Agents and Nephrogenic Systemic Fibrosis. *Radiology* **242**, 647 (2007)

121. Broome, D. R. Nephrogenic systemic fibrosis associated with gadolinium based contrast agents: A summary of the medical literature reporting. *Eur. J. Radiol.* **66**, 230 (2008)

122. Abujudeh, H.H, Kaewlai, R., Kagan, A., Chibnik, L.B., Nazarian, R.M., High, W.A., Kay, J. Nephrogenic Systemic Fibrosis after Gadopentetate Dimeglumine Exposure: Case Series of 36 Patients. **253,** 81 (2009)

123. Ramalho, Semelka, R. C., Ramalho, M., Nunes, R. H., AlObaidy, M., Castillo, M. Gadolinium-based contrast agent accumulation and toxicity: An update. *AJNR Am J Neuroradiol* **37,** 1192 (2016)

124. Kanda, T., Fukusato, T., Matsuda, M., Toyoda, K., Oba, H., Kotoku, J., Haruyama, T., Kitajima, K., Furui, S. Gadolinium-based Contrast Agent Accumulates in the Brain Even in Subjects without Severe Renal Dysfunction: Evaluation of Autopsy Brain Specimens with Inductively Coupled Plasma Mass Spectroscopy. *Radiology* **276**, 228 (2015)

125. Kanda, T., Oba, H., Toyoda, K., Kitajima, K., Furui, S. Brain gadolinium deposition after administration of gadolinium-based contrast agents. *Jpn J Radiol* **34**, 3 (2016)

126. Yan, X., Yi-Jie, W., Wen-Jun, Z., Xiao-Jing, L., Feng-Kui, P. Research Progress of Magnetic Resonance Imaging Contrast Agents. *Chinese J. Anal. Chem.* **39**, 757 (2011)

127. Estelrich, J., Sánchez-Martín, M. J. & Busquets, M. A. Nanoparticles in magnetic resonance imaging: From simple to dual contrast agents. *Int. J. Nanomedicine* **10**, 1728 (2015)

128. Li, L., Jiang, W., Luo, K., Song , H., Lan , F., Wu, Y., Gu, Z. Superparamagnetic iron oxide nanoparticles as MRI contrast agents for non-invasive stem cell labeling and tracking. *Theranostics* **3**, 595 (2013)

129. Carril, M., Fernández, I., Rodríguez, J., García, I., Penadés, S. Gold-coated iron oxide glyconanoparticles for MRI, CT, and US multimodal imaging. *Part. Part. Syst. Charact.* **31**, 81 (2014)

130. Bea, H., Ahmad, T., Rhee, I., Chang, Y., Jin, S., Hong, S. Carbon-coated iron oxide nanoparticles as contrast agents in magnetic resonance imaging. *Nanoscale Res. Lett.* **7**, 1 (2012)

131. Iqbal, M. Z., Ma, X., Chen, T., Zhang, L., Ren, W., Xiang, L., Wu, A. Silica-coated super-paramagnetic iron oxide nanoparticles (SPIONPs): a new type contrast agent of T_1 magnetic resonance imaging (MRI). *J. Mater. Chem. B* **3**, 5172 (2015)

132. Masoudi, A., Madaah Hosseini, H. R., Shokrgozar, M. A., Ahmadi, R., Oghabian, M. A. The effect of poly(ethylene glycol) coating on colloidal stability of superparamagnetic iron oxide nanoparticles as potential MRI contrast agent. *Int. J. Pharm.* **433**, 129 (2012)

133. Jarrett, B. R., Frendo, M., Vogan, J. Louie, A. Y. Size-controlled synthesis of dextran

sulfate coated iron oxide nanoparticles for magnetic resonance imaging. *Nanotechnology* **18**, 7 (2007)

134. Doiron, A. L., Homan, K. A., Emelianov, S., Brannon-peppas, L. Poly(Lactic-co-Glycolic) Acid as a Carrier for Imaging Contrast Agents. *Pharm. Res.* **26**, 674 (2009)

135. Rui, Y. P. Liang, B., Hu, F., Xu, F., P, Y. -F., Yin, P. -H., Duan, Y., Zhang, C., Gu, H. Ultra-large-scale production of ultra-small superparamagnetic iron oxide nanoparticles for T1-weighted MRI. *RSC Adv.* **6**, 22575 (2016)

136. Vetter, A., Reinisch, A., Strunk, D., Kremser, C., Hahn, H. W., Huck, C. W., Ostermann, T., Leithner, K., Bernkop-Schnürch, A. Thiolated polyacrylic acid-modified iron oxide nanoparticles for in vitro labeling and MRI of stem cells. *J. Drug Target.* **19**, 562 (2011)

137. Tassa, C., Shaw, S. Y., Weissleder, R. Dextran-coated iron oxide nanoparticles: A versatile platform for targeted molecular imaging, molecular diagnostics, and therapy. *Acc. Chem. Res.* **44**, 842 (2011)

138. Nitin, N., LaConte, L. E. W., Zurkiya, O., Hu, X., Bao, G. Functionalization and peptide-based delivery of magnetic nanoparticles as an intracellular MRI contrast agent. *J. Biol. Inorg. Chem.* **9**, 706 (2004)

139. Liao, Z., Wnag, H., Lv, R., Zhao, P., Sun, X., Wang, S., Su, W., Niu, R., Chang, J. Polymeric liposomes-coated superparamagnetic iron oxide nanoparticles as contrast agent for targeted magnetic resonance imaging of cancer cells. *Langmuir* **27**, 3100 (2011)

140. Huang, J., Wang, L., Lin, R., Wang, A. Y., Yang, L., Kuang, M., Qian, W., Mao, H. Casein-coated Iron Oxide Nanoparticles for High MRI Contrast Enhancement and Efficient Cell Targeting. *ACS Appl Mater Interfaces* **5**, 4632 (2013)

141. Krishnan, K. M. Biomedical nanomagnetics: A spin through possibilities in imaging, diagnostics, and therapy. *IEEE Trans. Magn.* **46**, 2523 (2010)

142. De La Fuente, J. M., Alcántara, D., Penadés, S. Cell response to magnetic glyconanoparticles: Does the carbohydrate matter? *IEEE Trans. Nanobioscience* **6**, 275 (2007)

143. Panahifar, A., Mahmoudi, M., Doschak, M. R. Synthesis and in vitro evaluation of bone-seeking superparamagnetic iron oxide nanoparticles as contrast agents for imaging bone metabolic activity. *ACS Appl. Mater. Interfaces* **5**, 52195226 (2013)

144. Jun, Y. W., Huh, Y -M., Choi, J., Lee, J. -H., Song, H. -T., Kim, S., Yoon, S., Kim, K. -S., Shin, J. -S., Suh, J. -S., Cheon, J. Nanoscale Size Effect of Magnetic Nanocrystals and Their Utilization for Cancer Diagnosis via Magnetic Resonance Imaging. *J. Am. Chem. Soc.* **127**, 5732 (2005)

145. Rosen, J. E., Chan, L., Shieh, D. Bin, Gu, F. X. Iron oxide nanoparticles for targeted cancer imaging and diagnostics. *Nanomedicine Nanotechnology, Biol. Med.* **8**, 275 (2012)

146. Corot, C., Warlin, D. Superparamagnetic iron oxide nanoparticles for MRI: Contrast media pharmaceutical company R&D perspective. *Wiley Interdiscip. Rev. Nanomedicine Nanobiotechnology* **5**, 411 (2013)

147. He, Y., Zhang, L., Zhu, D., Song, C. Design of multifunctional magnetic iron oxide nanoparticles/mitoxantrone-loaded liposomes for both magnetic resonance imaging and targeted cancer therapy. *Int. J. Nanomedicine* **9**, 4055 (2014)

148. Chertok, B., Moffat, B. A., David, A. E., Yu, F., Bergemann, C., Ross, B. D., Yang, V. C. Iron Oxide Nanoparticles as a Drug Delivery Vehicle for MRI Monitored Magnetic Targeting of Brain Tumors. *Biomaterials* **29**, 487 (2008)

149. Muthu, M. S., Leong, D. T., Mei, L., Feng, S. S. Nanotheranostics - application and further development of nanomedicine strategies for advanced theranostics. *Theranostics* **4**, 660 (2014)

150. Paknikar, K. M., Haghniaz, R. , Umrani, R. Temperature-dependent and time-dependent effects of hyperthermia mediated by dextran-coated La0.7Sr0.3MnO3: in vitro studies. *Int. J. Nanomedicine* **10**, 1609 (2015)

151. Roti, J. L. Cellular responses to hyperthermia (40-46°C): Cell killing and molecular events. *Int. J. Hyperth.* **24**, 3 (2008)

152. Shah, S. A., Reeves, D. B., Ferguson, R. M., Weaver, J. B., Krishnan, K. M. Mixed Brownian alignment and Néel rotations in superparamagnetic iron oxide nanoparticle suspensions driven by an ac field. *Phys. Rev. B* **92**, 094438 (2015)

153. Fortin, J. P., Gazeau, F. , Wilhelm, C. Intracellular heating of living cells through Néel relaxation of magnetic nanoparticles. *Eur. Biophys. J.* **37**, 223 (2008)

154. Rosensweig, R. E. Heating magnetic fluid with alternating magnetic field. *J. Magn. Magn. Mater.* **252**, 370 (2002)

155. Gonzales-Weimuller, M., Zeisberger, M., Krishnan, K. M. Size-dependant heating rates of iron oxide nanoparticles for magnetic fluid hyperthermia. *J. Magn. Magn. Mater.* **321**, 1947 (2009)

156. Habib, A. H., Ondeck, C. L., Chaudhary, P., Bockstaller, M. R., McHenry, M. E. Evaluation of iron-cobalt/ferrite core-shell nanoparticles for cancer thermotherapy. *J. Appl. Phys.* **103**, 7 (2008)

157. Nemati, Z., Alonso, J., Rodrigo, I., Das, R., Garaio, E., García, J. A., Orue, I., Phan, M. - H., Srikanth, H. Improving the Heating Efficiency of Iron Oxide Nanoparticles by Tuning Their Shape and Size. *J. Phys. Chem. C* **122**, 2367 (2018)

158. Gonzalez-Fernandez, M. A., Torres, T. E., Andres-Verges, M., Costo, R., de la Presa, P., Serna, C. J., Morales, M. P., Marquina, C., Ibarra, M. R., Goya, G. F. Magnetic nanoparticles for power absorption: Optimizing size, shape and magnetic properties. *J. Solid State Chem.* **182**, 2779 (2009)

159. Shaterabadi, Z., Nabiyouni, G., Soleymani, M. Optimal size for heating efficiency of superparamagnetic dextran-coated magnetite nanoparticles for application in magnetic fluid hyperthermia. *Phys. C Supercond. its Appl.* **549**, 84 (2018)

160. Martinez-Boubeta, C., Simeonidis, K., Makridis, A., Angelakeris, M., Iglesias, O., Guardia , P., Cabot, A., Yedra, L., Estrade, S., Peiro, F., Saghi, Z., Midgley, P. A., Conde-Lebora´n, I., Serantes, D., Baldomir, D. Learning from nature to improve the heat generation of iron-oxide nanoparticles for magnetic hyperthermia applications. *Sci. Rep.* **3**, 1652 (2013)

161. Noh, S. H., Na, W., J, J., Lee, J. -H., Jung Lee, E., Ho Moon, S., Lim, Y., Shin, J., Cheon, J. Nanoscale magnetism control via surface and exchange anisotropy for optimized ferrimagnetic hysteresis. *Nano Lett.* **12**, 3716 (2012)

162. Lee, J. H., Jang, J., Choi, J., Ho Moon, S., Noh, S., Kim, J., Kim, J. -G., Kim, I. -S., Park, K., I., Cheon, J. Exchange-coupled magnetic nanoparticles for efficient heat

induction. *Nat. Nanotechnol.***6**, 418 (2011)

163. Mohammad, F., Balaji, G., Weber, A., Uppu, R. M., Kumar, C. S. S. R. Influence of gold nanoshell on hyperthermia of superparamagnetic iron oxide nanoparticles. *J. Phys. Chem. C* **114**, 19194 (2010)

164. Larumbe, S., Gómez-Polo, C., Pérez-Landazábal, J. I., Pastor, J. M. Effect of a SiO2 coating on the magnetic properties of Fe3O4 nanoparticles. *J. Phys. Condens. Matter* **24**, 266007(2012)

165. Ramimoghadam, D., Bagheri, S., Hamid, S. B. A. Progress in electrochemical synthesis of magnetic iron oxide nanoparticles. *Journal of Magnetism and Magnetic Materials* **368**, 207(2014)

166. Guiden, D., Dravid, V., Su, M., Fu, L. Smart Therapy : The Multivariate Potentials of Iron Oxide Nanoparticles in Drug Delivery. *Nanoscape* , 71 (2004)

167. Jang, J. T., Nah, H., Lee, J. -H., Ho Moon, S., Gyu Kim, M., Cheon, J. Critical enhancements of MRI contrast and hyperthermic effects by dopant-controlled magnetic nanoparticles. *Angew. Chem. Int. Ed.* **48**, 1234 (2009)

168. Kim, B. H., Lee, N., Kim, H., An, K., Il Park, Y., Choi, Y., Shin, K., Lee, Y., Gu Kwon, S., Bin Na, H., Park, Je. -G., Ahn, T. -Y., Kim, Y. -W., Kyung Moon, W., Hong, Choi, S., Hyeon, T. Large-scale synthesis of uniform and extremely small-sized iron oxide nanoparticles for high-resolution T_1 magnetic resonance imaging contrast agents. *J. Am. Chem. Soc.* **133**, 12624 (2011)

169. Yao, A. H., Wang, D. P., Huang, W. H., Zhang, X., C. Synthesis, Characterisation and in vitro toxicity of self-regulating magnetic implant material for hyperthermia application. *Mater. Sci. Eng. C Mater. Biol. Appl.* **29**, 2525 (2009)

170. Barati, M. R., Suzuki, K., Selomulya, C., Garitaonandia, J. S. New T_c-tuned manganese ferrite-based magnetic implant for hyperthermia therapy application. *IEEE Trans. Magn.* **49**, 3460 (2013)

171. Nguyen, D. T., Kim, K. S. Controlled magnetic properties of iron oxide-based nanoparticles for smart therapy. *KONA Powder and Particle Journal* **33**, 33 (2016)

172. Hoare, T., Santamaria, J., Goya, G. F., Irusta, S., Lin, D., Lau, S., Padera, R., Langer, R., Kohane, D. S. A Magnetically Triggered Composite Membrane for On-Demand Drug Delivery. *Nano Lett.* **9**, 3651 (2009)

173. Liu, T. Y., Liu, K. H., Liu, D. M., Chen, S. Y., Chen, I. W. Temperature-sensitive nanocapsules for controlled drug release caused by magnetically triggered structural disruption. *Adv. Funct. Mater.* **19**, 616 (2009)

174. Feynman, R. Plenty of Room at the Bottom. *Annu. Meet. Am. Phys. Soc. Caltech Pasadena* (1959)

175. Ali, A., Zafar, H., Zia, M., ul Haq, I., Phull, A. R., Ali, J. S., Hussain, A., Synthesis, characterization, applications, and challenges of iron oxide nanoparticles. *Nanotechnol. Sci. Appl.* **9**, 49 (2016)

176. Pereira, C., Pereira, A. M., Fernandes, C., Rocha, M., Mendes, R., Paz Fernández-García, M., Guedes, A., Tavares, P. B., Grenèche, J. -M., Araújo, J. P., Freire, C. Superparamagnetic MFe_2O_4 (M = Fe, Co, Mn) nanoparticles: Tuning the particle size and magnetic properties through a novel one-step coprecipitation route. *Chem. Mater.* **24**, 1496 (2012)

177. Unni, M., Uhl, A. M., Savliwala, S., Savitzky, B. H., Dhavalikar, R., Garraud, N., Arnold, D. P., Kourkoutis, L. F.,Andrew, J. S., Rinaldi, C. Thermal Decomposition Synthesis of Iron Oxide Nanoparticles with Diminished Magnetic Dead Layer by Controlled Addition of Oxygen. *ACS Nano* **11**, 2284 (2017)

178. Shouheng, S., Hao, Z. Size-Controlled Synthesis of Magnetite Nanoparticles. *J. Am. Chem. Soc.* **124**, 8204 (2002)

179. Tian, Y., Yu, B., Li, X., Li, K. Facile solvothermal synthesis of monodisperse Fe3O4 nanocrystals with precise size control of one nanometre as potential MRI contrast agents. *J. Mater. Chem.* **21**, 2476 (2011)

180. Li, S., Zhang, T., Tang, R., Qiu, H., Wang, C., Zhou, Z., Solvothermal synthesis and characterization of monodisperse superparamagnetic iron oxide nanoparticles. *J. Magn. Magn. Mater.* **379**, 226 (2015)

181. Kim, E. H., Lee, H. S., Kwak, B. K., Kim, B. K. Synthesis of ferrofluid with magnetic nanoparticles by sonochemical method for MRI contrast agent. *J. Magn. Magn. Mater.* **289**, 328 (2005)

182. Lastovina, T. A., Budnyk, A. P., Soldatov, M. A., Rusalev, Y. V., Guda, A. A., Bogdan, A. S., Soldatov, A. V., Microwave-assisted synthesis of magnetic iron oxide nanoparticles in oleylamine–oleic acid solutions. *Mendeleev Commun.* **27**, 487 (2017)

183. Sommertune, J., Sugunan, A., Ahniyaz, A., Bejhed, R. S., Sarwe, A., Johansson, C., Balceris, C., Ludwig, F., Posth, O., Fornara, A. Polymer/iron oxide nanoparticle composites—A straight forward and scalable synthesis approach. *Int. J. Mol. Sci.* **16**, 19752 (2015)

184. Ge, S., Shi, X., Sun, K., Li, C., Baker Jr., J. R., Banaszak Holl, M. M., Orr, B. G. A Facile Hydrothermal Synthesis of Iron Oxide Nanoparticles with Tunable Magnetic Properties. *J Phys Chem C Nanomater Interfaces* **113**, 13593 (2009)

185. Park, H., Ayala, P., Deshusses, M. A., Mulchandani, A., Choi, H., Myung, N. V. Electrodeposition of maghemite (γ-Fe2O3) nanoparticles. *Chem. Eng. J.* **139**, 208 (2008)

186. Stephen, Z. R., Kievit, F. M., Zhang, M. Magnetite Nanoparticles for Medical MR Imaging Mater. *Mater. Today* **14**, 330 (2012)

187. De León-Rodríguez, L. M., Martins, A. F., Pinho, M., Rofsky, N., Sherry, A., D. Basic MR Relaxation Mechanisms & Contrast Agent Design. *J Magn Reson Imaging* **42,** 545 (2015)

188. Jacques, V., Dumas, S., Sun, W. -C., Troughton, J. S., Greenfield, M. T., Caravan, P. High relaxivity MRI contrast agents part 2: Optimization of inner- and second-sphere relaxivity. *Invest. Radiol.* **45**, 613 (2010)

189. Bañobre-López, M., Teijeiro, A., Rivas, J. Magnetic nanoparticle-based hyperthermia for cancer treatment. *Reports Pract. Oncol. Radiother.* **18**, 397 (2013)

190. Kim, T., Shima, M. Reduced magnetization in magnetic oxide nanoparticles. *J. Appl. Phys.* **101,** 09M516, (2007)

191. Kucheryavy, P., He, J., John , V. T., Maharjan , P., Spinu, L., Goloverda, G. Z., Kolesnichenko, V. L., Superparamagnetic iron oxide nanoparticles with variable size and an iron oxidation state as prospective imaging agents. *Langmuir* **29**, 710 (2013)

192. Fiorani, D. Surface Effects in Magnetic Nanoparticles. *Springer Sci. Bus. Media, Inc.*

New York (2005)

193. Hu, D., Wang, Y., Song, Q. Weakly magnetic field-assisted synthesis of magnetite nano-particles in oxidative co-precipitation. *Particuology* **7,** 363 (2009)

194. Samadi, M. S., Shokrollahi, H., Zamanian, A. The magnetic-field-assisted synthesis of the Co-ferrite nanoparticles via reverse co-precipitation and their magnetic and structural properties. *Mater. Chem. Phys.* **215**, 355 (2018)

195. Wang, J., Zhang, K., Peng, Z., Chen, Q. Magnetic properties improvement in Fe_3O_4 nanoparticles grown under magnetic fields. *J. Cryst. Growth* **266**, 500 (2004)

196. Li, Y., Hu K., Chen, B., Liang, Y., Fan, F., Sun, J., Zhang, Y., Gu, N., Fe_3O_4@PSC nanoparticle clusters with enhanced magnetic properties prepared by alternating-current magnetic field assisted co-precipitation. *Colloids Surfaces A Physicochem. Eng. Asp.* **520**, 348 (2017)

197. Maeda, H., Wu, J., Sawa, T., Matsumura, Y., Hori, K. Tumor vascular permeability and the EPR effect in macromolecular therapeutics: a review. *J. Control. Release* **65**, 271 (2000).

198. Zhou, Z. H., Wang, J., Liu, X., Chan, H. S. O. Synthesis of Fe_3O_4 nanoparticles from emulsions. *J. Mater. Chem.* **11**, 1704 (2001)

199. Morales, M. P., Veintemillas-Verdaguer, S., Montero, M. I., Serna, C. J. Surface and Internal Spin Canting in γ-Fe $_2O_3$ Nanoparticles. *Chem. Mater.* **11,3**058 (1999)

200. Li, L., Yang, Y., Ding, J., Xue, J. Synthesis of magnetite nanooctahedra and their magnetic field-induced two-/three-dimensional superstructure. *Chem. Mater.* **22**, 3183 (2010)

201. Chen, J., Sorensen, C., Klabunde, K. Size-dependent magnetic properties of MnFe2O4 fine particles synthesized by coprecipitation. *Phys. Rev. B - Condens. Matter Mater. Phys.* **54**, 9288 (1996)

202. Xiao, W., Liu, X., Hong, X., Yang, Y., Fang, J., Ding, J. Magnetic-field-assisted synthesis of magnetite nanoparticles via thermal decomposition and their hyperthermia properties. *CrystEngComm* **17**, 3652 (2015)

203. Massart, R. Preparation of Aqueous Magnetic Liquids in Alkaline and Acidic Media. *IEEE Transactions on Magnetics* **17**, 1247 (1981)

204. Wikswo, J. P. SQUIDs Remain Best Tools for Measuring Brain's Magnetic Field. *Phys. Today* **57,** 15 (2004)

205. Correa, J. R., Bordallo, E., Canetti, D., Leon, V., Otero-Dı´az, L. C., Negro, C., Go´mez, A., Sa´ez-Puche, R. Structure and superparamagnetic behaviour of magnetite nanoparticles in cellulose beads. *Mater. Res. Bull.* **45,** 946 (2010)

206. Santoyo Salazar, J., Perez, L., de Abril, O., Truong Phuoc, L., Ihiawakrim, D., Vazquez, M., Greneche, J. -M., Begin-Colin, S., Pourro, G. Magnetic iron oxide nanoparticles in 10-40 nm range: Composition in terms of magnetite/maghemite ratio and effect on the magnetic properties. *Chem. Mater.* **23**, 1379 (2011)

207. H Hui, C., Shen, C., Yang, T., Bao, L., Tian, J., Ding, H., Li, C., Gao, H. Large-Scale Fe_3O_4 Nanoparticles Soluble in Water Synthesized by a Facile Method. *J. Phys. Chem. C* **112**, 11336 (2008)

208. Yang, Y. Liu, X., Lv, Y., Herng, T. S., Xu, X., Xia, W., Zhang, T., Fang, J., Xiao, W., Ding, J.
Orientation mediated enhancement on magnetic hyperthermia of Fe_3O_4 nanodisc. *Adv. Funct. Mater.* **25**, 812 (2015)

209. Ruíz-Baltazar, A., Esparza, R., Rosas, G., Pérez, R. Effect of the Surfactant on the Growth and Oxidation of Iron Nanoparticles. *J. Nanomater.* **2015**, 1 (2015)

210. Kolen'Ko, Y. V., Bañobre-López, M., Rodríguez-Abreu, C., Carbó-Argibay, E., Sailsman, A., Piñeiro-Redondo, Y., Fátima Cerqueira, M., Petrovykh, D. Y., Kovnir, K., Lebedev, O. I., Rivas, J. Large-scale synthesis of colloidal Fe3O4nanoparticles exhibiting high heating efficiency in magnetic hyperthermia. *J. Phys. Chem. C* **118**, 8691 (2014)

211. Mahdavi, M., Ahmad, M. B., Haron, M. J., Namvar, F., Nadi, B., Ab Rahman, M. Z., Amin, J. Synthesis, surface modification and characterisation of biocompatible magnetic iron oxide nanoparticles for biomedical applications. *Molecules* **18**, 7533 (2013)

212. Wu, M., Xiong, Y., Jia, Y., Niu, H., Qi, H., Ye, Y., Chen, Q. Magnetic field-assisted hydrothermal growth of chain-like nanostructure of magnetite. *Chem. Phys. Lett.* **401,3**74 (2005)

213. Fujiwara, M., Chie, K., Sawai, J., Shimizu, D., Tanimoto, Y. On the Movement of Paramagnetic Ions in an Inhomogeneous Magnetic Field. *J. Phys. Chem. B* **108**, 3531 (2004)

214. Ikezoe, Y., Hirota, N., Nakagawa, J., Kitazawa, K. Making water levitate. *Nature* **393**, 749 (1998)

215. Zhang, L., He, R., Gu, H. C. Synthesis and kinetic shape and size evolution of magnetite nanoparticles. *Mater. Res. Bull.* **41**, 260 (2006)

216. Cornell, R. M., Schwertmann, U. The Iron Oxides: Structure, Properties, Reactions, Occurrences and Uses. *John Wiley Sons* Weinheim**,** Chapter 6 (2003)

217. Mohapatra, J., Mitra, A., Bahadur, D. & Aslam, M. Surface controlled synthesis of MFe2O4(M = Mn, Fe, Co, Ni and Zn) nanoparticles and their magnetic characteristics. *CrystEngComm* **15**, 524 (2013)

218. Lee, Y., Lee, J., Jin Bae, C., Park, J. -G., Noh, H. -J., Park, J -H., Hyeon, T. Large-Scale Synthesis of Uniform and Crystalline Magnetite Nanoparticles Using Reverse Micelles as Nanoreactors under Reflux Conditions. *Adv. Funct. Mater.* **15**, 503 (2005)

219. Mørup, S., Tronc, E. Superparamagnetic relaxation of weakly interacting particles. *Phys. Rev. Lett.* **72**, 3278 (1994)

220. Concas, G., Congiu, F., Muscas, G., Peddis, D. Determination of Blocking Temperature in Magnetization and Mössbauer Time Scale: A Functional Form Approach. *J. Phys. Chem. C* **121**, 16541 (2017)

221. Kim, B. H., Hackett, M. J., Park, J., Hyeon, T. Synthesis, characterization, and application of ultra-small nanoparticles. *Chem. Mater.* **26**, 59 (2014)

222. Zarschler, K., Rocks, L., Licciardello, N., Boselli, L., Polo, E., Garcia, K. P., De Cola, L., Stephan, H., Dawson, K. A., Ultra-small inorganic nanoparticles: State-of-the-art and perspectives for biomedical applications. *Nanomedicine Nanotechnology, Biol. Med.* **12**, 1663 (2016)

223. Guptaa, A., K., Guptab, M. Synthesis and surface engineering of iron oxide nanoparticles for biomedical applications. *Biomaterials* **26**, 3995 (2005)

224. Almeida, J., Allen L Chen, A. L., Foster, A., Drezek, R. In vivo biodistribution of nanoparticles. *Nanomedicine* **6,** 815 (2011)

225. Ernsting, M. J., Murakami, M., Roy, A., Li, S.-D. Factors Controlling the Pharmacokinetics, Biodistribution and Intratumoral Penetration of Nanoparticles. *J Control Release* **172**, 782(2013)

226. Oostendorp, M., Post, M. J., Backes, W. H. Vessel Growth and Function: Depiction with Contrast-enhanced MR Imaging. *Radiology* **251,3**17 (2009)

227. Longmire, M., Choyke, P. L., Kobayashi, H. Clearance properties of nano-sized particles and molecules as imaging agents: Considerations and caveats. *Nanomedicine* **3**, 703 (2008)

228. Uchiyama, MK, Toma, SH, Rodrigues, SF, Shimada, AL, Loiola, RA, Cervantes Rodríguez, HJ, Oliveira, PV, Luz, M, Rabbani, SR, Toma, HE, Poliselli Farsky, SH, Araki, K. Ultra-small cationic superparamagnetic iron oxide nanoparticles as nontoxic and efficient MRI contrast agent and magnetic-targeting tool. *Int J Nanomedicine.* **10**, 4731 (2015)

229. Lee, J. J., Tirman, P. J., Chang, Y., Ryeom, H. K., Lee, S. K., Kim, Y. S, Kang, K. S., The Optimization of Scan Timing for Contrast-Enhanced Magnetic Resonance Angiography. *Korean J. Radiol.* **1**, 142 (2000)

230. Singh, R. Unexpected magnetism in nanomaterials. *J. Magn. Magn. Mater.* **346**, 58 (2013)

231. Tucek, J., Sofer , Z., Bousˇa, D., Pumera, M., Hola, K., Mala, A., Pola´kova, K., Havrdova, M., Cˇe´pe, K., Tomanec, O., Zborˇil, R. Air-stable superparamagnetic metal nanoparticles entrapped in graphene oxide matrix. *Nat. Commun.* **7**, 1 (2016)

232. Sato, T., Iijima, T., Seki, M., Inagaki, N. Magnetic properties of ultrafine ferrite particles. *J. Magn. Magn. Mater.* **65**, 252 (1987)

233. Yang, H., Liu, C., Yang, D., Zhang, H., Xi, Z. Comparative study of cytotoxicity, oxidative stress and genotoxicity induced by four typical nanomaterials: The role of particle size, shape and composition. *J. Appl. Toxicol.* **29**, 69 (2009)

234. Yoon, T., Lee, H., Shao, H., Weissleder, R. Highly Magnetic Core – Shell Nanoparticles with a Unique Magnetization Mechanism. *Angew. Chemie Int. Ed.* **50**, 4663 (2011)

235. Zhang, G., Liao, Y., Baker, I. Surface Engineering of Core/Shell Iron oxide/iron Nanoparticles from Microemulsions for Hyperthermia. *Mater Sci Eng C Mater Biol Appl.* **30**, 92 (2010)

236. Yang, B., Li, X., Yang, X., Yu, R. Chemical synthesis of Fe/Fe3O4 core-shell composites with enhanced soft magnetic performances. *J. Magn. Magn. Mater.* **428**, 6 (2017)

237. López-Ortega, A., Estrader, M., Salazar-Alvarez, G., Roca, A. G. & Nogués, J. Applications of exchange coupled bi-magnetic hard/soft and soft/hard magnetic core/shell nanoparticles. *Phys. Rep.* **553**, 1 (2015)

238. Nemati, Z., Khurshid, H., Alonso, J., Phan, M. H., Mukherjee, P., Srikanth, H. From core/shell to hollow Fe/$_{\gamma}$-Fe_2O_3 nanoparticles: Evolution of the magnetic behavior.

Nanotechnology **26**, 405705 (2015)

239. Costo, R., Bello, V., Robic, C., Port, M., Marco, J. F., Puerto Morales, M., Veintemillas-Verdaguer, S. Ultra-small iron oxide nanoparticles for biomedical applications: improving the colloidal and magnetic properties. *Langmuir* **28**, 178 (2012)

240. Baker, S. H., Roy, M., Thornton, S. C., Qureshi, M., Binns, C. Probing atomic structure in magnetic core/shell nanoparticles using synchrotron radiation. *J. Phys. Condens. Matter* **22**, 385301 (2010).

241. Yang, S., Ellis, A. M., Spence, D., Feng, C., Boatwright, A., Latimer, E., Binns, C., Growing metal nanoparticles in superfluid helium. *Nanoscale* **5**, 11545 (2013)

242. Kim, M., Osone, S., Kim, T., Higashi, H., Seto, T. Synthesis of nanoparticles by laser ablation: A review. *KONA Powder Part. J.* **2017**, 80 (2017)

243. Sequeira, C. A. C. Electrochemical Synthesis of Iron Oxide Nanoparticles for Biomedical Application. *Org. Med. Chem IJ* **5**, 1 (2018)

244. Wang, R., Zuo, S., Wu, D., Zhang, J., Zhu, W., Becker, K. H., Fang, J., Microplasma-assisted synthesis of colloidal gold nanoparticles and their use in the detection of cardiac Troponin I (cTn-I). *Plasma Process. Polym.* **12**, 380(2015)

245. Masayuki, S., Ohgiyama, T., Clements, J. S. Formation of Chemical Species and Their Effects on Microorganisms Using a Plused High-Voltage Discharge in Water. *IEEE Trans. Ind. Appl.* **32**, 106 (1996)

246. Cavendish, H. Experiments on Air. *Phil. Trans.* **75**, 372 (1785)

247. Rosen, A. L., Hieftje, G. M. Inductively coupled plasma mass spectrometry and electrospray mass spectrometry for speciation analysis: Applications and instrumentation. *Spectrochim. Acta - Part B At. Spectrosc.* **59**, 135 (2004)

248. Webb, M. R., Hieftje, G. M. Spectrochemical analysis by using discharge devices with solution electrodes. *Anal. Chem.* **81**, 862 (2009)

249. Stevenson, P., Gregory, K., Cliffe, R. J., Smith, I. R. A RING CARBON PLASMA GUN FOR THE PLASMA OPENING SWITCH. *tPPPS-2001 Pulsed Power Plasma Sci. 2001. 28th IEEE Int. Conf. Plasma Sci.* (2001)

250. Tichonovas, M. Krugly, E., Racys, V., Hippler, R., Kauneliene, V., Stasiulaitiene, I., Martuzevicius, D. Degradation of various textile dyes as wastewater pollutants under dielectric barrier discharge plasma treatment. *Chem. Eng. J.* **229**, 9 (2013)

251. Foster, J., Sommers, B. S., Gucker, S. N., Blankson, I. M., Adamovsky, G. Perspectives on the interaction of plasmas with liquid water for water purification. *IEEE Trans. Plasma Sci.* **40**, 1311 (2012)

252. Holland, L. Some characteristics and uses of low-pressure plasmas in materials science. *J. Vac. Sci. Technol.* **14**, 5 (1977)

253. Wertheimer, M. R. Plasma processing and polymers: A personal perspective. *Plasma Chem. Plasma Process.* **34**, 363 (2014)

254. Babb, J. Ayliffe, G., Bradley, C., Jackson, M., Johnson, M., Taylor, E., Hansford, J., Ingram, I., Fowler, C. Decontamination of minimally invasive surgical endoscopes and accessories. *J. Hosp. Infect.* **45**, 263 (2000)

255. Fridman, G. Friedman, G., Gutsol, A., Shekhter, A. B., Vasilets, V. N.,Fridman, A. Applied plasma medicine. *Plasma Process. Polym.* **5**, 503 (2008)

256. Ostrikov, K., Neyts, E. C., Meyyappan, M. Plasma nanoscience: From nano-solids in plasmas to nano-plasmas in solids. *Adv. Phys.* **62**, 113 (2013)

257. Takai, O. Solution plasma processing (SPP). *Pure Appl. Chem.* **80**, 2003 (2008)

258. Cui, S. Mattson, E. C., Lu, G., Hirschmugl, C., Gajdardziska-Josifovska, M., Chen, J. Tailoring nanomaterial products through electrode material and oxygen partial pressure in a mini-arc plasma reactor. *J. Nanoparticle Res.* **14**, 744 (2012)

259. Grammatikopoulos, P., Steinhauer, S., Vernieres, J., Singh, V., Sowwan, M. Nanoparticle design by gas-phase synthesis. *Adv. Phys. X* **1**, 81 (2016)

260. Tabrizi, N. S., Xu, Q., Van Der Pers, N. M., Lafont, U., Schmidt-Ott, A. Synthesis of mixed metallic nanoparticles by spark discharge. *J. Nanoparticle Res.* **11**, 1209 (2009)

261. Hamdan, A., Noël, C., Ghanbaja, J., Belmonte, T. Comparison of aluminium nanostructures created by discharges in various dielectric liquids. *Plasma Chem. Plasma Process.* **34**, 1101 (2014)

262. Kareem, T. A., Kaliani, A. A. Glow discharge plasma electrolysis for nanoparticles synthesis. *Ionics (Kiel).* **18**, 315 (2012)

263. Hu, X., Shen, X., Takai, O., Saito, N. Facile fabrication of PtAu alloy clusters using solution plasma sputtering and their electrocatalytic activity. *J. Alloys Compd.* **552**, 351 (2013)

264. Hu, X., Cho, S. P., Takai, O., Saito, N. Rapid synthesis and structural characterization of well-defined gold clusters by solution plasma sputtering. *Cryst. Growth Des.* **12**, 119 (2012)

265. Hu, X. L., Takai, O., Saito, N. Synthesis of gold nanoparticles by solution plasma sputtering in various solvents. *J. Phys. Conf. Ser.* **417**, conference 1(2013)

266. Koo, I. G., Lee, M. S., Shim, J. H., Ahn, J. H., Lee, W. M. Platinum nanoparticles prepared by a plasma-chemical reduction method. *J. Mater. Chem.* **15**, 4125 (2005)

267. Kelgenbaeva, Z., Omurzak, E., Takebe, S., Sulaimankulova, S., Abdullaeva, Z., Iwamoto, C., Mashimo, T. Synthesis of pure iron nanoparticles at liquid-liquid interface using pulsed plasma. *J. Nanoparticle Res.* **16**, 2603 (2014)

268. Omurzak, E., Jasnakunov, J., Mairykova, N., Abdykerimova, A., Maatkasymova, A., Sulaimankulova, S., Matsuda, M., Nishida, M., Ihara, H., Mashimo, T. Synthesis Method of Nanomaterials by Pulsed Plasma in Liquid. *J. Nanosci. Nanotechnol.* **7**, 3157 (2007)

269. Yuan, Y., Rende, D., Altan, C. L., Bucak, S., Ozisik, R., Borca-Tasciuc, D. A. Effect of surface modification on magnetization of iron oxide nanoparticle colloids. *Langmuir* **28**, 13051 (2012)

270. Charinpanitkul, T., Soottitantawat, A., Tonanon, N., Tanthapanichakoon, W. Single-step synthesis of nanocomposite of copper and carbon nanoparticles using arc discharge in liquid nitrogen. *Mater. Chem. Phys.* **116**, 125 (2009)

271. Horikoshi, S., Serpone, N. In-liquid plasma: A novel tool in the fabrication of nanomaterials and in the treatment of wastewaters. *RSC Adv.* **7**, 47196 (2017)

272. Bruggeman, P., Leys, C. Non-thermal plasmas in and in contact with liquids. *J. Phys. D. Appl. Phys.* **42**, (2009)

273. Toriyabe, Y., Watanabe, S., Yatsu, S., Shibayama, T., Mizuno, T. Controlled formation of metallic nanoballs during plasma electrolysis. *Appl. Phys. Lett.* **91**, 041501 (2007)

274. Lee, H. Park, S. H., Kim, S. J., Park, Y. K., An, K. H. Kim, B. J., Jung, S. C. Liquid phase plasma synthesis of iron oxide/carbon composite as dielectric material for capacitor. *J. Nanomater.* **2014**, 1 (2014)

275. Hamdan, A., Noël, C., Ghanbaja, J., Migot-Choux, S., Belmonte, T. Synthesis of platinum embedded in amorphous carbon by micro-gap discharge in heptane. *Mater. Chem. Phys.* **142**, 199 (2013)

276. Kabbara, H. Noël, C., Ghanbaja, J., Hussein, K., Mariotti, D., Švrcek, V., Belmonte, T. Synthesis of nanocrystals by discharges in liquid nitrogen from Si-Sn sintered electrode. *Sci. Rep.* **5**, 1 (2015)

277. Mariotti, D., Sankaran, R. M. Microplasmas for nanomaterials synthesis. *J. Phys. D. Appl. Phys.* **43**, 323001 (2010)

278. Saito, G., Akiyama, T. Nanomaterial Synthesis Using Plasma Generation in Liquid. *J. Nanomater.* **2015**, 123696 (2015)

279. Lee, H., Park, S. H., Jung, S. C., Yun, J. J., Kim, S. J., Kim, D. H. Preparation of nonaggregated silver nanoparticles by the liquid phase plasma reduction method. *J. Mater. Res.* **28**, 1105 (2013)

280. Lee, H. Park, S. H., Park, Y. K., Kim, B. H., Kim, S. J., Jung, S. C. Rapid destruction of the rhodamine B using TiO_2 photocatalyst in the liquid phase plasma. *Chem. Cent. J.* **7**, 156 (2013)

281. Dzimitrowicz, A., Jamroz, P., Pogoda, D., Nyk, M., Pohl, P. Direct current atmospheric pressure glow discharge generated between a pin-type solid cathode and a flowing liquid anode as a new tool for silver nanoparticles production. *Plasma Process. Polym.* **14**, 1600251 (2017).

282. Dzimitrowicz, A., Greda, K., Lesniewicz, T., Jamroz, P., Nyk, M., Pohl, P. Size-controlled synthesis of gold nanoparticles by a novel atmospheric pressure glow discharge system with a metallic pin electrode and a flowing liquid electrode. *RSC Adv.* **6,** 80773 (2016).

283. Dzimitrowicz, A., Motyka, A., Jamroz, P., Lojkowska, E., Babinska, W., Terefinko, D., Pohl, P., Sledz, W. Application of silver nanostructures synthesized by cold atmospheric pressure plasma for inactivation of bacterial phytopathogens from the genera Dickeya and Pectobacterium. *Materials* **11,3**31 (2018)

284. Dzimitrowicz, A., Cyganowski, P., Pohl, P., Jermakowicz-Bartkowiak, D., Terefinko, D., Jamroz, P. Atmospheric Pressure Plasma-Mediated Synthesis of Platinum Nanoparticles Stabilized by Poly(vinylpyrrolidone) with Application in Heat Management Systems for Internal Combustion Chambers. *Nanomaterials* **8**, 619 (2018)

285. Motyka, A., Dzimitrowicz, A., Jamroz, P., Lojkowska, E., Sledz, W., Pohl, P. Rapid eradication of bacterial phytopathogens by atmospheric pressure glow discharge generated in contact with a flowing liquid cathode. *Biotechnol. Bioeng.* **115**, 1581 (2018)

286. Dzimitrowicz, A., Bielawska-Pohl, A., DiCenzo, G., Jamroz, P., Macioszczyk, J.,

Klimczak, A., Pohl, P. Pulse-Modulated Radio-Frequency Alternating-Current-Driven Atmospheric-Pressure Glow Discharge for Continuous-Flow Synthesis of Silver Nanoparticles and Evaluation of Their Cytotoxicity toward Human Melanoma Cells. *Nanomaterials* **8**, 398 (2018)

287. Saito, G., Hosokai, S., Tsubota, M., Akiyama, T. Nickel nanoparticles formation from solution plasma using edge-shielded electrode. *Plasma Chem. Plasma Process.* **31**, 719 (2011)

288. Schaper, L., Stalder, K. R., Graham, W. G. Plasma production in electrically conducting liquids. *Plasma Sources Sci. Technol.* **20**, 034004 (2011)

289. Schaper, L., Graham, W. G., Stalder, K. R. Vapour layer formation by electrical discharges through electrically conducting liquids - Modelling and experiment. *Plasma Sources Sci. Technol.* **20**, 034003 (2011)

290. Saito, N., Hieda, J., Takai, O. Synthesis process of gold nanoparticles in solution plasma. *Thin Solid Films* **518**, 912 (2009)

291. Ostrikov, K. Control of energy and matter at nanoscales: Challenges and opportunities for plasma nanoscience in a sustainability age. *J. Phys. D. Appl. Phys.* **44**, 174003 (2011).

292. Kabbara, H., Ghanbaja, J., Noël, C., Belmonte, T. Synthesis of copper and zinc nanostructures by discharges in liquid nitrogen. *Mater. Chem. Phys.* **207**, 350 (2018)

293. Kabbara, H., Ghanbaja, J., Noël, C., Belmonte, T. Synthesis of Cu@ZnO core–shell nanoparticles by spark discharges in liquid nitrogen. *Nano-Structures and Nano-Objects* **10**, 22 (2017)

294. Saito, G., Hosokai, S., Akiyama, T., Yoshida, S.,Yatsu, S.,Watanabe, S. Size-controlled Ni nanoparticles formation by solution glow discharge. *J. Phys. Soc. Japan* **79**, 083501 (2010)

295. Saito, G., Hosokai, S., Akiyama, T. Synthesis of ZnO nanoflowers by solution plasma. *Mater. Chem. Phys.* **130**, 79 (2011)

296. Keidar, M. Levchenko, I., Arbel, T., Alexander, M., Waas, A. M.,Ostrikov, K. K., Magnetic-field-enhanced synthesis of single-wall carbon nanotubes in arc discharge. *J. Appl. Phys.* **103**, 094318 (2008)

297. Levchenko, I., Volotskova, O., Shashurin, A., Raitses, Y., Ostrikov, K., Keidar, M. The large-scale production of graphene flakes using magnetically-enhanced arc discharge between carbon electrodes. *Carbon* **48**, 4570 (2010)

Appendix

A. Background helium droplet mass spectrum

The spectrum below is the background helium droplet mass spectrum recorded with un-doped helium droplets. The main peak was the He_2^+ peak which forms by self-trapping. The helium cluster peaks were caused by attachment to of helium atoms to the He_2^+ ion during ejection. The other peaks indicated were due to background water and nitrogen in the system.

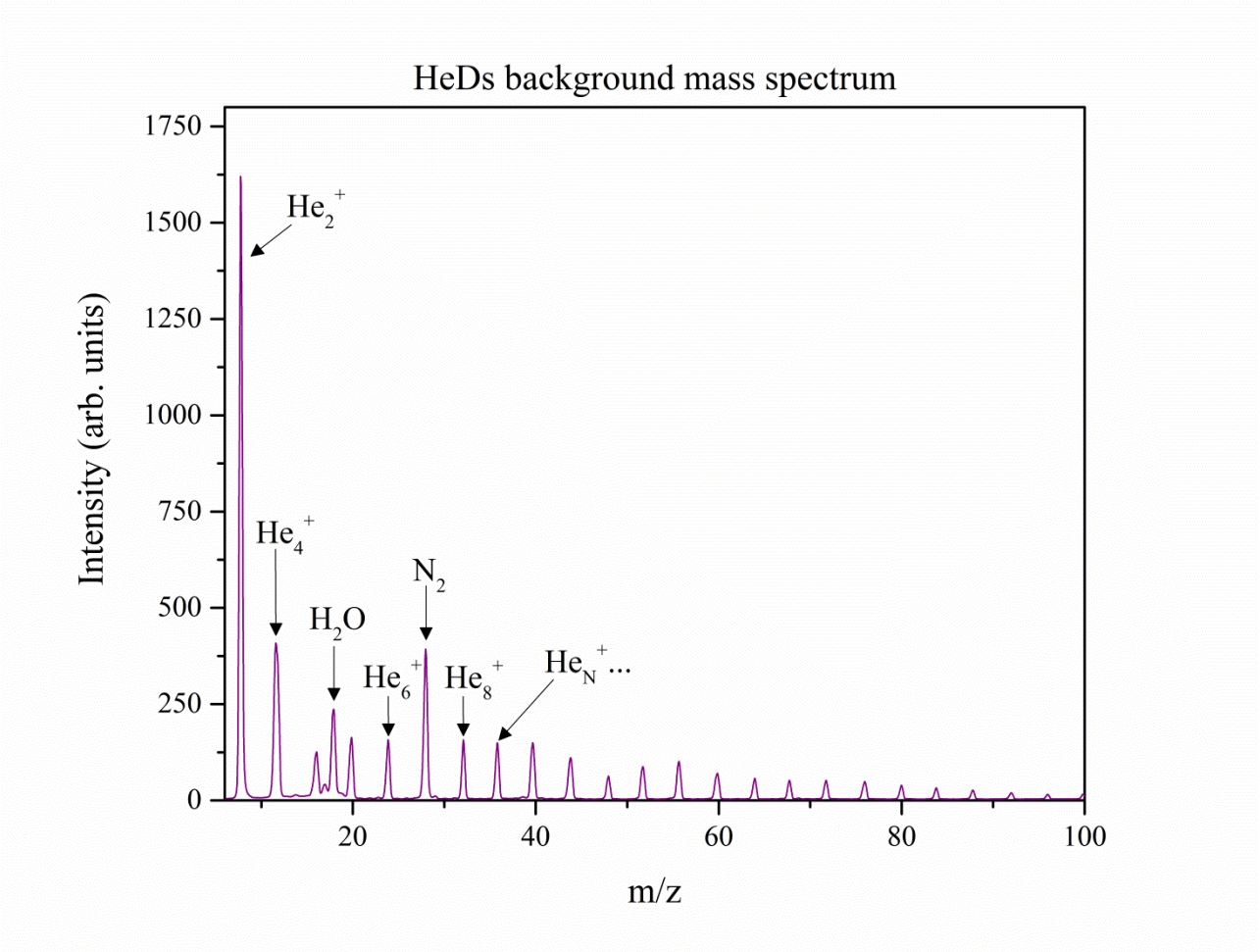

B. Density functional theory calculations in Gaussian16

All density functional theory (DFT) calculations were performed using Gaussian16 (g16) and the cc-pVTZ basis set. Below are example in-put files for the calculations described in the Experimental section in Chapter 1. This sequence of calculations was used for each fragmentation step in the energy profiles in Fig.s 12, 19, 20 and 23. The example in-put files are from the first step of C_2H_2 loss from p-benzoquinone (pathway 1, Fig. 12). The atomic positions of the constituent atoms are represented in XYZ coordinate format. The same in-put file formats were used for all molecules evaluated in this study, however, of course with different XYZ coordinates.

Calculation 1 - optimization of the ground state (*opt* + *freq*)

The ground state structure was optimized using quadratic convergence (QC) criteria. A frequency calculation was also performed to determine whether the structure was a minimum energy structure, which is indicated from all positive frequencies in the output file.

```
%mem=2GB
%NProcShare=2
%chk=qb.chk

# B3LYP/cc-pVTZ opt freq scf=(qc,maxcycle=999)
Integral=Ultrafine

Optimization of p-benzoquinone

0 1
 C                  0.00000000    0.00000000    1.44854400
 C                  0.00000000    1.26775200    0.67497100
 C                  0.00000000    1.26775200   -0.67497100
 C                  0.00000000    0.00000000   -1.44854400
 C                  0.00000000   -1.26775200   -0.67497100
 C                  0.00000000   -1.26775200    0.67497100
 H                  0.00000000    2.18440200    1.25821700
 H                  0.00000000    2.18440200   -1.25821700
 H                  0.00000000   -2.18440200   -1.25821700
 H                  0.00000000   -2.18440200    1.25821700
 O                  0.00000000    0.00000000   -2.67585900
```

```
O                  0.00000000      0.00000000      2.67585900
```

Calculation 2 - single point calculation of the p-benzoquinone ground state

The optimized structure obtained from Calculation 1 was used in Calculation 2 to determine the ionization energy of the molecule. Vertical ionisation was assumed. This means the ground state structure was excited into a vibrational state upon ionization and did not rearrange to a lower vibrational energy state before fragmentation. Therefore, the structure of the parent ion could be assumed to be the same as the ground state molecule. Using this, the energy of the parent ion was obtained from a single point calculation with the optimized XYZ coordinates from Calculation 1 and charge and multiplicity changed to 1 and 2, respectively.

```
%mem=2GB
%NProcShare=2
%chk=qc.chk

# B3LYP/cc-pVTZ Integral=Ultrafine

Single point calc. for ionization of p-benzoquinone

1 2
C     0.000000000000      0.000000000000      1.439304000000
C     0.000000000000      1.265374000000      0.667808000000
C     0.000000000000      1.265374000000     -0.667808000000
C     0.000000000000      0.000000000000     -1.439304000000
C     0.000000000000     -1.265374000000     -0.667808000000
C     0.000000000000     -1.265374000000      0.667808000000
H     0.000000000000      2.175367000000      1.253367000000
H     0.000000000000      2.175367000000     -1.253367000000
H     0.000000000000     -2.175367000000     -1.253367000000
H     0.000000000000     -2.175367000000      1.253367000000
O     0.000000000000      0.000000000000     -2.657244000000
O     0.000000000000      0.000000000000      2.657244000000
```

Calculation 3 - potential energy surface scan for fragmentation

A series of potential energy surface (PES) scan calculations were performed for each fragmentation pathway. This involves varying the bond(s) of interest in the fragmentation pathway (i.e. bond(s) which breaks during fragmentation) either simultaneously or one-bond at a time. The bonds were varied using incremental steps of 0.05-0.2 Å. The step size used depended on whether the atom/fragment was tightly bound or loose. After each stepwise increase in the bond length(s), the geometry was optimized using an *opt* calculation. This produced a relaxed potential energy surface showing the energy change and formation of a potential transition state as the atom(s) fragmented from the molecule.

```
%mem=2GB
%NProcShare=2
%chk=c2h2.chk

# B3LYP/cc-pVDZ opt=(ModRedundant) scf=(xqc,maxcycle=999)
Integral=Ultrafine

PES scan for loss of C2H2 from p-benzoquinone

0 1
C      0.000000000000      0.000000000000      1.439304000000
C      0.000000000000      1.265374000000      0.667808000000
C      0.000000000000      1.265374000000     -0.667808000000
C      0.000000000000      0.000000000000     -1.439304000000
C      0.000000000000     -1.265374000000     -0.667808000000
C      0.000000000000     -1.265374000000      0.667808000000
H      0.000000000000      2.175367000000      1.253367000000
H      0.000000000000      2.175367000000     -1.253367000000
H      0.000000000000     -2.175367000000     -1.253367000000
H      0.000000000000     -2.175367000000      1.253367000000
O      0.000000000000      0.000000000000     -2.657244000000
O      0.000000000000      0.000000000000      2.657244000000
B 1 6 S 30 0.2 → this means the bond between atoms 1 and 6 was
scanned using a step size of 0.2 Å for a total of 30 steps.
```

Calculation 4 - optimization of the 'guess' transition state structure (*opt ts*)

From the PES calculation, the structure with the highest energy at the maximum point along the potential energy surface was taken as the 'guess' transition state structure for the fragmentation step. The guess transition state geometry was optimized using an *opt ts* calculation. Tight convergence was used in instances where the structure of the transition state was 'loose', or alternatively, QC was replaced with XQC. XQC uses normal quadratic convergence but adds another QC step if the geometry has not converged. A frequency calculation (*freq*) was performed separately to determine whether the structure was a potential transition state. Potential transition states were identified by a single negative frequency that vibrates in the direction of the bond breaking/forming process.

Input file for optimization of the guess transition state structure (*opt ts*)

```
%mem=2GB
%NProcShare=2
%chk=tsc2h24m.chk

# B3LYP/cc-pVTZ opt=(calcfc,ts,noeigentest,tight) freq
Integral=Ultrafine scf=(xqc,maxcycle=999)

'guess' ts opt calc. for loss of C2H2 from p-benzoquinone

1 2
C     0.522796000000     -0.980846000000      1.923493000000
C     0.441905000000      1.751071000000      0.601939000000
C    -0.207411000000      1.393024000000     -0.396162000000
C     0.312522000000     -0.066057000000     -1.077204000000
C    -0.170048000000     -1.244438000000     -0.410208000000
C    -0.195481000000     -1.572609000000      0.930032000000
H     1.002523000000      2.035852000000      1.466226000000
H    -0.949966000000      1.846923000000     -1.042747000000
H    -0.650490000000     -1.938740000000     -1.092326000000
H    -0.767354000000     -2.431437000000      1.273190000000
O     0.914569000000      0.059812000000     -2.089877000000
O     1.134273000000     -0.583684000000      2.798254000000
```

Input file for frequency calculation on the optimized transition state structure (*freq*)

```
%mem=2GB
%NProcShare=2
%chk=tsc2h24m.chk

# B3LYP/cc-pVTZ freq Integral=Ultrafine
ts loss of one proton

1 2
C    -1.333838000000     -0.128806000000     -0.077969000000
C    -1.031946000000      1.310323000000      0.034956000000
C     0.010960000000      1.788245000000      0.666065000000
C     1.716283000000     -0.302002000000     -0.168533000000
C     0.911481000000     -1.257431000000      0.443223000000
C    -0.433905000000     -1.167249000000      0.538068000000
H    -1.759602000000      1.963031000000     -0.452338000000
H     0.477155000000      2.724626000000      0.929651000000
H     1.474759000000     -2.110961000000      0.813887000000
H    -0.963577000000     -1.996420000000      0.993306000000
O     2.491453000000      0.330986000000     -0.682216000000
O    -2.274321000000     -0.585831000000     -0.680205000000
```

Calculation 5 - IRC calculation using the transition state structure from the PES scan

An Intrinsic Reaction Coordinate (IRC) calculation was then performed using the optimized transition state structure from Calculation 4. An IRC calculation follows the minimum energy reaction pathway between the transition state and its reactants and products, but will not proceed all the way. Therefore, by optimising the final structure on either side of the IRC curve, the starting reagent structure and the product of the fragmentation step should be obtained. The IRC path can be followed in the forward or reverse direction, or alternatively in both directions. Any of these three options is suitable, but the output file should show a maximum energy and gradient of zero for the transition state structure, hence representing a maximum point. If this is the case, the correct transition state for the fragmentation step has been obtained. The structures

on either side of the IRC curve can then be optimized to obtain the original reagent structure and the product structure using *opt + freq* calculations.

Input file for IRC calculation (*IRC*)

This input file calculates the IRC on both sides of the transition state structure. The IRC on one side can be calculated by adding the syntax '`forward`' (i.e. to product) or '`reverse`' (i.e. to reagent) to the `IRC=(forward/reverse,….)` command.

```
%mem=2GB
%NProcShare=2
%chk=IRCc2h2.chk

# B3LYP/cc-pVTZ
irc=(calcfc,recorrect=never,maxpoint=50,nogradstop)
integral=ultrafine scf=xqc

IRC for C2H2 loss from p-benzoquinone

1 2
C    -1.333838000000     -0.128806000000     -0.077969000000
C    -1.031946000000      1.310323000000      0.034956000000
C     0.010960000000      1.788245000000      0.666065000000
C     1.716283000000     -0.302002000000     -0.168533000000
C     0.911481000000     -1.257431000000      0.443223000000
C    -0.433905000000     -1.167249000000      0.538068000000
H    -1.759602000000      1.963031000000     -0.452338000000
H     0.477155000000      2.724626000000      0.929651000000
H     1.474759000000     -2.110961000000      0.813887000000
H    -0.963577000000     -1.996420000000      0.993306000000
O     2.491453000000      0.330986000000     -0.682216000000
O    -2.274321000000     -0.585831000000     -0.680205000000
```

Calculation 6 – optimization of the product and reagent structure from the IRC profiles from Calculation 5

The structure on either side of the IRC were optimized using an (*opt* + *freq*) calculation. Optimization of the structure on the reagent side should converge to the starting reagent geometry. This was checked by comparing the energies and frequencies from both calculations. Similarly, the structure on the product side of the IRC is optimized and should have all positive frequencies, indicating a minimum. If the optimized product structure was an intermediate, the same set of calculations were performed again for the next step in the fragmentation pathway, and so on until fragmentation was complete.

In-put file for optimization of reagent structure from IRC

```
%mem=2GB
%NProcShare=2
%chk=c2h2reacts2.chk
%nosave

# B3LYP/cc-pVTZ opt freq integral=ultrafine
scf=(xqc,maxcycle=999)

reagent from IRCH.com for proton loss

1 2
 C                 -0.82875700   -0.23226000   -0.16721800
 C                 -2.33549900   -0.25812600   -0.41338000
 C                 -2.96635000    0.32722100    0.52929800
 C                  2.02782000    0.09968900    0.05323000
 C                  1.17651300    1.18669900   -0.04812600
 C                 -0.18112000    1.08112900   -0.10879700
 H                 -2.71449500   -0.91247300   -1.19381600
 H                 -3.41632300    0.85288000    1.34656300
 H                  1.69249900    2.14049600   -0.06056500
 H                 -0.77366400    1.97911100   -0.21026700
 O                  2.86650200   -0.65283100    0.11189800
 O                 -0.21455900   -1.26049100    0.02042800
```

In-put file for optimization of product structure from IRC

```
%mem=2GB
%NProcShare=2
%chk=c2h2prods2.chk
%nosave

# B3LYP/cc-pVTZ opt=tight freq integral=ultrafine scf=xqc

reagent from IRCH.com for proton loss

1 2
 C                 -0.53215200   -0.28279300   -0.00590900
 C                 -2.94234000   -0.03844900   -0.63542700
 C                 -2.97712900    0.17261200    0.56004500
 C                  2.22812400    0.25344600    0.02346100
 C                  1.30941000    1.24156100   -0.09392900
 C                 -0.08137200    1.00608200   -0.10991600
 H                 -2.97042900   -0.26060600   -1.67641300
 H                 -3.06922200    0.40361200    1.57579800
 H                  1.69757200    2.24993900   -0.18105300
 H                 -0.77723300    1.82075800   -0.20355800
 O                  2.98095100   -0.59236400    0.12383700
 O                 -0.43256400   -1.43465400    0.09077200
```

C. ImageJ analysis of Fe_3O_4 nanoparticles

Images were first converted to 8-bit images and thresholded. Because the nanoparticles were heavily aggregated, they were processed using the 'Watershed' plugin. This segments the binary image to remove overlaps between the nanoparticles allowing accurate analysis of the nanoparticles diameter. The average diameter of the nanoparticles was taken from the sum of the Min. and Max. diameter provided by the 'Analysis' plugin and dividing it by two. The average diameters where then plotted to give the histograms in Fig. 30 and the overall average diameter determined.

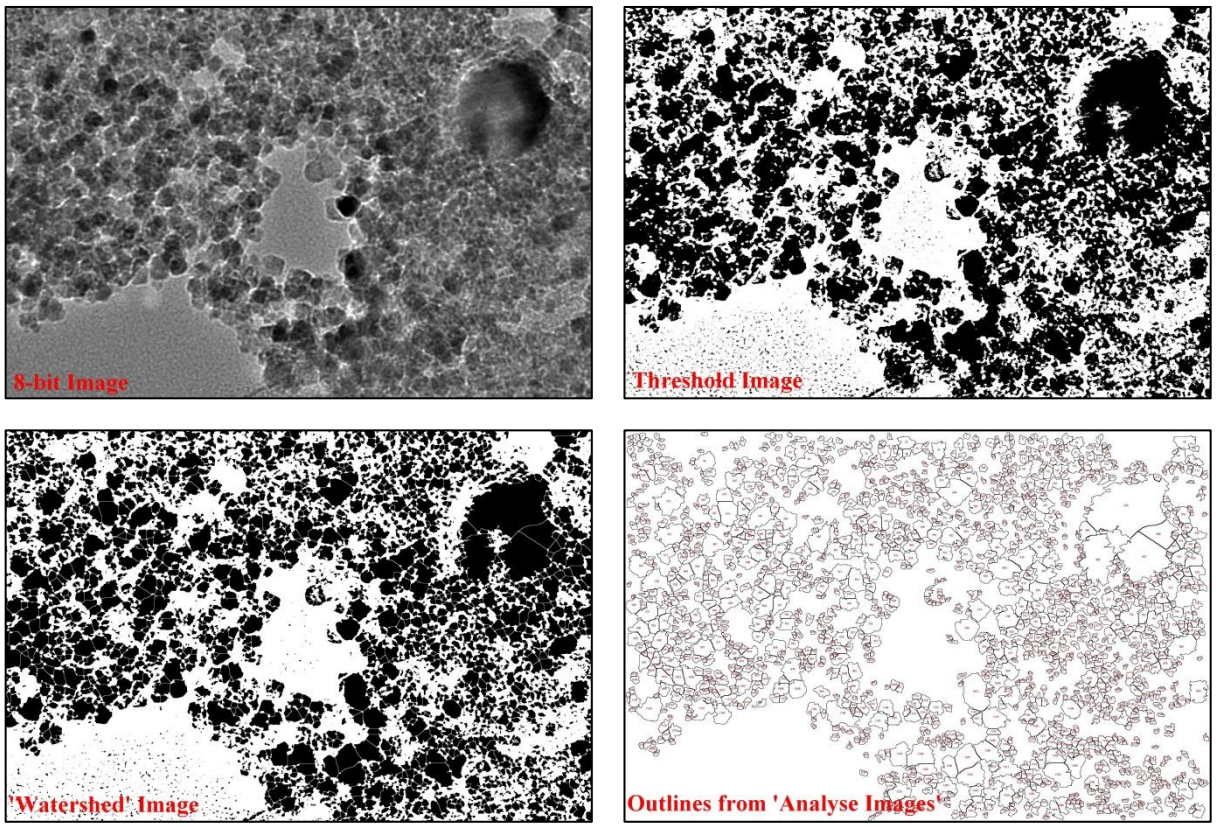

The variation in the shape of the nanoparticles was interpreted by the 'Roundness' plugin. This is calculated from the following equation:

$$Roundness = 4 \text{ x } \frac{[Area]}{\pi \text{ x } [\text{Major axis}]^{2}}$$

Circularity, which is defined as…

$$Circualrity = 4 \text{ x } \frac{[Area]}{[\text{Perimeter}]^{2}}$$

…can also be used to as a measure of the shape of the nanostructure. However, it is less accurate for very small particles. Hence, roundness was used, and average roundness was determined by plotting the results in histograms in Fig. 31.